Meson properties from Lattice QCD

John N. Hedditch

Supervisors: D. B. Leinweber and A. G. Williams

Centre for the Subatomic Structure of Matter
University of Adelaide
Adelaide
2006

This thesis is dedicated to Kati - you are proof the universe is a wonderful place.

Abstract

Quantum Chromo-Dynamics (QCD) is the part of the Standard Model which describes the interaction of the strong nuclear force with matter. QCD is asymptotically free, so at high energies perturbation expansions in the coupling can be used to calculate expectation values. Away from this limit, however, perturbation expansions in the coupling do not converge.

Lattice QCD (LQCD) is a non-perturbative approach to calculations in QCD. LQCD first performs a Wick rotation $t \rightarrow -it_E$, and then discretises spacetime into a regular lattice with some lattice spacing a. QCD is then expressed in terms of parallel transport operators of the gauge field between grid points, and fermion fields which are defined at the grid points. Operators are evaluated in terms of these quantities, and the lattice spacing is then taken to zero to recover continuum values.

We perform computer simulations of Lattice QCD in order to extract a variety of meson observables. In particular, we perform a comprehensive survey of the light and strange meson octets, obtain for the first time exotic meson results consistent with experiment, calculate the charge form-factor of the light and strange pseudoscalar mesons, and determine (for the first time in Lattice QCD) all three form-factors of the vector meson.

Statement of Originality

This work contains no material which has been accepted for the award of any other degree or diploma in any university or other tertiary institution and, to the best of my knowledge and belief, contains no material previously published or written by another person, except where due reference has been made in the text.

I give consent to this copy of my thesis, when deposited in the University Library, being available for loan and photocopying, and further consent to it's reproduction as a musical or theatrical work.

John N. Hedditch

Acknowledgements

- Thank you first of all to Derek Leinweber and Tony Williams, my supervisors, for their tremendous patience, wisdom, and calm, all of which are attributes I would dearly love to posess myself.

- Big Ups to Ben Lasscock for his organisational genius and committment to being a team-player(TM).

- My Hat Off and great thanks to Sara Boffa and Sharon Johnson who have saved me from ruin many a time.

- Three Cheers to James Zanotti, Ross Young, Waseem Kamleh, Alex Kalloniatis, Tony Thomas, Marco Ghiotti and Marco Bartolozzi, Mariusz Hoppe, and all those others who have made working at the CSSM one of the most enjoyable times of my life.

- Thank you to Ramona Adorjan and Grant Ward for computing support, and sense of humour under pressure.

- The Australian Partnership for Advanced Computing, the South Australian Partnership for Advanced Computing, and the National Facility for Lattice Gauge Theory provided the computational muscle for this project, which would have been quite impossible otherwise.
- Finally, a big thankyou to all of my family, and Kati's family, for their support in this endeavour. It's been a wild ride.

Contents

List of Figures

List of Tables

1

Introduction

> *"Research ! A mere excuse for idleness; it has never achieved, and will never achieve any results of the slightest value."*
>
> Benjamin Jowett (1817-93), British theologian.

In this thesis we determine how to explore various meson properties using Lattice techniques. We do so by evaluating the following quark-flow diagrams:

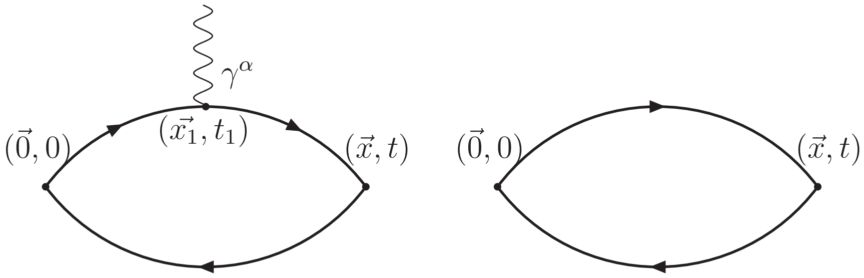

Fig. 1.1: Quark-flow diagrams for three-point and two-point meson vertices.

The fact that the evaluation of these diagrams is sufficient to constitute the basis of a thesis is testament to the complexity of Quantum Chromodynamics. We shall now describe exactly why this is so.

1.1 Quantum Chromodynamics

Quantum Chromodynamics is a tremendously succesful theory of the strong interaction. Mathematically, it is a non-Abelian Gauge Field Theory. It's origins are, however, strongly empirical - they lie in an attempt to explain hundreds of apparently 'fundamental' particles discovered in the 1950s in accelerator experiments.

Sorting the spin-0 mesons, for example, by Charge and Strangeness (indicated by an abnormally long lifetime as strong decays preserve flavour and thus strange particles took longer to decay) yields the structure depicted in Figure 1.2.

This structure (an octet and a singlet) can be obtained from a triplet and anti-triplet obect as follows: $\mathbf{3} \otimes \bar{\mathbf{3}} = \mathbf{8} \oplus \mathbf{1}$.

It was a natural step to consider each of the elements of such a triplet to be a 'flavour' of new fundamental particle which Gell-Mann labelled 'quarks'. The scalar and vector nonets, as well as the baryon octet are very simply explained in terms of three quarks,

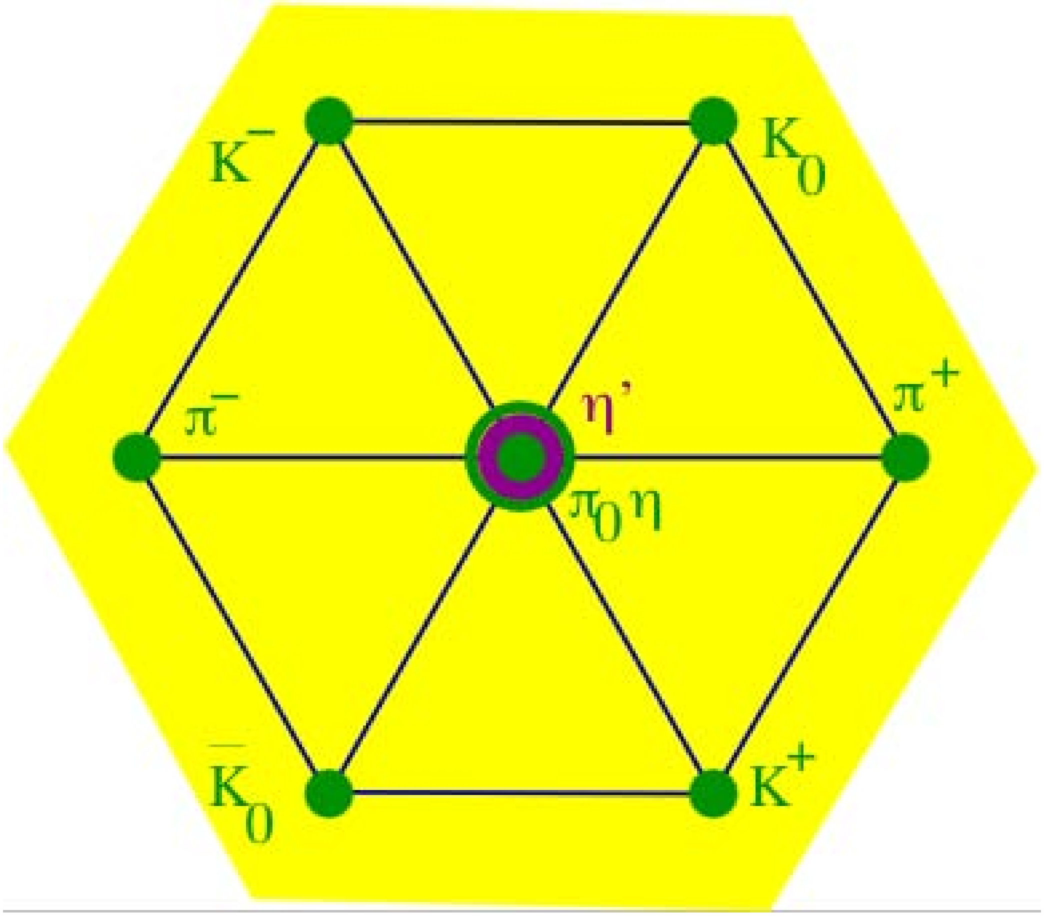

Fig. 1.2: The scalar meson octet and singlet η'. Image courtesy of WikiImages

called ‘up’, ‘down’, and ‘strange’, each with spin $1/2$ and charges $+\frac{2e}{3}, -\frac{e}{3}$, and $-\frac{e}{3}$ respectively with e the magnitude of the electron’s charge. A meson is formed through a quark and an antiquark, a baryon through three quarks.

However, the Δ^{++}, which has a spin of $3/2$ and a charge of twice that of the proton would then require three ‘up’-quarks with their spins aligned. There are not enough quantum numbers available to make such a thing totally antisymmetric (required for fermions). So a new quantum number had to be created, which Gell-Mann called ‘colour’.

The need to introduce colour gave the theory it’s most important characteristics. First, this new quantum number was not observed directly, so the theory was required to be invariant under an arbitrary, local, relabelling of colours. This requirement embeds in the theory some sort of mechanism to keep the colours together in singlet states (confinement), the precise physical mechanism (as opposed to the mathematical requirement) for which is still a great puzzle. The locality of the requirement required the introduction of a gauge field. The relevant gauge group turned out to be $SU(N_c)$. Experiments were able to determine that N_c should be 3 to a fairly high degree of certainty.

$SU(3)$ is a non-abelian group, which makes the theory intrinsically complex, but the major complications of the resultant theory, QCD, are that the theory admits coupling between the gauge bosons with the same strength as between the quarks and gauge bosons (‘gluons’), and that the coupling strength is not small, except at very high energies. Perturbation expansions in the coupling thus do not work in most regimes.

These serve to render QCD analytically intractable except at regimes in which the coupling becomes small (the regime of ‘asymptotic freedom’).

In this thesis, we investigate the masses, characteristic sizes, and electromagnetic form-factors of mesons via numerical simulations. We also probe for some of the more exotic offspring of QCD. The method chosen is that of Lattice Quantum Chromodynamics.

2

Lattice QCD

2.1 Introduction

First, let us step away from Quantum Field Theory altogether and consider a classical Lagrangian field theory. In this case, we start out with a Lagrangian, which describes in some sense the deviation of the system from an energy balance - if the Lagrangian at some point in configuration space is zero, then the four-momentum of the system is shared equally between all degrees of freedom - in this case the various fields and their interactions.

Integrating over the four-volume in which this system exists, and imposing appropriate boundary conditions gives us the Action associated with the system, and we then obtain the equations of motion for the fields - the Euler-Lagrange equations, through the assumption that the trajectory taken by the system in field-configuration-space will be an extremum of this action. This assumption gives us a series of equations (1 per field), the solutions to which define the evolution of our system.

For a theory of N fields $\phi_1, \phi_2, \ldots, \phi_N$, we could express this as

$$Z = \prod_i \left(\int \mathcal{D}\phi_i \right) \delta(\delta S[\phi_1, \ldots, \phi_N]) \,,$$

where the first δ denotes the Dirac delta-function and δS denotes the variation of S. Thus if we were to consider some quantity $\mathcal{Q}[\phi_1, \ldots, \phi_N]$, we could express the classical value of this functional as

$$\langle \mathcal{Q} \rangle = \frac{\prod_i \left(\int \mathcal{D}\phi_i \right) \delta(\delta S[\phi_1, \ldots, \phi_N]) \mathcal{Q}[\phi_1, \ldots, \phi_N]}{\prod_i \left(\int \mathcal{D}\phi_i \right) \delta(\delta S[\phi_1, \ldots, \phi_N])}$$

In fact, in the classical case the denominator is identically unity by the properties of delta functions, but we introduce it for the sake of clarity in what follows. From this point of view, the transition from classical field theory to Quantum field theory is one simple step - replacing the Dirac delta-function from the equation with $e^{-iS/\hbar}$. The major contribution to the integral will still come from the point of minimum action, since away from this point the exponential will be fluctuating rapidly, and contributions from these trajectories should thus cancel each other.

Our quantum-field-theoretical expectation value is then simply

$$\langle \mathcal{Q} \rangle = \frac{\prod_i \left(\int \mathcal{D}\phi_i \right) e^{-iS[\phi_1, \ldots, \phi_N]/\hbar} \mathcal{Q}[\phi_1, \ldots, \phi_N]}{\prod_i \left(\int \mathcal{D}\phi_i \right) e^{-iS[\phi_1, \ldots, \phi_N]/\hbar}}$$

The Lattice was introduced by Kenneth Wilson as a method for studying Quark Confinement [47]. QCD is reformulated on a discrete Euclidean lattice whilst retaining local gauge invariance, and physical quantities are derived from the limits of this theory as the lattice spacing goes to zero (continuum limit), and the number of lattice sites goes to infinity (infinite volume limit).

The key step is a change of variables from the gauge field $A_\mu(x)$ to parallel transport operators (links) $U_\mu(x) = e^{ig\mathcal{P}\int_0^a A_\mu(x+y\hat{\mu})dy}$, where $\mathcal{P}$ is an operator which path-orders the terms in the exponential. A closed product of such links is a gauge-invariant object, and we can in fact express any gauge functional in terms of products of these links.

We can rewrite, for example, a correlation function in this lattice formalism as:

$$C_{ij} = \langle\Omega|T(\Theta_i\Theta_j)|\Omega\rangle = \lim_{a\to 0}\frac{\int \mathcal{D}U\mathcal{D}\bar{\Psi}\mathcal{D}\Psi e^{-S[U,\bar{\Psi},\Psi]}\Theta_i\Theta_j}{\int \mathcal{D}U\mathcal{D}\bar{\Psi}\mathcal{D}\Psi e^{-S[U,\bar{\Psi},\Psi]}} \tag{2.1}$$

Let us now write $S[U,\bar{\psi},\psi] = S_{\mathrm{G}}[U] + \bar{\Psi}M[U]\Psi$. We can then carry out the integration over $\bar{\Psi}$ and Ψ to give

$$C_{ij} = \frac{\int \mathcal{D}Ue^{-S_{\mathrm{G}}[U]}\det(M[U])\cap_{ij}[U]}{\int \mathcal{D}Ue^{-S_{\mathrm{G}}[U]}\det(M[U])} \tag{2.2}$$

where $\cap_{ij}$ is the sum of all full contractions of Θ_i, Θ_j.

In general, we cannot carry out the integration explicitly, so we instead make use of an importance sampling process to yield a finite ensemble of N gauge-fields U with $P(U_k) = \det(M[U_k])e^{-S_G[U_k]}$. We now write

$$C_{ij} \simeq \frac{1}{N}\sum_{k=1}^{N}\cap_{ij}[U_k] \tag{2.3}$$

2.2 Discrete symmetries

2.2.1 Symmetries of Correlation functions

In this section, we show that for the case of QCD, baryonic correlation functions are generally real. We also see how it is possible to enforce this reality in correlation functions, which proves a useful method for reducing statistical errors in lattice calculations of these quantities. This technology was pioneered by Draper *et al.* [19] during the 1980s.

For the following discussion, we need to introduce one important theorem:

Pauli's Theorem: If $[\gamma_\mu,\gamma_\nu]_+ = 2g^{\mu\nu}I = [\tilde{\gamma}_\mu,\tilde{\gamma}_\nu]_+$ then $\exists$ an invertible matrix S such that $\tilde{\gamma}_\mu = S\gamma_\mu S^{-1}, \mu = 0, ..., 3$

Therefore we can define an invertible matrix S such that $S\gamma_\mu S^{-1} = \gamma_\mu^*$. Pauli's theorem holds under a Wick rotation, i.e the replacement of $g_{\mu\nu}$ with $\delta_{\mu\nu}$, so we can make an analogous construction in Euclidean space.

Assertion[1]: If $\gamma_\mu = {\gamma_\mu}^\dagger, \mu = 0,1,2,3$, then $S = C\gamma_5$.

We are now ready to proceed:

Correlation function:
The correlation function in a QCD-like theory is defined as follows:

$$C_{ij} = \langle \Omega | T(\Theta_i \Theta_j) | \Omega \rangle = \frac{\int \mathcal{D}U \mathcal{D}\bar{\Psi} \mathcal{D}\Psi e^{-S[U,\bar{\Psi},\Psi]} \Theta_i \Theta_j}{\int \mathcal{D}U \mathcal{D}\bar{\Psi} \mathcal{D}\Psi e^{-S[U,\bar{\Psi},\Psi]}} \tag{2.4}$$

Suppose we can write $S[U,\bar{\psi},\psi] = S_{\mathrm{G}}[U] + \bar{\Psi} M[U] \Psi$. We can then carry out the integration over $\bar{\Psi}$ and Ψ to give

$$C_{ij} = \frac{\int \mathcal{D}U e^{-S_{\mathrm{G}}[U]} \det(M[U]) \cap_{ij} [U]}{\int \mathcal{D}U e^{-S_{\mathrm{G}}[U]} \det(M[U])} \tag{2.5}$$

where $\cap_{ij}$ is the sum of all full contractions of Θ_i, Θ_j.

Since $U_\mu(x) = \exp\left\{ iga \int_0^a A_\mu(x + x'\hat{\mu}) dx' \right\}$, $U \to U^*$ is equivalent to $A \to -A^*$. eg. $F_{\mu\nu}[U^*] = -(F_{\mu\nu}[U])^*$.

Suppose $M[U] = M[U^*]$.

Assertion[2]: For a Clover-like action we have $M[U]$=$M[U^*]$

Thus $\det(M[U^*]) = \det(SM[U^*]S^{-1}) = \det(M[U]^*) = \det(M[U])^*$. Then if $S_G[U] = S_G[U^*]$, we can write

$$C_{ij} = \frac{1}{2} \left(\frac{\int \mathcal{D}U e^{-S_{\mathrm{G}}[U]} \det(M[U]) \left\{ \cap_{ij}[U] + \cap_{ij}[U^*] \right\}}{\int \mathcal{D}U e^{-S_{\mathrm{G}}[U]} \det(M[U])} \right) \tag{2.6}$$

If we make the following approximation (finite ensemble approximation):

$$\int \mathcal{D}U e^{-S_G[U]} \cap_{ij} [U] \simeq \frac{1}{N} \sum_{k=1}^{N} \cap_{ij}[U_k] \tag{2.7}$$

where the U_k are a finite ensemble wherein the probability of finding a configuration U_n is $e^{-S_G[U_n]}$, then we can replace the above with

$$C_{ij} \simeq \frac{1}{2N} \left(\sum_{k=1}^{N} \cap_{ij}[U_k] + \cap_{ij}[U_k^*] \right) \tag{2.8}$$

---

[1] proof on page 8

[2] proof on page 8

Define $G_{ij} = \mathrm{tr}_{\mathrm{sp}}\{C_{ij}\Gamma\}$ with Γ a γ-matrix product, where $\mathrm{tr}_{\mathrm{sp}}$ denotes the spinor trace.
If $\mathrm{tr}_{\mathrm{sp}}\left\{\cap_{ij}[U^*]\right\} = \mathrm{tr}_{\mathrm{sp}}\left\{\cap_{ij}[U]^*\right\}$, then $G_{ij} \in \mathbf{R}$

Note that this is satisfied if $S(\cap_{ij}[U^*])S^{-1} = (\cap_{ij}[U])^*$

Assertion[3]: For a theory of the form described above, $G_{ij} \in \mathbf{R}$, subject to the condition that for all vector-field operators $O[U]$ in $\cap_{ij}$, $O[U^*] = O^*[U]$.

2.2.2 Generalisation

Let us restrict ourselves to consideration of (possibly momentum-dependent) gauge-functionals $G(\vec{p})[U]$ which are eigenstates of charge conjugation, C and parity P.

That is to say,

$$\begin{aligned} G(\vec{p})[U] &= \mathrm{s_P} G(-\vec{p})[U] \\ G(\vec{p})[U] &= \mathrm{s_C} G^{\star}(\vec{p})[U^{\star}] \end{aligned}$$

Then one can make the replacement $G(\vec{p})[U] \to \frac{1}{2}(G(\vec{p})[U] \pm s_C s_P G^*(-\vec{p})[U^*])$ to obtain an improved estimator which is unbiased with respect to parity and charge conjugation. In all of our lattice codes we implement just such a step.

---

[3] proof on page 8

2.2.3 Proofs

If $\gamma_\mu = {\gamma_\mu}^\dagger, \mu = 0, 1, 2, 3$*, then* $S = C\gamma_5$*.*

Recall the commutator algebra for γ_5: $\{\gamma_5, \gamma_\mu\} = 0, {\gamma_5}^2 = 1$

Thus $\gamma_5\gamma_\mu\gamma_5 = -\gamma_\mu$

Also recall the action of the charge conjugation operator upon the gamma matrices: $C\gamma_\mu C^{-1} = -{\gamma_\mu}^T$

Therefore $S\gamma_\mu S^{-1} = {\gamma_\mu}^T = ({\gamma_\mu}^\dagger)^T = {\gamma_\mu}^*$ where $S = C\gamma_5$ ∎

For Clover-like Action, $M[U] = M[U^*]$*.*

$$M[U] = \sum_{\mu,\nu} (real.\gamma_\mu + real.U_\mu.\gamma_\mu + i\sigma_{\mu\nu}F^{\mu\nu}[U])$$

Then

$$SM[U^*]S^{-1} = \left(\sum_{\mu,\nu} \left(real.\gamma_\mu^* + real.U_\mu^*.\gamma_\mu^* - i\sigma_{\mu\nu}^*(F^{\mu\nu}[U])^*\right)\right) = M[U]^* \quad ∎$$

$S(\cap_{ij}[U^*])S^{-1} = (\cap_{ij}[U])^*$ *for given theory.*

The terms denoted collectively by $\cap_{ij}$ will most generally be of the following types:

- Gamma matrices - and we have shown that $S\gamma_\mu S^{-1} = \gamma_\mu^*$.
- Propagators: These will be of the form $M^{-1}[U]$, and since inversion and complex conjugation are orthogonal operations, $SM[U^*]^{-1}S^{-1} = (M[U]^{-1})^*$ by the properties of M.
- Vector-field operators $O[U]$: These will not posess Dirac indices, so we will require that $O[U^*] = (O[U])^*$.

  For example $iF_{\mu\nu}[U^*] = -i(-F_{\mu\nu}^*[U]) = iF_{\mu\nu}[U]$.
- Products of the above types of terms: These we can split up by inserting SS^{-1} between terms, so they add nothing to the discussion.

Thus if $O[U^*] = (O[U])^*$, then we have shown that $S(\cap_{ij}[U^*])S^{-1} = (\cap_{ij}[U])^*$. ∎

3

Mesons from LQCD

3.1 Introduction

As low-lying states in the QCD spectrum, mesons (via the variational structure of the action) play a crucial role in mediating the exchange force between particles such as the proton or neutron. Indeed, various successful models or effective field theories have been constructed by simply considering the π and K (χPT), and sometimes the ρ (e.g Vector Meson Dominance).

3.2 Meson correlation functions at the hadronic level

3.2.1 Lorentz Scalar fields

Consider $G_{ij}(\vec{p},t) = \int d^3x\ e^{-i\vec{p}.\vec{x}}\,\langle 0|\chi_i(\vec{x},t)\bar{\chi}_j(0)|0\rangle$, with subscripts i and j there to remind us we could have different operators involved in creation and annhilation.

Suppose that $\bar{\chi}_i|0\rangle$ and $\bar{\chi}_j|0\rangle$ both have overlap with N different states. Label these states by $|n,\vec{p}\rangle$ where $n \in \{1,..,N\}$.

We shall take the normalisation of these states to be such that

$$\sum_{n=1}^{N}\int \frac{d^3p'}{(2\pi)^3}|n,\vec{p'}\rangle\langle n,\vec{p'}| = 1\,.$$

Then

$$G_{ij}(\vec{p},t) = \sum_{n=1}^{N}\int \frac{d^3p'}{(2\pi)^3}\int d^3x\ e^{-i\vec{p}.\vec{x}}\left\langle 0|\chi_i(\vec{x},t)|n,\vec{p'}\rangle\langle n,\vec{p'}|\bar{\chi}_j(0)|0\right\rangle\,.$$

Next, we invoke translation invariance to write:

$$\chi(\vec{x},t) = e^{i\hat{H}t}e^{-i\hat{\vec{P}}.\vec{x}}\chi(0)e^{i\hat{\vec{P}}.\vec{x}}e^{-i\hat{H}t}$$

We can thus rewrite $G(\vec{p},t)$ as follows:

$$G_{ij}(\vec{p},t) = \sum_{n=1}^{N}\int \frac{d^3p'}{(2\pi)^3}\int d^3x\ e^{-i\vec{p}.\vec{x}}\left\langle 0|e^{i\hat{H}t}e^{-i\hat{\vec{P}}.\vec{x}}\chi_i(0)e^{i\hat{\vec{P}}.\vec{x}}e^{-i\hat{H}t}|n,\vec{p'}\rangle\langle n,\vec{p'}|\bar{\chi}_j(0)|0\right\rangle$$

Now, $\langle 0|e^{i\hat{H}t}e^{-i\hat{\vec{P}}.\vec{x}} = \langle 0|$, and $e^{i\hat{\vec{P}}.\vec{x}}e^{-i\hat{H}t}|n,\vec{p'}\rangle = e^{i\vec{p'}.\vec{x}}e^{-iE_nt}|n,\vec{p'}\rangle$, thus:

$$G_{ij}(\vec{p},t) = \sum_{n=1}^{N} \int \frac{d^3p'}{(2\pi)^3} \int d^3x \; e^{-i\vec{p}.\vec{x}} e^{i\vec{p'}.\vec{x}} e^{-iE_nt} \left\langle 0|\chi_i(0)|n,\vec{p'}\rangle\langle n,\vec{p'}|\bar{\chi}_j(0)|0\right\rangle$$

Thus, finally:

$$G_{ij}(\vec{p},t) = \sum_{n=1}^{N} e^{-iE_nt} \left\langle 0|\chi_i(0)|n,\vec{p'}\rangle\langle n,\vec{p'}|\bar{\chi}_j(0)|0\right\rangle \tag{3.1}$$

If we continue this expression to Euclidean space-time $(t \to -it_E)$, we get the equivalent expression:

$$G_{ij}(\vec{p},t) = \sum_{n=1}^{N} e^{-E_nt_E} \left\langle 0|\chi_i(0)|n,\vec{p'}\rangle\langle n,\vec{p'}|\bar{\chi}_j(0)|0\right\rangle \tag{3.2}$$

If we have N distinct creation operators χ_i and N distinct annhilation operators χ_j , then we can construct the $N \times N$ matrix G, whose components are given above. Note that G is not generally a symmetric matrix.

3.2.2 Lorentz Vector fields

Consider the momentum-space meson two-point function for $t > 0$,

$$G^{ij}_{\mu\nu}(t,\vec{p}) = \int d^3x \; e^{-i\vec{p}\cdot\vec{x}} \langle\Omega|\chi^i_\mu(t,\vec{x})\chi^{j\dagger}_\nu(0,\vec{0})|\Omega\rangle \tag{3.3}$$

where i, j label the different interpolating fields and μ, ν label the Lorentz indices. At the hadronic level,

$$G^{ij}_{\mu\nu}(t,\vec{p}) \;=\; \int d^3x \; e^{-i\vec{p}\cdot\vec{x}} \int \frac{d^3p'}{(2\pi)^3} \sum_{n,s} \langle\Omega|\chi^i_\mu(t,\vec{x})|n,\vec{p}\,',s\rangle\langle n,\vec{p}\,',s|\chi^{j\dagger}_\nu(0,\vec{0})|\Omega\rangle$$

where the $|n,\vec{p}\,',s\rangle$ are a complete set of hadronic states, of energy n, momentum $\vec{p}\,'$, and spin s,

$$\int \frac{d^3p'}{(2\pi)^3} \sum_{n,s} |n,\vec{p}\,',s\rangle\langle n,\vec{p}\,',s| = I \; . \tag{3.4}$$

We shall denote the vacuum couplings as follows:

$$\begin{aligned} \langle\Omega|\,\chi^i_\mu\,|n,\vec{p}\,',s\rangle &= \lambda^i_n\,\epsilon_\mu(p\,',s) \\ \langle n,\vec{p}\,',s|\,\chi^{j\dagger}_\nu\,|\Omega\rangle &= \lambda^{j\star}_n\,\epsilon^\star_\nu(p\,',s) \end{aligned}$$

where the on-shell four-vector $p\,' = (E_n, \vec{p}\,')$ is introduced, with $E_n = \sqrt{\vec{p}^2 + m_n^2}$.

We can translate the sink operator from x to 0 to write this as

$$\begin{aligned}
& \int d^3x \int \frac{d^3p'}{(2\pi)^3} \sum_{n,s} e^{-i\vec{p}\cdot\vec{x}} \langle\Omega|\, \chi^i_\mu(0)\, e^{i\hat{\vec{P}}\cdot\vec{x}-\hat{H}t}\, |n,\vec{p}\,',s\rangle \\
& \times \langle n,\vec{p}\,',s|\, \chi^{j\,\dagger}_\nu(0)\, |\Omega\rangle \\
= \; & \sum_{n,s} e^{-E_n t} \langle\Omega|\chi^i_\mu|n,\vec{p},s\rangle\langle n,\vec{p},s|\chi^{j\,\dagger}_\mu|\Omega\rangle \\
= \; & \sum_{n,s} e^{-E_n t} \lambda^i_n \epsilon_\mu(p,s) \lambda^{j\star}_n \epsilon^\star_\nu(p,s)\ .
\end{aligned} \tag{3.5}$$

In general the number of states, N, in this tower of excited states may be very large, but we will only ever need to consider a finite set of the lowest energy states here, as higher states will be exponentially suppressed as we evolve to large Euclidean time. Finally, the transversality condition:

$$\sum_s \epsilon_\mu(p,s)\, \epsilon^\star_\nu(p,s) = -\left(g_{\mu\nu} - \frac{p_\mu p_\nu}{m^2}\right) \tag{3.6}$$

implies that for $\vec{p}=0$, we have

$$\begin{aligned}
& G^{ij}_{00}(t,\vec{0}) = 0 \\
& G^{ij}_{kl}(t,\vec{0}) = \sum_n \delta_{kl}\, \lambda^i_n\, \lambda^{j\star}_n\, e^{-m_n t}\ .
\end{aligned} \tag{3.7}$$

Since G^{ij}_{11}, G^{ij}_{22},and G^{ij}_{33} are all estimates for the same quantity we add them together to reduce variance, forming the sum

$$G^{ij} = G^{ij}_{11} + G^{ij}_{22} + G^{ij}_{33}\ .$$

Evolving to large Euclidean time suppresses higher mass states exponentially with respect to the lowest-lying, leading to the following definition of the effective mass

$$M^{ij}_{\text{eff}}(t) = \ln\left(\frac{G^{ij}(t,\vec{0})}{G^{ij}(t+1,\vec{0})}\right) \tag{3.8}$$

The presence of a plateau in M_{eff} as a function of time, then, signals that only the ground state signal remains.

3.3 Analysis

We can extract the masses and coupling strengths in G through the so-called “variational” approach. It is discussed briefly by McNeile *et al.* [40], but we will examine it here in some greater depth.

We seek to diagonalise our matrix of correlation functions in terms of mass eigenstates of the hamiltonian. This corresponds to maximising $v_i G_{ij}(t) u_j$ for constant $v_i G_{ij}(t - a) u_j$, where a is some integer, i.e finding all of the solutions of $v_i G_{ij}(t) u_j = \lambda v_i G_{ij}(t - a) u_j$ for some λ.

The presence of both u and v terms in these expressions is to allow for the fact that we may not in general have a symmetric matrix G - we may wish to treat source and sink operators differently (say, through a different smearing prescription).

We can cancel the v_i terms on both sides, and premultiply by $G^{-1}(t - a)$ to get the eigenvalue equation:

$$G^{-1}(t-a)G(t)\vec{u^{\alpha}} = (\lambda^{\alpha})^{a}\vec{u^{\alpha}} \tag{3.9}$$

To see how these eigenvalues are related to masses, it is instructive to consider the same procedure from a slightly different angle:

$$\text{Let } \phi^{\alpha} = u_k^{\alpha}\chi_k\,, \text{ s.t. } \phi^{\alpha}|n\rangle = z_1^{\alpha}\delta_{n\alpha}|n\rangle$$
$$\text{Let } \bar{\phi}^{\alpha} = v_k^{*\alpha}\chi_k\,, \text{ s.t. } \langle n|\bar{\phi}^{\alpha} = z_2^{*\alpha}\delta_{n\alpha}\langle n|\,,$$

where χ_k is the k'th interpolator. Then, expanding in an orthonormal basis, we have that

$$\int d^3x e^{-i\vec{p}.\vec{x}}\langle\phi^{\alpha}(\vec{x},t)\bar{\phi}^{\beta}(0)\rangle\Big|_{\vec{p}=0} = z_1^{\alpha}z_2^{*\alpha}\delta^{\alpha\beta}e^{-m_{\alpha}t}$$

$$\text{i.e.,}\quad v_i^{*\alpha}G_{ij}(t)u_j^{\beta} = \sum_{\gamma} v_i^{*\alpha}Z_{ij}^{\gamma}e^{-m_{\gamma}t}u_j^{\beta} = z_1^{\alpha}z_2^{*\alpha}\delta^{\alpha\beta}e^{-m_{\alpha}t} \tag{3.10}$$

$$\text{i.e.,}\quad z_1^{\alpha}z_2^{*\alpha} = v_i^{*\alpha}Z_{ij}^{\alpha}u_j^{\alpha}$$

If $v_i^{*\alpha}u_j^{\alpha} \neq 0$, we can divide through by this term to recover the corresponding Z_{ij}^{α}. Premultiplying Eq. (3.10) by u_i^{α} gives:

$$u_i^{\alpha}v_i^{*\alpha}G_{ij}(t)u_j^{\beta} = z_1^{\alpha}z_2^{*\alpha}e^{-m_{\alpha}t}u_i^{\beta} = e^{-am_{\alpha}}u_i^{\alpha}v_i^{*\alpha}G_{ij}(t-a)u_j^{\beta}$$

Provided that $u_i^{\alpha}v_i^{*\alpha} \neq 0$ (satisfied automatically for symmetric G), we can divide both sides of this equation by this term, to give us our final result:

$$G_{ij}(t)u_j^{\beta} = e^{-am_{\alpha}}G_{ij}(t-a)u_j^{\beta} \tag{3.11}$$

We recognise this as Eq. (3.9), making the identification that $\lambda^{\alpha} = e^{-m_{\alpha}}$. Note that we can also construct an equivalent left-eigenvalue equation and thus recover the v terms. Also note that the u, (and hence v) vectors are still real since both the matrix G and the eigenvalues λ^{α} are real.

In practice we calculate our correlation functions on the lattice in a discrete approximation to our path integral, a finite sum over some carefully chosen gauge fields. Further, we do not calculate these quantities in a continuum. Therefore we can expect error in our quantities. Last, it may be that the correlation functions are too computationally expensive for us to construct an $N \times N$ matrix where N is the number of states in the system.

Let us now consider the case where there are N states in the system, and we have only M distinct creation and M distinct annhilation operators, with $M < N$.

In this case we can write our correlation matrix as follows:

$$\begin{aligned}
G_{ij}(\vec{p},t) &= \sum_{n=1}^{N}\sum_{s} e^{-E_n t_E}\,\langle 0|\chi_i(0)|n,p',s\rangle\langle n,p',s|\bar{\chi_j}'(0)|0\rangle \\
&= \sum_{n=1}^{M}\sum_{s} e^{-E_n t_E}\,\langle 0|\chi_i(0)|n,p',s\rangle\langle n,p',s|\bar{\chi_j}'(0)|0\rangle \\
+ \quad & \sum_{k=M}^{N}\sum_{s} e^{-E_k t_E}\,\langle 0|\chi_i(0)|k,p',s\rangle\langle k,p',s|\bar{\chi_j}'(0)|0\rangle
\end{aligned}$$

We shall now write this symbolically as $G = \tilde{G} + E$. $\tilde{G}$ is an $M \times M$ matrix with M exponential terms with real coefficients, and in the case of a symmetric G, these will be all positive, so if we could somehow remove the higher order exponential terms that we have collected into E we would be in the same position we were in earlier, save that we are fitting with M masses vs. N.

This brings us to the crux of the problem - “How can we get rid of these higher terms?”. Since these terms will have larger negative coefficents of t_E in the exponentials, we expect that if we diagonalise G and examine the logarithms of the eigenvalues that these will become independent of t_E at sufficiently large t_E, indicating that the contributions of these higher correlation functions at large t_E we find that the statistical error in our measurements become large. At small t_E, where our statistical errors are small (and where our correlations are large), we will generally have a strong contribution from these higher states. Thus we are in need of a solution.

The simplest approach is to increase M - thus providing us with a better approximation to the full spectrum of masses. To think of it another way we are introducing an extra degree of freedom for our rotation to single-mass states, thus allowing more flexibility (and hence noise-resistance). In principle, the computational effort goes as M^2, so simultaneous extraction of 3 states is 9 times as expensive as the extraction of the ground state. In practice, however, we rarely have a large number of independent operators, and implementations of this procedure grow in sensitivity to error with rank, so we rarely employ $M > 3$.

3.4 Meson correlation functions at quark level

3.4.1 Mesonic operators from the naive quark model

The naive quark model approximates the mesons of gauge field theory as a bound state of a quark and an antiquark, where the quantum numbers of this bound state are then determined by the relative angular momentum of the quark-antiquark pair. In a spinor representation, this corresponds to mixing different elements of the quark and antiquark spinors together via Dirac gamma-matrices.

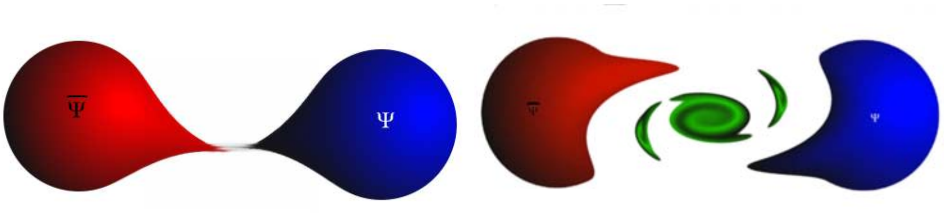

Fig. 3.1: Author's sketch of a quark-model meson vs a hybrid meson

Recall that under a Lorentz transform, we have that:

$$\bar{\psi}\mathcal{O}\psi \to \bar{\psi}\Lambda_{\frac{1}{2}}^{-1}\mathcal{O}\Lambda_{\frac{1}{2}}\psi$$

If $\mathcal{O}_\mu$ is a Lorentz vector, then we can write this as

$$\bar{\psi}\Lambda_{\frac{1}{2}}^{-1}\mathcal{O}_\nu\Lambda_{\frac{1}{2}}\psi = \Lambda_\mu^\nu\bar{\psi}\mathcal{O}_\nu\psi$$

SO(3) rotations form a proper subgroup of the Lorentz transformations, and thus we can obtain the angular momentum from lorentz transformation properties of the field. A Lorentz scalar object must correspond to $J = 0$, and similarly a vector must correspond to $J = 1$.

3.5 Hybrid Mesons

3.5.1 Introduction

A hybrid meson is a boson formed by coupling quark-antiquark pairs with the gauge field in order to produce a colour singlet.

We consider the local interpolating fields summarized in Table 3.1. Gauge-invariant Gaussian smearing [24, 52] is applied at the fermion source ($t = 8$), and local sinks are used to maintain strong signal in the two-point correlation functions. Chromo-electric and -magnetic fields are created from 3-D APE-smeared links [1, 22] at both the source and sink using the highly-improved $\mathcal{O}(a^4)$-improved lattice field strength tensor [11] described in greater detail below.

Some comments can already be made, however. In the non-relativistic limit, the lower components of the spinor become small relative to the upper components, and vice versa for the antispinor. So we expect strong signal from operators which are skew-diagonal and thus couple the large components of the spinor with the large components of the antispinor. Additionally, our hybrid operators will be expected to have larger statistical fluctuations since we are including more information about our finite ensemble of gauge fields. Thus we do not expect good signal for our 0^{--} meson interpolator, nor for the 0^{+-} interpolator $i\bar{q}^a\gamma_5\gamma_j B_j^{ab} q^b$. For the remaining 0^{+-} operator, we note with Bernard *e*t.

Table 3.1: J^{PC} quantum numbers and their associated meson interpolating fields.

0^{++}	0^{+-}	0^{-+}	0^{--}
$\bar{q}^a q^a$	$i\bar{q}^a \gamma_5 \gamma_j B_j^{ab} q^b$	$\bar{q}^a \gamma_5 q^a$	$\bar{q}^a \gamma_5 \gamma_j E_j^{ab} q^b$
$\bar{q}^a \gamma_j E_j^{ab} q^b$	$\bar{q}^a \gamma_4 q^a$	$\bar{q}^a \gamma_5 \gamma_4 q^a$	
$i\bar{q}^a \gamma_j \gamma_4 \gamma_5 B_j^{ab} q^b$		$i\bar{q}^a \gamma_j B_j^{ab} q^b$	
$\bar{q}^a \gamma_j \gamma_4 E_j^{ab} q^b$		$i\bar{q}^a \gamma_4 \gamma_j B_j^{ab} q^b$	
1^{++}	1^{+-}	1^{-+}	1^{--}
$\bar{q}^a \gamma_5 \gamma_j q^a$	$\bar{q}^a \gamma_5 \gamma_4 \gamma_j q^a$	$\bar{q}^a \gamma_4 E_j^{ab} q^b$	$i\bar{q}^a \gamma_5 B_j^{ab} q^b$
$i\bar{q}^a \gamma_4 B_j^{ab} q^b$	$\bar{q}^a \gamma_5 \gamma_4 E_j^{ab} q^b$	$i\epsilon_{jkl} \bar{q}^a \gamma_k B_l^{ab} q^b$	$\bar{q}^a \gamma_4 \gamma_j q^a$
$\epsilon_{jkl} \bar{q}^a \gamma_k E_l^{ab} q^b$	$\bar{q}^a \gamma_5 E_j^{ab} q^b$	$i\epsilon_{jkl} \bar{q}^a \gamma_4 \gamma_k B_l^{ab} q^b$	$\bar{q}^a E_j^{ab} q^b$
$\epsilon_{jkl} \bar{q}^a \gamma_k \gamma_4 E_l^{ab} q^b$	$i\bar{q}^a B_j^{ab} q^b$	$\epsilon_{jkl} \bar{q}^a \gamma_5 \gamma_4 \gamma_k E_l^{ab} q^b$	$\bar{q}^a \gamma_j q^a$
			$i\bar{q}^a \gamma_4 \gamma_5 B_j^{ab} q^b$

al [10] that the interpolating field $\bar{q}\gamma_4 q$ corresponds to the operator for Baryon number and is thus expected to be zero.

3.5.2 Method

Fat-Link Irrelevant Fermion Action

Propagators are generated using the fat-link irrelevant clover (FLIC) fermion action [54] where the irrelevant Wilson and clover terms of the fermion action are constructed using fat links, while the relevant operators use the untouched (thin) gauge links. Fat links are created via APE smearing [1, 22]. In the FLIC action, this reduces the problem of exceptional configurations encountered with clover actions [12], and minimizes the effect of renormalization on the action improvement terms [31]. Access to the light quark mass regime is enabled by the improved chiral properties of the lattice fermion action [12]. By smearing only the irrelevant, higher dimensional terms in the action, and leaving the relevant dimension-four operators untouched, short distance quark and gluon interactions are retained. Details of this approach may be found in reference [54]. FLIC fermions provide a new form of nonperturbative $\mathcal{O}(a)$ improvement [12,31] where near-continuum results are obtained at finite lattice spacing.

Gauge Action

We use quenched-QCD gauge fields created by the CSSM Lattice Collaboration with the $\mathcal{O}(a^2)$ mean-field improved Lüscher-Weisz plaquette plus rectangle gauge action [38]

i_κ	κ	m_π
1	0.12780	0.8356(14)
2	0.12830	0.7744(15)
3	0.12885	0.7012(15)
4	0.12940	0.6201(15)
5	0.12990	0.5354(16)
6	0.13025	0.4660(20)
7	0.13060	0.3732(79)
8	0.13080	0.3076(63)

Table 3.2: κ values, and corresponding pion masses (and uncertainties) in GeV.

using the plaquette measure for the mean link. The gauge-field parameters are defined by

$$\begin{aligned} S_G &= \frac{5\beta}{3} \sum_{\substack{x\,\mu\,\nu \\ \nu>\mu}} \frac{1}{3} \operatorname{Re} \operatorname{Tr} (1 - P_{\mu\nu}(x)) \\ &- \frac{\beta}{12\, u_0^2} \sum_{\substack{x\,\mu\,\nu \\ \nu>\mu}} \frac{1}{3} \operatorname{Re} \operatorname{Tr} (2 - R_{\mu\nu}(x)) \ , \end{aligned}$$

where $P_{\mu\nu}$ and $R_{\mu\nu}$ are defined in the usual manner and the link product $R_{\mu\nu}$ contains the sum of the rectangular 1×2 and 2×1 Wilson loops.

The CSSM configurations are generated using the Cabibbo-Marinari pseudo-heat-bath algorithm [16] using a parallel algorithm with appropriate link partitioning [13]. To improve the ergodicity of the Markov chain process, the three diagonal SU(2) subgroups of SU(3) are looped over twice [14] and a parity transformation [35] is applied randomly to each gauge field configuration saved during the Markov chain process.

Simulation Parameters

The calculations of meson masses are performed on $20^3 \times 40$ lattices at $\beta = 4.53$, which provides a lattice spacing of $a = 0.128(2)$ fm set by the Sommer parameter $r_0 = 0.49$ fm.

A fixed boundary condition in the time direction is used for the fermions by setting $U_t(\vec{x}, N_t) = 0 \; \forall \; \vec{x}$ in the hopping terms of the fermion action, with periodic boundary conditions imposed in the spatial directions.

Eight quark masses are considered in the calculations and the strange quark mass is taken to be the third heaviest quark mass. This provides a pseudoscalar mass of 701 MeV which compares well with the experimental value of $(2M_K^2 - M_\pi^2)^{1/2} = 693\,\mathrm{MeV}$ motivated by leading order chiral perturbation theory. κ values and the corresponding pion masses are given in Table 3.2.

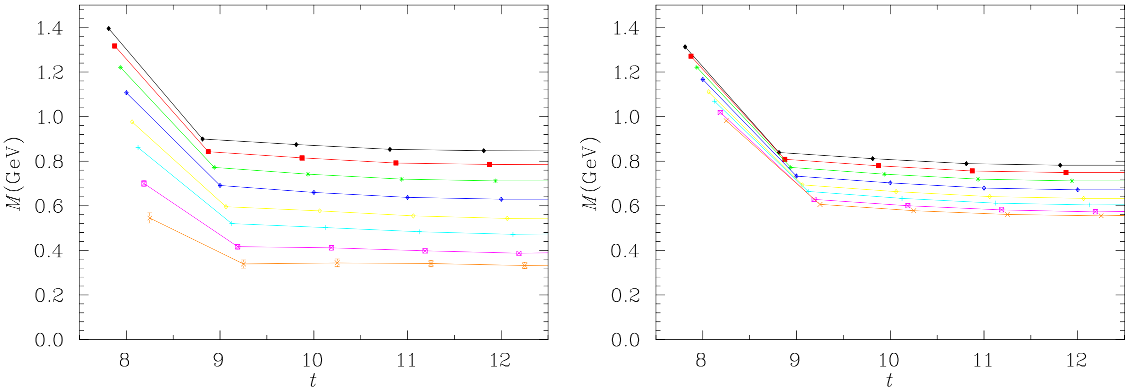

Fig. 3.2: Effective mass for standard pseudovector interpolating field, for equal (left) and unequal (right) quark-masses. Results are shown for all eight masses.

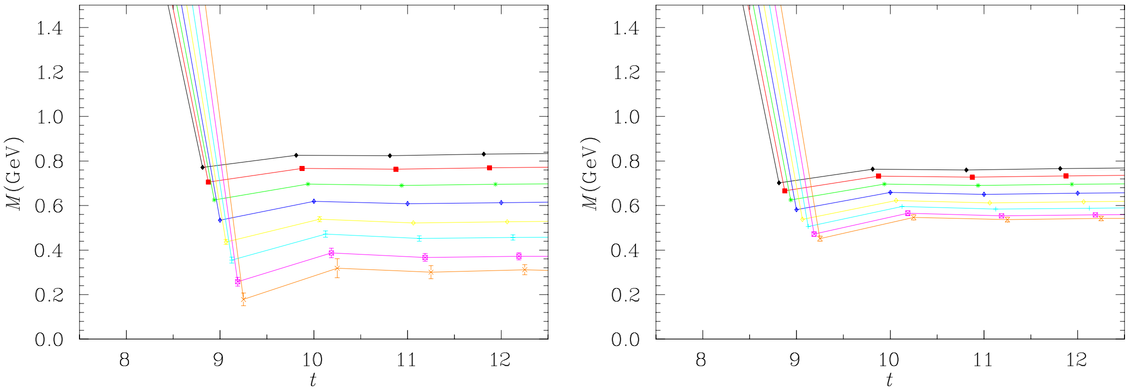

Fig. 3.3: Effective mass for axial-vector pion interpolating field, for equal (left) and unequal (right) quark-masses. Results are shown for all eight masses.

3.5.3 Results

π (pseudoscalar meson, $J^{PC} = 0^{-+}$)

The pseudoscalar channel gives an extremely strong signal – so strong that all four of our operators yield convincing plateaus. We can make use of this feature to extract excited state masses. The same is true for the K-mesons. In all results that follow, ‘unequal’ quark-antiquark masses means that we hold the quark mass fixed at our third heaviest quark mass (corresponding to the strange quark mass).

Figure 3.2 shows effective mass plots using the standard $\bar{q}\gamma_5 q$ pseudovector interpolating field. The statistical errors are very small, allowing us to determine masses with an uncertainty of less than 3%.

In Figure 3.3, we show the same plot for the alternative pion interpolator: $\bar{q}\gamma_5\gamma_4 q$, corresponding to the t-component of the four-vector operator $\bar{q}\gamma_5\gamma_\mu q$. A significant difference in excited-state information relative to the standard operator is seen close to the source, making the combination of this operator and the standard one an excellent choice

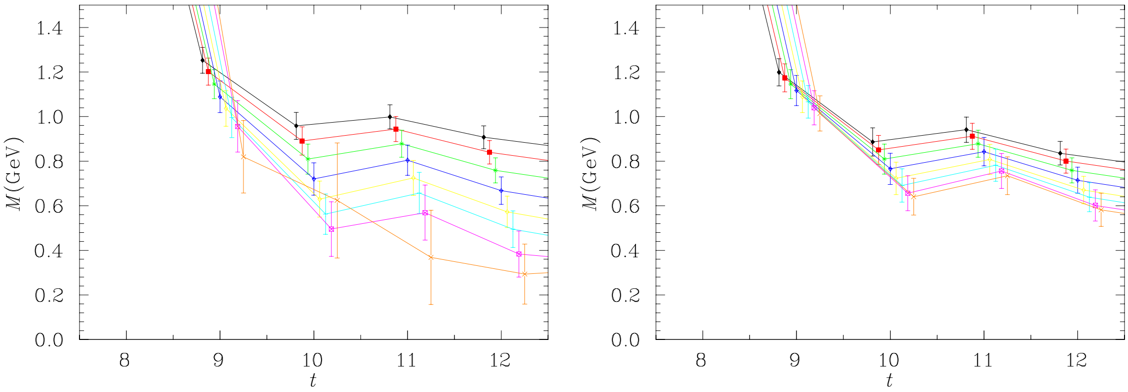

Fig. 3.4: Effective mass for the hybrid pion interpolating field $i\bar{q}^a\gamma_j B_j^{ab} q^b$, for equal (left) and unequal (right) quark-masses. Results are shown for all eight masses.

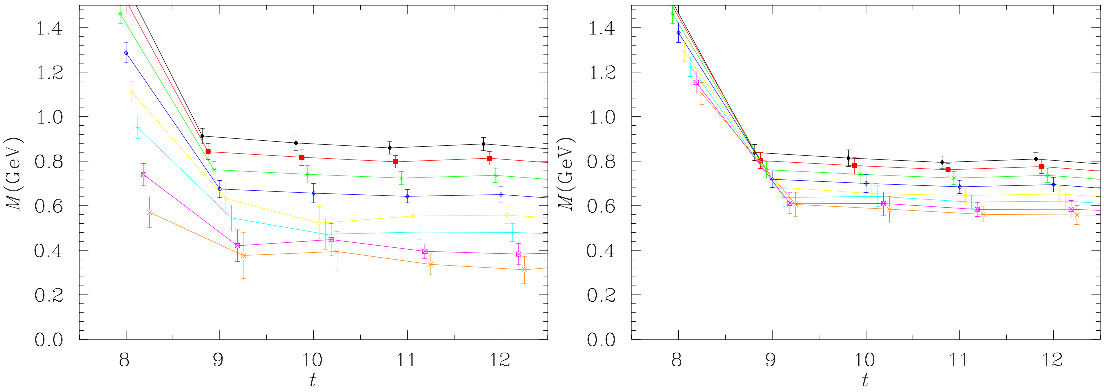

Fig. 3.5: Effective mass for the hybrid pion interpolating field $i\bar{q}^a\gamma_j\gamma_4 B_j^{ab} q^b$, for equal (left) and unequal (right) quark-masses. Results are shown for all eight masses.

for obtaining the first excited-state.

Figure 3.4 illustrates the behaviour of a hybrid pion derived from contracting a vector meson with the magnetic field. The signal exhibits significantly more jitter than the two conventional operators, but it is clear that the same ground state is being accessed.

In the non-relativistic limit, the two upper (lower) components of particle (antiparticle) spinors become large relative to the lower (upper) components. Both hybrid pion operators couple large-large and small-small components in this limit, but by introducing a relative minus sign via introduction of γ_4, as is done in Figure 3.5 significantly reduces both statistical fluctuations and curvature near the source, as we are excluding the first excited state by taking an axial-vector spinor structure.

The sources considered here are, as stated earlier, smeared sources corresponding to 48 sweeps of Gauge-invariant Gaussian smearing, with a smearing parameter $\alpha_{\rm src} = 0.7$. The procedure is defined precisely in the next chapter.

Using the interpolating fields $\chi_1 = \bar{q}\gamma_5 q$, $\chi_2 = \bar{q}\gamma_5\gamma_4 q$, and $\chi_3 = i\bar{q}^a\gamma_j B_j^{ab} q^b$, we can construct a matrix of correlation functions. From this, by the variational process described above, we can obtain more than just the ground state. Figure 3.6 shows the first excited-

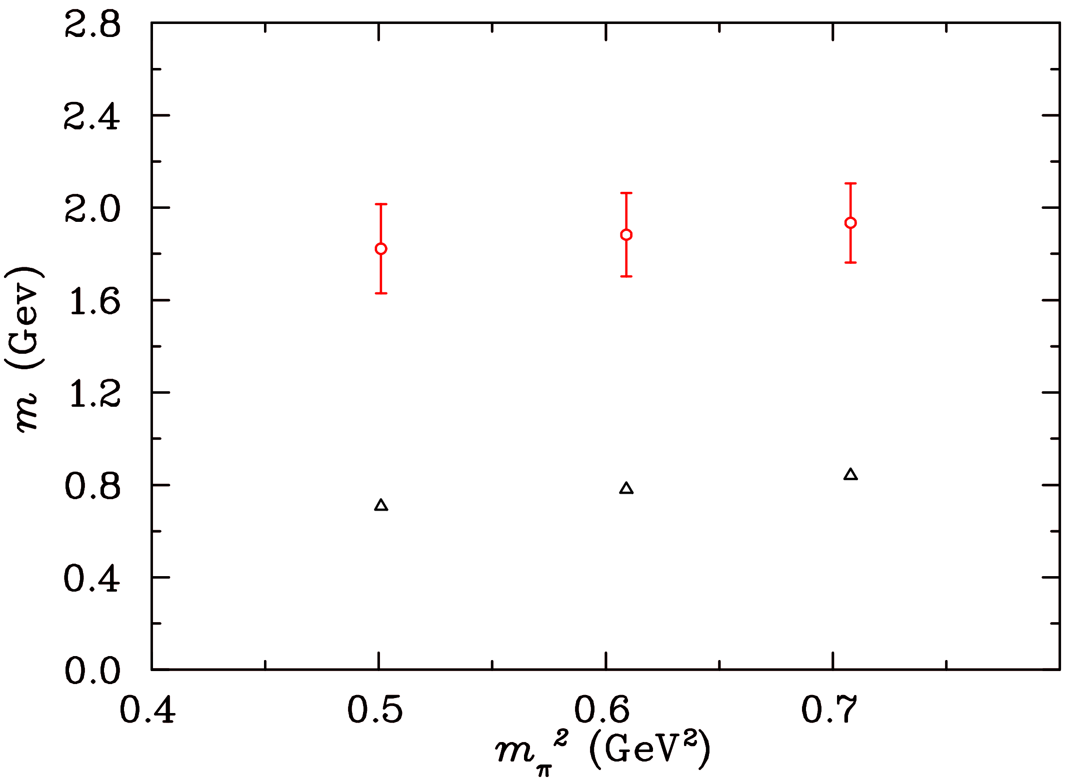

Fig. 3.6: Ground (triangles) and excited state (circles) masses for the pion, extracted using a 3×3 variational process using the first three pion interpolating fields. Signal is only obtained for the heaviest 3 quark masses.

state mass extracted using this process. Unfortunately, the sensitivity of the variational procedure to statistical noise precludes us from performing a fit below the SU(3) flavour limit. The data from which this graph was generated can be found in tables 3.3 and 3.4. For this calculation, the matrix diagonalisation was performed at $t = 9$.

a_0 *(scalar meson,* $J^{PC} = 0^{++}$*)*

The scalar channel is problematic, with a large decay width and considerable overlap with many other resonances and non $\bar{q}q$ objects such as glueballs. For an excellent discussion of the problem, see the section entitled ‘Note on scalar mesons’ in the PDG data book [21]. In our lattice simulations we admit the decay $a_0 \to \pi\eta'$ [8] (in full QCD, this would be $a_0 \to \pi\eta$, but in SU(2)-flavour the η and η' are the same particle). In the quenched approximation the η' is degenerate with the pion, so we will expect our calculations of effective mass to break down when the a_0 becomes heavier than twice the pion mass on the same lattice. We can observe just this occuring in Figure 3.7 where the correlation function becomes negative for intermediate times at the four lightest quark masses. Table 3.5 shows fitted effective mass of the a_0 vs the $\eta'\pi$ decay channel mass for the heaviest three quarks. We see that by the time we reach the SU(3) flavour limit the a_0

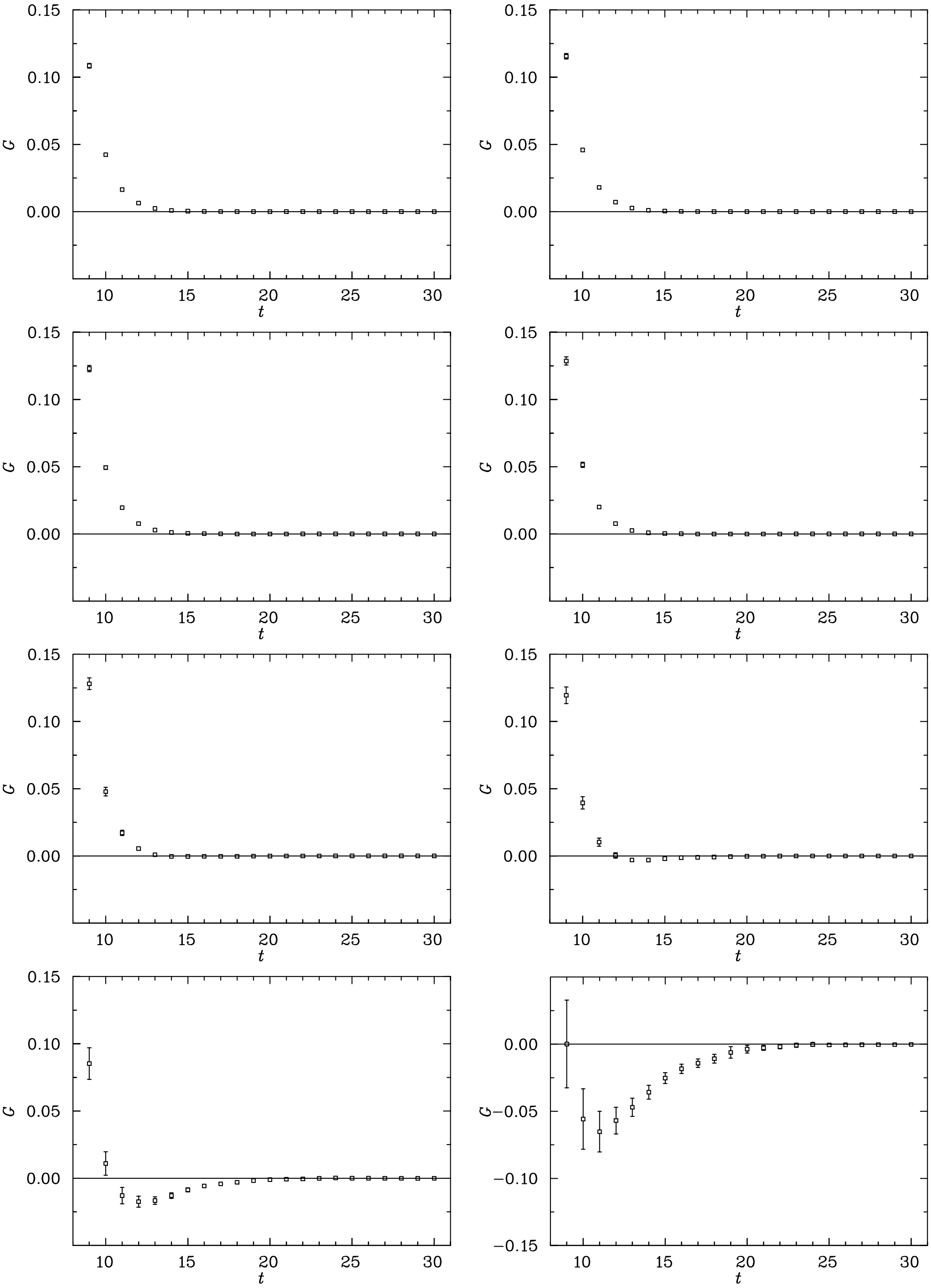

Fig. 3.7: The a_0 scalar meson correlation function vs. time.

Table 3.3: Pion ground-state mass fits from a 3×3 correlation matrix analysis. t_{start} and t_{end} denote the limits of the fit-window. Ma is the mass, in lattice units. σ is the uncertainty. $\chi^2/\text{d.o.f}$ is the χ^2 per degree of freedom of the fit. i_κ labels the κ value as per Table 3.2.

i_κ	t_{start}	t_{end}	Ma	σ	$\chi^2/\text{d.o.f}$
1	10	14	0.5458	0.0018	0.129
2	10	14	0.5063	0.0019	0.281
3	10	14	0.4592	0.0020	0.492

Table 3.4: Pion excited-state mass fit. Column labels are as for Table 3.3.

i_κ	t_{start}	t_{end}	Ma	σ	$\chi^2/\text{d.o.f}$
1	10	12	1.2551	0.1112	0.885
2	10	12	1.2216	0.1168	0.913
3	10	12	1.1821	0.1253	0.898

is already unbound on our lattice.

ρ *(vector meson,* $J^{PC} = 1^{--}$*)*

In the case of the ρ meson, we are able to extract information from 5 independent operators. The effective mass plots can be found in Figures 3.8 through 3.12. The ρ cannot decay to $\pi\pi$ as there is no way to produce a neutral flavour non-singlet from the vacuum in Quenched QCD [6]. The decay $\rho \to \pi\eta'$ is forbidden by G-parity, but even if it were not so forbidden, the η' is degenerate in mass with the π in quenched QCD, and the ρ mass is well below the energy of this state, which would be $2\sqrt{m_\pi + \frac{2\pi}{aL}}$, corresponding to approximately 1.1 GeV at our lightest quark mass.

It is instructive to contrast the results in Figures 3.8 and 3.9. As for the case of the π-meson interpolating fields, we see that by changing the relative sign between large-large and small-small terms in the spinor sum we can effect a significant reduction in excited state contamination.

Table 3.5: a_0 scalar meson mass vs decay channel mass.

$2m_\pi(GeV)$	$m_{a_0}(GeV)$
1.668(3)	1.453(12)
1.545(3)	1.430(15)
1.399(3)	1.416(20)

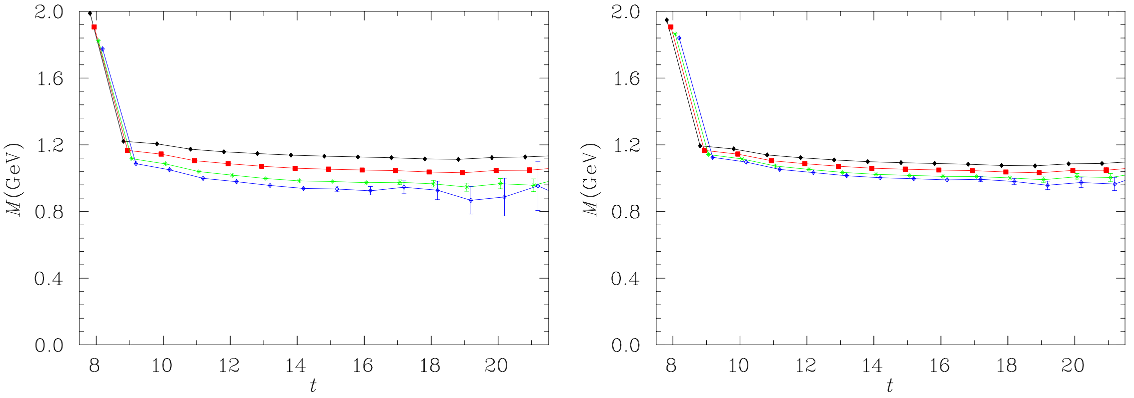

Fig. 3.8: ρ-meson effective mass derived from standard $\bar{q}\gamma_j q$ interpolator. Results are shown for both equal (left) and unequal (right) quark-antiquark masses. Results for every second quark mass are depicted.

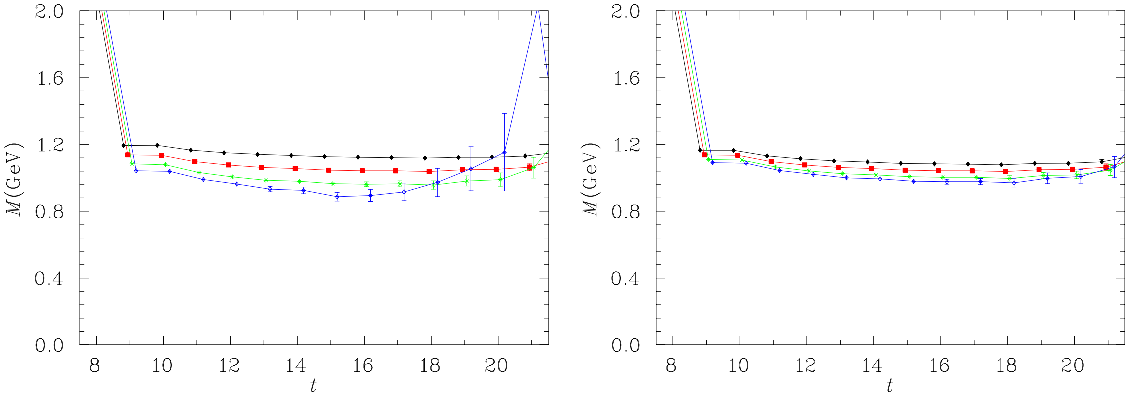

Fig. 3.9: ρ-meson (left) and K^* (right) effective mass plots derived from interpolator $\bar{q}\gamma_j\gamma_4 q$. Every second quark mass is depicted.

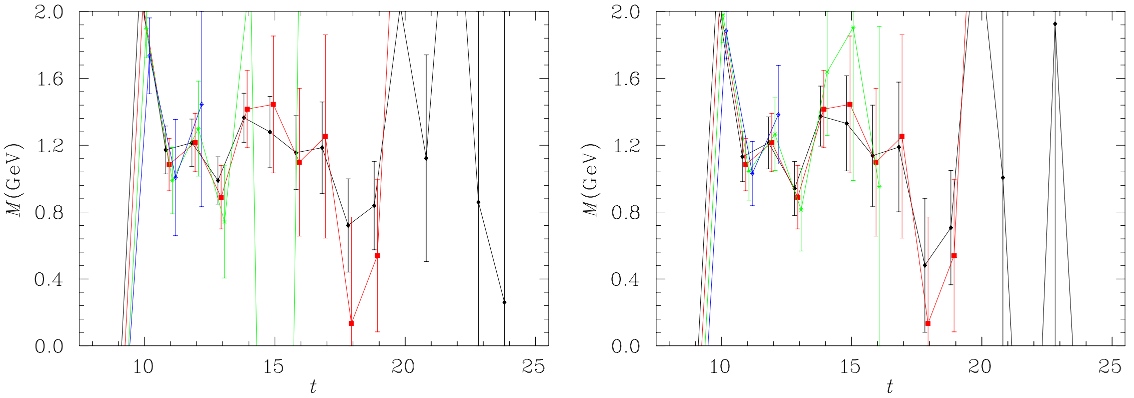

Fig. 3.10: Vector meson effective mass from hybrid interpolator $\bar{q}^a E_j^{ab} q^b$. Every second quark mass is depicted, and results are depicted for both ρ (left) and K^* (right) mesons.

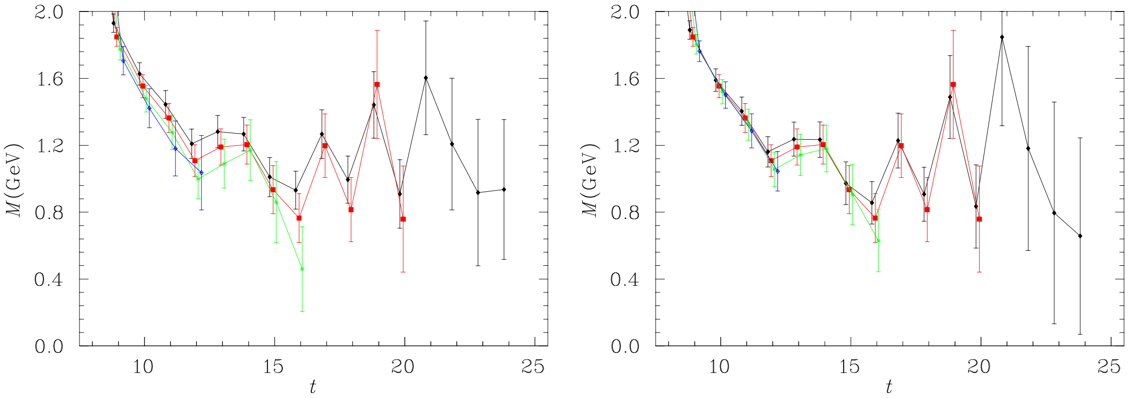

Fig. 3.11: Vector meson effective mass from hybrid interpolator $i\bar{q}^a\gamma_5 B_j^{ab} q^b$. Every second quark mass is depicted, and results are depicted for both ρ (left) and K^* (right) mesons.

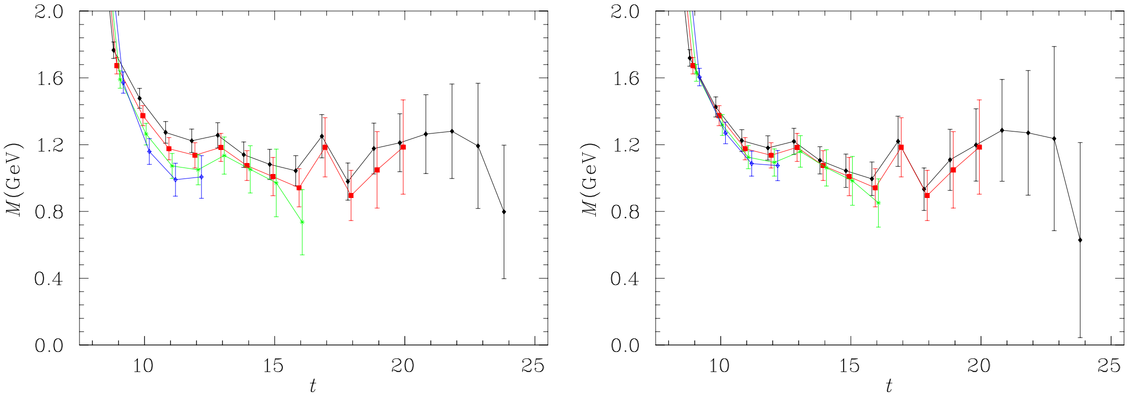

Fig. 3.12: Vector meson effective mass from hybrid interpolator $i\bar{q}^a\gamma_4\gamma_5 B_j^{ab} q^b$. Every second quark mass is depicted, and results are depicted for both ρ (left) and K^* (right) mesons.

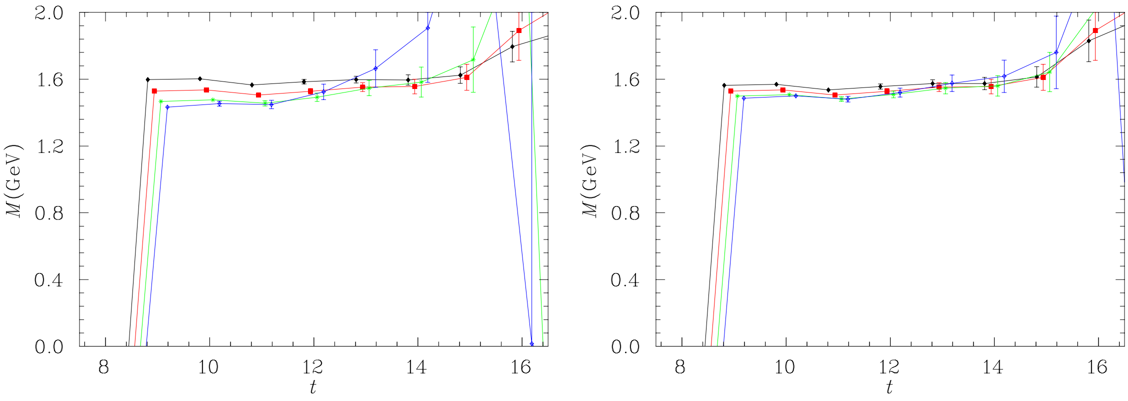

Fig. 3.13: Effective mass plots for a_1 axial-vector meson interpolator. Results are shown for light (left) and strange-light (right) quark-masses.

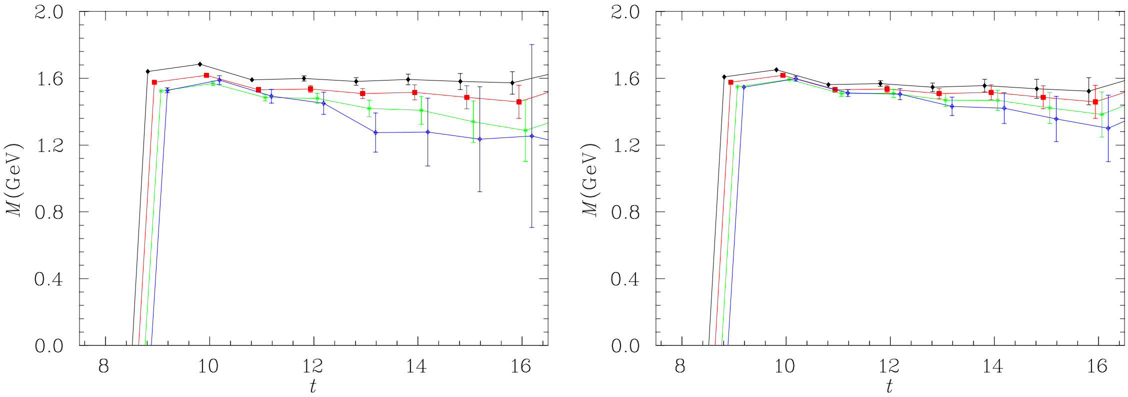

Fig. 3.14: b_1 axial-vector meson effective mass. Results are shown for both light (left) and strange-light (right) quark masses.

There are three available hybrid vector-meson interpolating fields. The strongest signal is obtained from the interpolator $i\bar{q}^a\gamma_4\gamma_5 B_j^{ab} q^b$. The results are compatible with the conventional operators, albeit with larger statistical uncertainties. It is clear that stronger signal is observed in those operators which couple the (non-relativistically) large-large components compared to those which couple the large to the small.

The $K^\star$ mesons extracted using these operators display qualitatively similar behaviour, although statistical fluctuations are reduced due to the presence of the strange quark, whose larger mass makes it less sensitive to it's gluonic environment.

axial-vector ($J^P = 1^+$)

Strong signal in the a_1 axial-vector channel is obtained via the use of interpolating field $\bar{q}\gamma_5\gamma_i q$. The resulting effective mass plots for both equal and unequal quark masses are shown in Figure 3.13. This signal shows strange behaviour at larger Euclidean times, but the correlation function does not become negative as in the scalar case.

For the b_1, only the non-hybrid operator provides a good signal, despite the fact that it

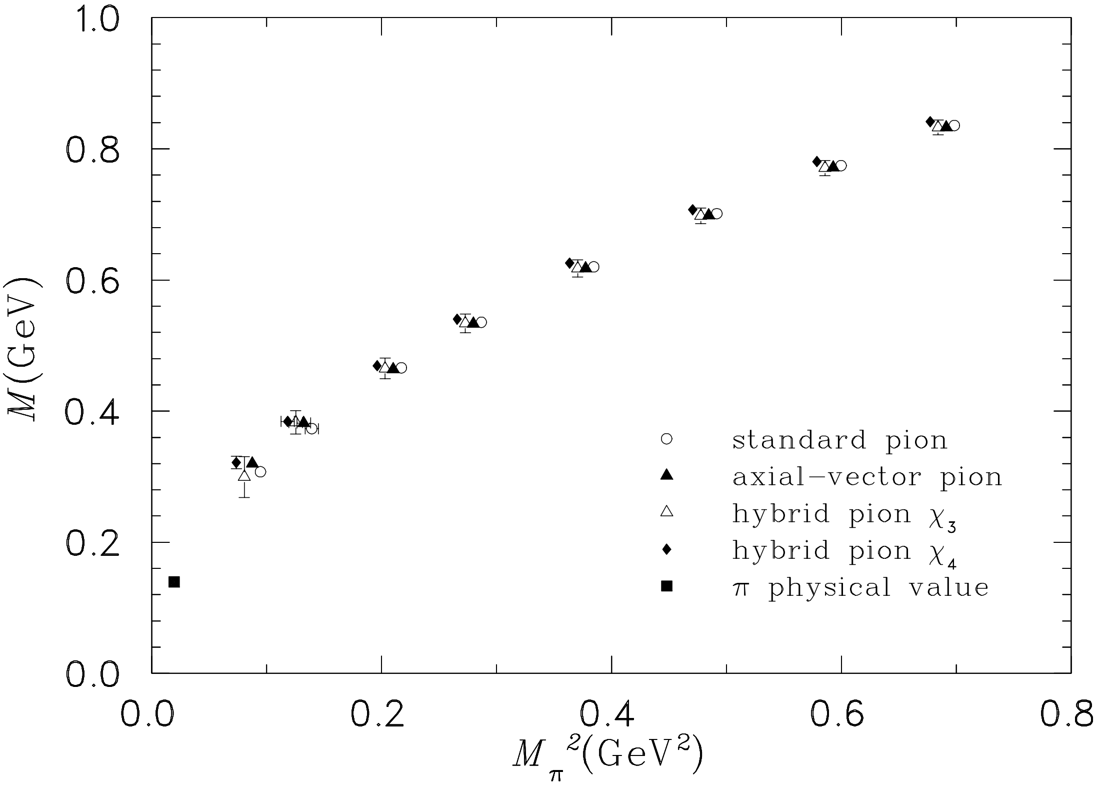

Fig. 3.15: Summary of results for pion interpolating fields. m_π^2, derived from the standard pion interpolator, provides a measure of the input quark mass.

couples large to small components. The interpolating field is:

$$\chi_{b_1} = \bar{q}\gamma_5\gamma_4\gamma_j q \,.$$

The effective mass is shown in Figure 3.14. The K_1 meson signal derived from this is also shown.

3.5.4 Summary

Now we move on to placing these results in context. Figure 3.15 shows results for all four of our π-meson interpolating fields. These demonstrate excellent agreement, indicating that our hybrid operators share the same ground state as the conventional interpolating fields. For an estimate of the systematic effects on these results due to quenching see [23]. For reference, the physical pion mass is also provided. Figure 3.16 is the corresponding plot for the K-meson results.

For the ρ (Figure 3.17), and K^* the same broad pattern applies. The results for each of our interpolating fields are consistent with each other. For the χ_3 ($\bar{q}^a E_j^{ab} q^b$) noise dominates over signal for the lightest quark mass, so this point is omitted. Recall that χ_3 couples large-small components, so we might expect it to behave thus. The situation is even more dramatic in the case of the K^*, where we have a signal only for the

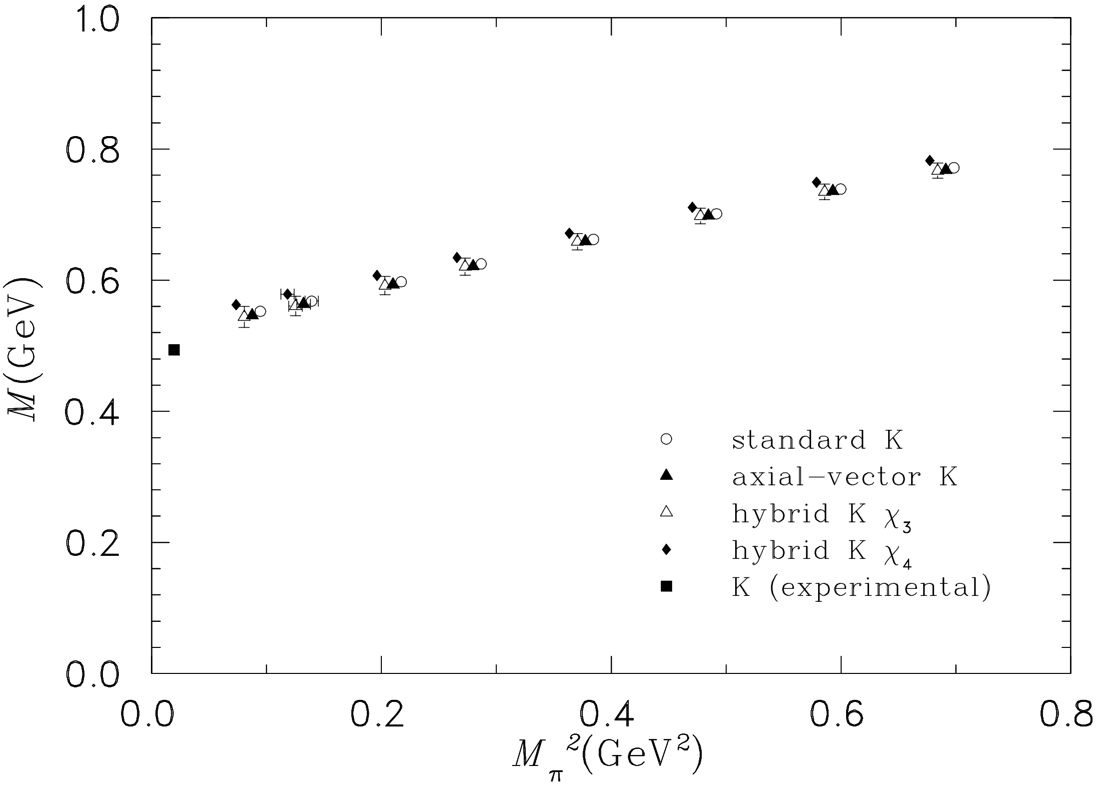

Fig. 3.16: Summary of results for K interpolating fields. m_π^2, derived from the standard pion interpolator, provides a measure of the input quark mass.

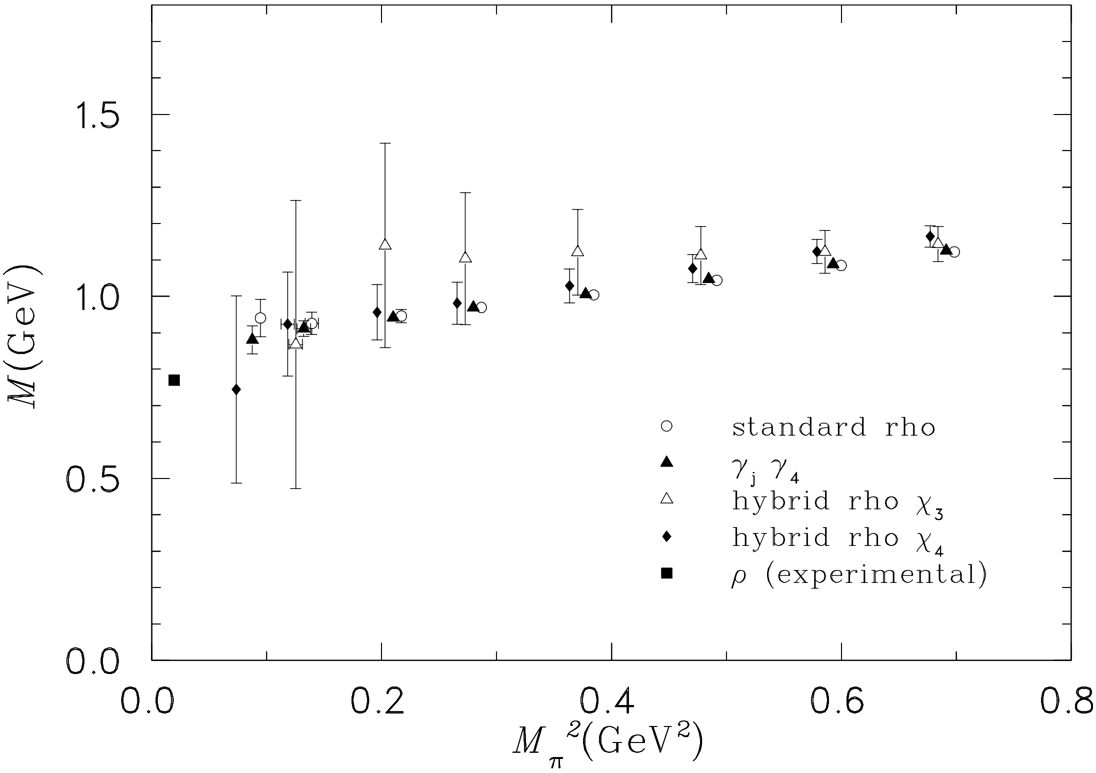

Fig. 3.17: Summary of results for ρ-meson interpolating fields. m_π^2, derived from the standard pion interpolator, provides a measure of the input quark mass.

four heaviest quark masses. Further discussion of the statistical errors associated with the hybrid operators can be found in the next chapter, where we demonstrate that the source-smearing prescription used for this study (48 sweeps of Gauge-invariant Gaussian smearing with $\alpha = 6$ is somewhat less than ideal.

It is instructive to compare the a_1 and b_1 mesons as in Figure 3.19, which lie at $1230(40)$ and $1230(3)$ MeV respectively according to the Particle Data Group [21]. The masses of the two particles are indistinguishable in our simulation, but sit somewhat above the experimental results. Little literature exists on the topic of the a_1 in lattice simulations, but a previous simulation [48] did not see this behaviour, returning an a_1 mass in agreement with the experimental value. It is, however, somewhat difficult to compare directly with this simulation as they have used a very different scheme to set the scale.

Curiously, it is the b_1 interpolator which shows the largest statistical errors, where the experimental situation has the largest uncertainties associated with the a_1.

This concludes our survey of local hybrid meson interpolating fields. The primary lesson has been the importance of constructing interpolating fields which have the large-large components coupled together. We now move on to the 1^{-+} exotic meson.

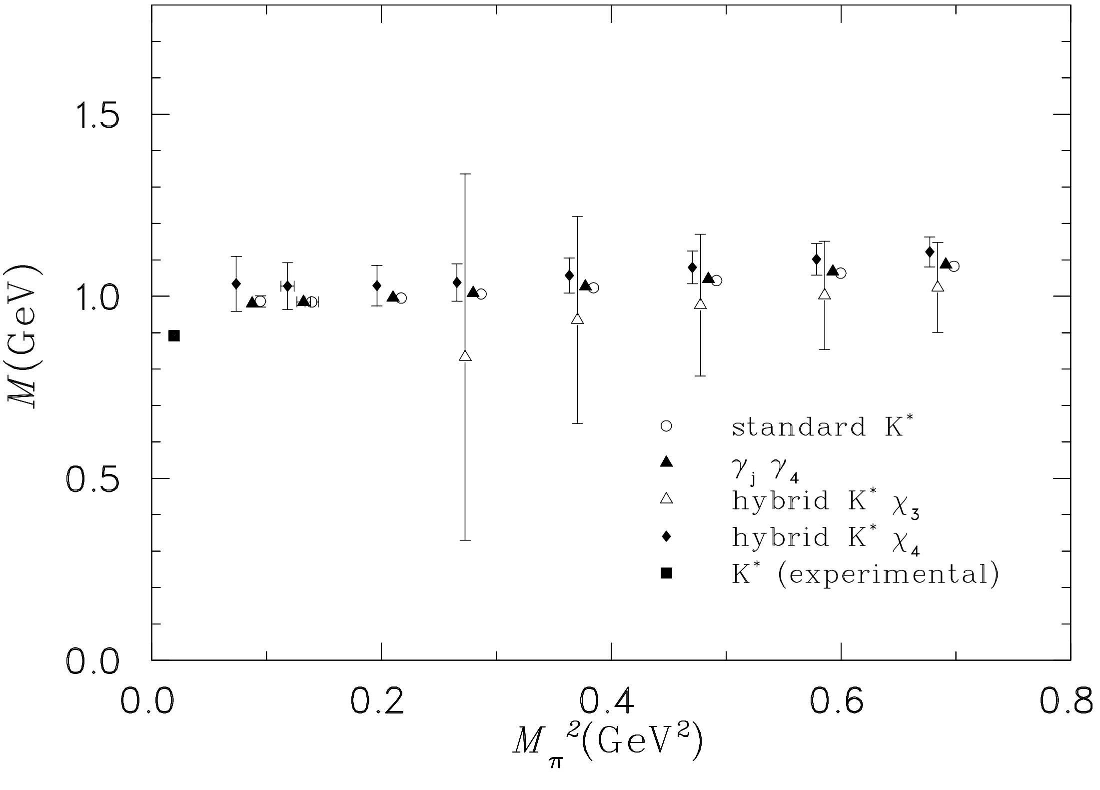

Fig. 3.18: Summary of results for K^*-meson interpolating fields. m_π^2, derived from the standard pion interpolator, provides a measure of the input quark mass.

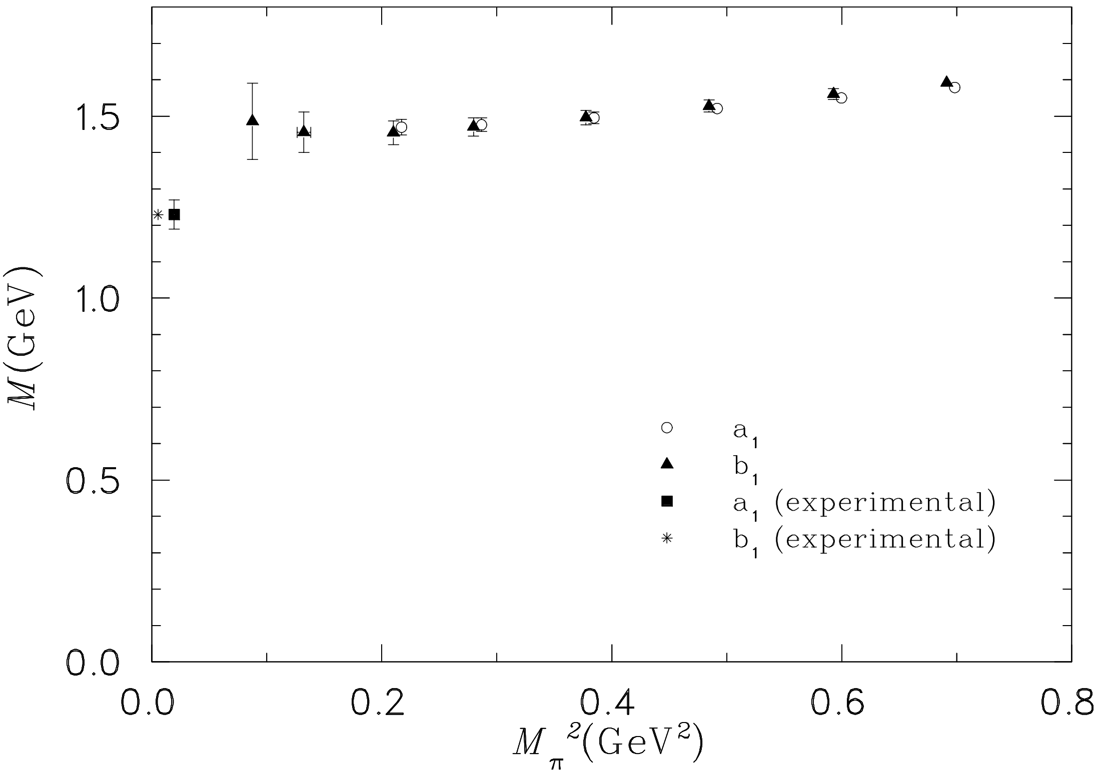

Fig. 3.19: Summary of results for pseudovector-meson interpolating fields. m_π^2, derived from the standard pion interpolator, provides a measure of the input quark mass.

3.6 Exotic Mesons

3.6.1 Introduction

A A $q\bar{q}$ system is an eigenstate of parity with $P = (-1)^{L+1}$. Charge conjugation applied to a neutral system provides $C = (-1)^{L+S}$. For $J = 1$, for example we can either have $L = 1, S = 0$, providing $(P, C) = (+-)$, or $L = 0, S = 1$, providing $(P, C) = (--)$. We cannot form, for example the state $J^{PC} = 1^{-+}$. Such states as these are called 'exotic'.

The characterisation of these so-called 'exotic' mesons is attracting considerable attention from the experimental community [2,17,37,43,46] as a vehicle for the elucidation of the relatively unexplored role of gluons in QCD. The E852 collaboration has published experimental results indicating an isovector 1^{-+} mass in the range $1.2 - 1.6$ GeV [17,37], and another 1^{-+} exotic state having a mass around 2 GeV [37]. Recently, Dzierba *et. al* have published a paper showing the absence of a signal for the $\pi_1(1600)$ in the $\pi_-\pi_-\pi_+$ and $\pi_-\pi_0\pi_0$ systems [20].

Early work in the field of light-quark lattice exotics has been performed by other groups . In [29], the UKQCD Collaboration made use of gauge-invariant non-local operators to explore P and D-wave mesons, as well as exotics. They used a tadpole-improved clover action, with 375 configurations for a $16^3 \times 48$ lattice and reported a 1^{-+} exotic mass of $1.9(4)$ GeV.

In 1997, the MILC Collaboration published [10], in which they used local operators formed by combining the gluon field strength tensor and standard quark bilinears, the same approach we have taken in this paper. They also used highly anisotropic lattices to allow many time slices to be used to determine the mass of the exotic, and used large $20^3 \times 48$ and $32^3 \times 64$ lattices with multiple fermion sources per lattice. The Wilson action was used throughout. They reported a possible 1^{-+} value of $1.97(9)$ GeV, but emphasised that extrapolation to the continuum was troublesome due to large errors.

The UKQCD collaboration then released [30], which updated their earlier work by using dynamical fermions. The new mass estimate for the 1^{-+} exotic was reported as $1.9(2)$ GeV.

Further work using the Clover action, but this time with Local interpolators was performed by Mei *et al.* [41]. Very heavy quark masses were used to get good control of statistical errors. Their extrapolation to the continuum predicted a mass of $2.01(7)$ GeV.

In 2002 the MILC Collaboration published new work [9] where they used dynamical improved Kogut-Susskind fermions on the same lattices as earlier, and compared these with both quenched and Wilson results. They quote two sets of results for the 1^{-+} mass corresponding to different choices of scale: $1.85(7)$ and $2.03(7)$ GeV.

Michael [42] provides a good summary of work to 2003, concluding that the light-quark exotic is predicted by lattice studies to have a mass of $1.9(2)$ GeV.

The hybrid exotic interpolating fields considered in this study are the following:

$$\begin{aligned} \chi_2 &= i\epsilon_{jkl}\bar{q}^a\gamma_k B_l^{ab} q^b \\ \chi_3 &= i\epsilon_{jkl}\bar{q}^a\gamma_4\gamma_k B_l^{ab} q^b. \end{aligned} \tag{3.12}$$

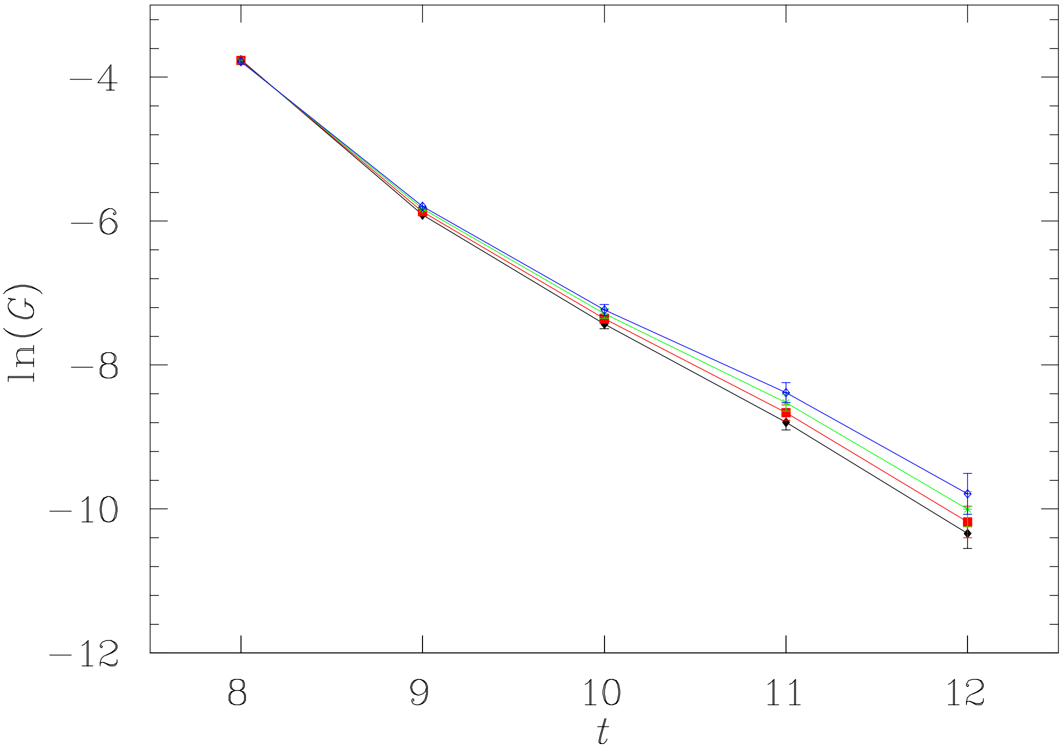

Fig. 3.20: Exotic meson propagator for interpolator χ_2. Results are shown for every 2nd quark mass in the simulation. Lower lines correspond to heavier quark masses. For all but the heaviest mass, the signal is lost after t=12. Pion masses corresponding to each quark mass may be found at the beginning of appendix A

Figures 3.20 and 3.21 show the natural log of the correlation functions calculated with interpolators χ_2 and χ_3 from Eq. (3.12) respectively. The curves become linear after two time slices from the source, corresponding to approximately 0.256 fm. This is consistent with Ref. [10], where a similar effect is seen after approximately 3 to 4 time slices, corresponding to 0.21 to 0.28 fm following the source.

Figures 3.22 and 3.23 show the effective mass for the two different interpolators. For clarity, we have plotted the results for every second quark mass used in our simulation. The plateaus demonstrate that we do indeed see an exotic signal in quenched lattice QCD. This is significant, as we expect the two interpolating fields to possess considerably different excited-state contributions, based on experience with pseudoscalar interpolators [25].

For example, the approach to the pion mass plateau is from above (below) for the pseudo-scalar (axial-vector) interpolating field as illustrated in Fig. 3.2 (Fig. 3.3) earlier in this chapter. This exhibits the very different overlap of the interpolators with excited states. As in the 1^{-+} interpolators, the role of γ_4 in the pion interpolators is to change the sign with which the large-large and small-small spinor components are combined.

We also present results for the strangeness ± 1 analogue of the 1^{-+} in Figs. 3.24 and 3.25.

Table 3.6 summarizes our results for the mass of the 1^{-+} meson, with the squared

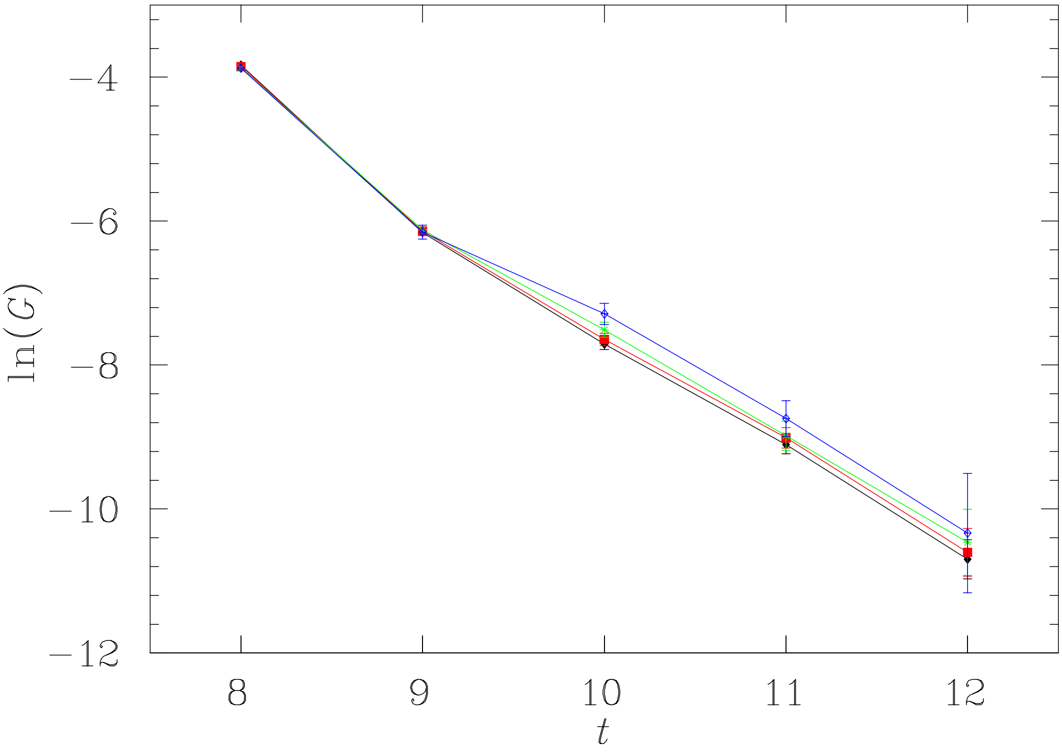

Fig. 3.21: Exotic meson propagator for interpolator χ_3. Results are shown for every 2nd quark mass in the simulation. Lower lines correspond to heavier quark masses.

pion-mass provided as a measure of the input quark mass. The agreement observed in the results obtained from the two different 1^{-+} hybrid interpolators provides evidence that a genuine ground-state signal for the exotic has been observed.

Table 3.7 summarizes our results for the mass of the strangeness ± 1, $J^P = 1^-$ meson.

Finally, in Fig. 3.26 we summarize a collection of results for the mass of 1^{-+} obtained in lattice QCD simulations thus far. The current results presented herein are compared with results from the MILC [9,10] and SESAM [30] collaborations, both of which provide a consistent scale via r_0.

Our results compare favorably with earlier work at large quark masses. Agreement within one sigma is observed for all the quenched simulation results illustrated by filled symbols. It is interesting that the dynamical Wilson fermion results of the SESAM collaboration [30] tend to sit somewhat higher as this is a well known effect in baryon spectroscopy [50, 51, 53, 54].

3.6.2 Physical Predictions

In comparing the results of quenched QCD simulations with experiment, the most common practice is to simply extrapolate the results linearly in m_q or m_π^2 to the physical values. However, such an approach provides no opportunity to account for the incorrect chiral nonanalytic behavior of quenched QCD [32, 33, 49, 50].

Table 3.6: 1^{-+} Exotic Meson mass m (GeV) vs square of pion mass m_π^2 (GeV^2).

m_π^2	χ_2 fit 10-11		χ_2 fit 10-12		χ_3 fit 10-11	
	m	χ^2/dof	m	χ^2/dof	m	χ^2/dof
0.693(3)	2.15(12)	0.69	2.16(11)	0.44	2.20(15)	0.45
0.595(4)	2.11(12)	0.77	2.12(11)	0.51	2.18(16)	0.46
0.488(3)	2.07(12)	0.85	2.08(12)	0.59	2.15(17)	0.41
0.381(3)	2.01(12)	0.91	2.03(12)	0.65	2.14(19)	0.29
0.284(3)	1.97(13)	0.78	1.98(13)	0.55	2.27(29)	0.00012
0.215(3)	1.92(14)	0.78	1.92(14)	0.40	2.25(31)	0.02
0.145(3)	1.85(17)	0.57	1.84(17)	1.76	2.26(37)	0.02
0.102(4)	1.80(23)	0.13	1.75(23)	3.04	2.46(58)	0.03

Table 3.7: Strangeness ± 1 1^{-} Meson mass m (GeV) vs square of pion mass m_π^2(GeV^2).

m_π^2	χ_2 fit 10-11		χ_2 fit 10-12		χ_3 fit 10-11	
	m	χ^2/dof	m	χ^2/dof	m	χ^2/dof
0.693(3)	2.11(12)	0.76	2.12(11)	0.51	2.17(16)	0.44
0.595(4)	2.09(12)	0.81	2.10(12)	0.55	2.16(16)	0.44
0.488(3)	2.07(12)	0.85	2.08(12)	0.59	2.15(17)	0.41
0.381(3)	2.04(12)	0.88	2.05(12)	0.63	2.15(18)	0.36
0.284(3)	2.01(13)	0.85	2.02(12)	0.63	2.25(20)	0.22
0.215(3)	1.99(13)	0.87	2.00(12)	0.64	2.11(20)	0.29
0.145(3)	1.97(13)	0.73	1.97(13)	0.54	2.12(22)	0.11
0.102(4)	1.96(14)	0.56	1.96(14)	0.39	2.09(24)	0.01

Unfortunately, little is known about the chiral nonanalytic behavior of the 1^{-+} meson. Ref. [45] provides a full QCD exploration of the chiral curvature to be expected from transitions to nearby virtual states and channels which are open at physical quark masses. While virtual channels act to push the lower-lying single-particle 1^{-+} state down in mass, it is possible to have sufficient strength lying below the 1^{-+} in the decay channels such that the 1^{-+} mass is increased [4, 34]. Depending on the parameters considered in Ref. [45] governing the couplings of the various channels, corrections due to chiral curvature are estimated at the order of $+20$ to -40 MeV.

Generally speaking, chiral curvature is suppressed in the quenched approximation. For mesons, most of the physically relevant diagrams involve a sea-quark loop and are therefore absent [4, 44]. However, the light quenched η' meson can provide new nonanalytic behavior, with the lowest order contributions coming as a negative-metric contribution through the double-hairpin diagrams. Not only do these contributions alter the 1^{-+} mass through self-energy contributions, but at sufficiently light quarks masses, open

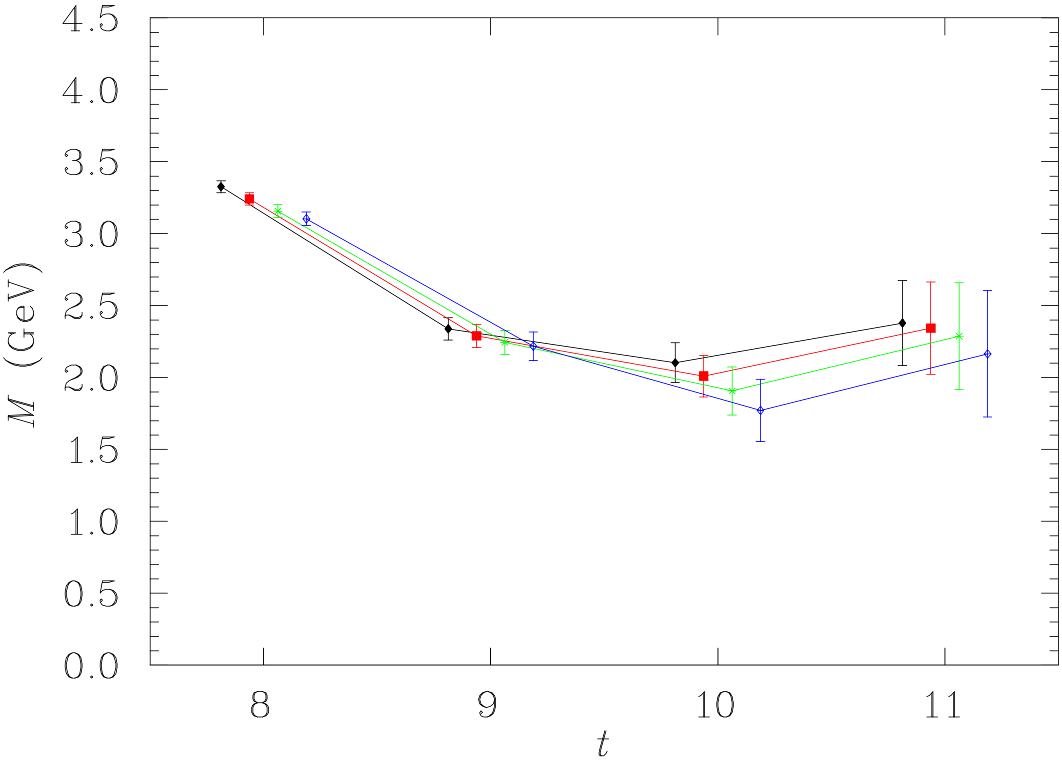

Fig. 3.22: Effective mass for interpolator χ_2. Plot symbols are as for the corresponding propagator plot.

decay channels can dominate the two-point correlator and render its sign negative.

For the quenched 1^{-+} meson, the $a_1\eta'$ channel can be open. Using the pion mass as the η' mass a direct calculation of the mass of an $a_1\eta'$ two-particle state indicates that the 1^{-+} hybrid lies lower than the two-particle state for heavy input quark mass. This indicates that the hybrid interpolator is effective at isolating a single-particle bound state as opposed to the two-particle state at heavy quark masses. This is particularly true for the case here, where long Euclidean time evolution is difficult.

As the light quark mass regime is approached, the trend of the one and two-particle states illustrated in Fig. 3.27, suggests that they either merge or cross at our second lightest quark mass, such that the exotic 1^{-+} may be a resonance at our lightest quark mass and at the physical quark masses. We note that the exotic 1^{-+} mass displays the common resonance behavior of becoming bound at quark masses somewhat larger than the physical quark masses. This must happen at sufficiently heavy quark masses by quark counting rules, i.e $2q \rightarrow 4q$ for the 1^{-+} to $a_1\eta'$ transition.

One might have some concerns about $a_1\eta'$ contaminations in the two-point correlation function affecting the extraction of the 1^{-+} meson mass. However we can already make some comments.

Under the assumption that the coupling to the quenched $a_1\eta'$ channel comes with a negative metric, as suggested by chiral perturbation theory arguments, and from the observation that our correlation functions are positive, then it would appear that our in-

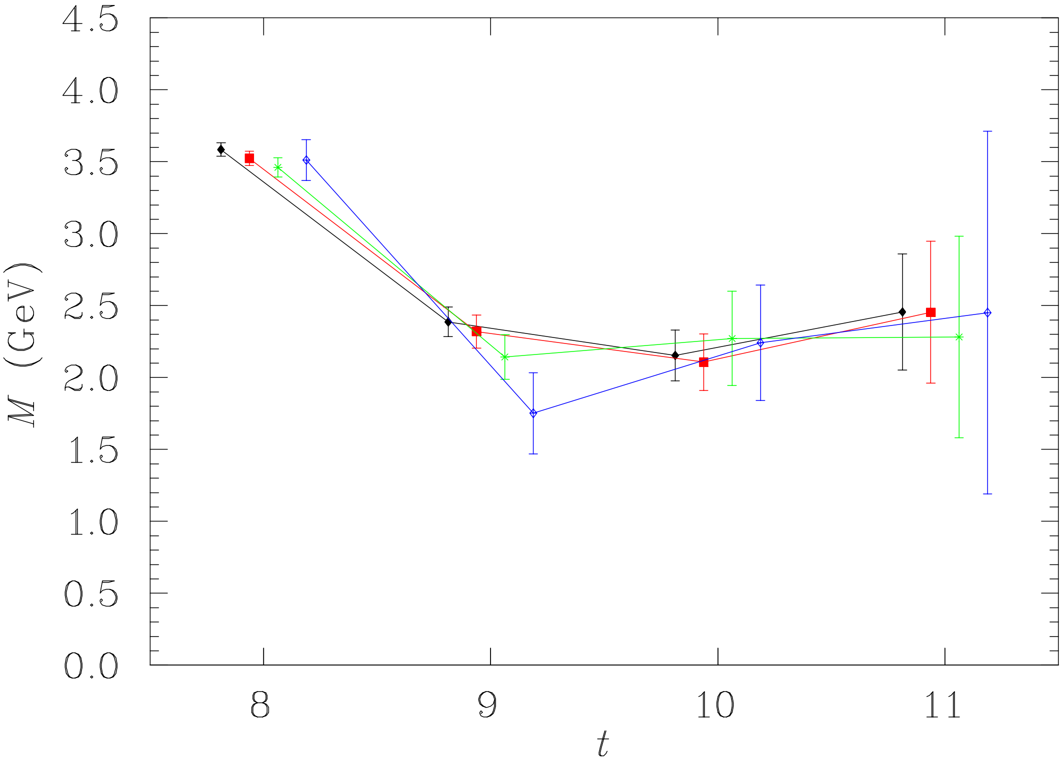

Fig. 3.23: As for Fig. 3.22, but for interpolator χ_3. Signal is lost after $t = 11$.

terpolators couple weakly to the decay channel. Furthermore, at heavy quark masses the correlation function is dominated by the 1^{-+} bound state already at early Euclidean times suggesting that coupling to the decay channel is weak.

Thus we conclude that the hybrid interpolating fields used to explore the 1^{-+} quantum numbers are well-suited to isolating the single-particle 1^{-+} exotic meson.

Moreover, since the mass of the $a_1\eta'$ channel is similar or greater than the single-particle 1^{-+} state, one can conclude that the double-hairpin $a_1\eta'$ contribution to the self energy of the single-particle 1^{-+} exotic meson is repulsive in quenched QCD. Since the curvature observed in Fig. 3.26 reflects attractive interactions, we can also conclude that quenched chiral artifacts are unlikely to be large.

Hence we proceed with simple linear and quadratic extrapolations in quark mass to the physical pion mass, with the caution that chiral nonanalytic behavior could provide corrections to our simple extrapolations the order of 50 MeV in the 1^{-+} mass [45].

Figures 3.27 and 3.28 illustrate the extrapolation of the 1^{-+} exotic and its associated strangeness ±1 1^{-} state to the limit of physical quark mass. We perform the linear fit using the four lightest quark masses and fit the quadratic form to all 8 masses. A third-order single-elimination jackknife error analysis yields masses of $1.74(24)$ and $1.74(25)$ GeV for the linear and quadratic fits, respectively. These results agree within one standard deviation with the experimental $\pi_1(1600)$ result of 1.596^{+25}_{-14} GeV, and exclude the mass of the $\pi_1(1400)$ candidate.

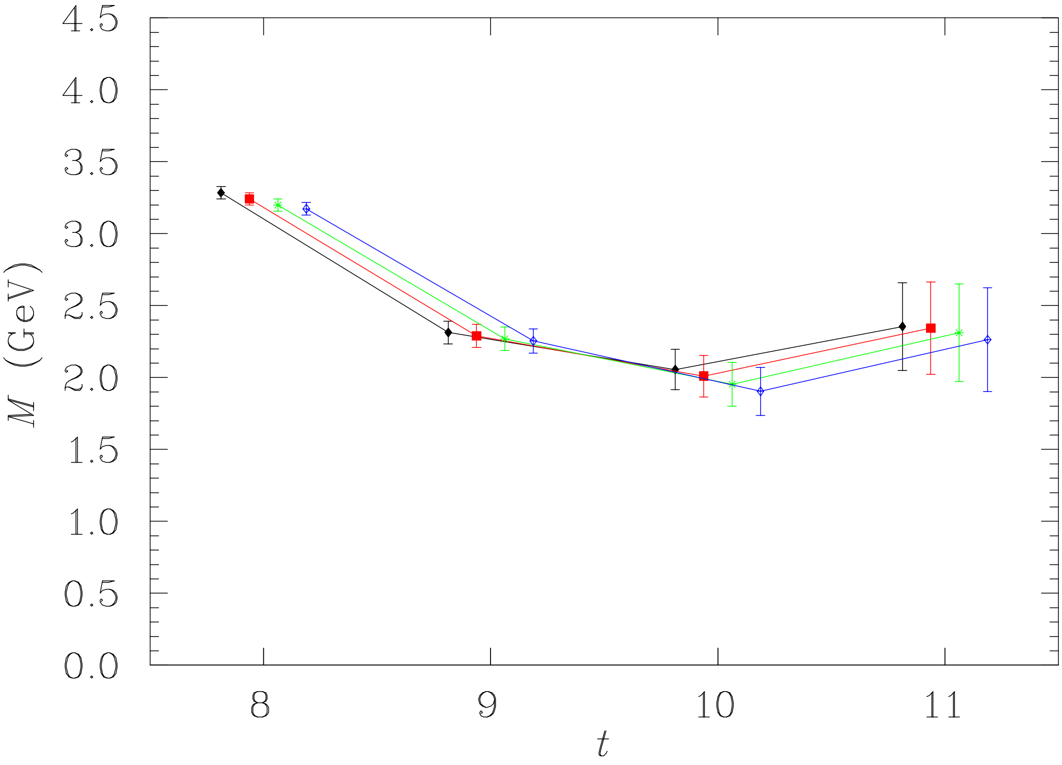

Fig. 3.24: Effective mass for the interpolator χ_2 with a strange quark.

The associated parameters of the fits are as follows. The linear form

$$m_{1^{-+}} \quad = \quad a_0 + a_2\, m_\pi^2\,,$$

yields best fit parameters of

$$\begin{aligned} a_0 &= 1.73 \pm 0.15 \text{ GeV}\,, \\ a_2 &= 0.85 \pm 0.35 \text{ GeV}^{-1}\,. \end{aligned}$$

The quadratic fit, with formula

$$m_{1^{-+}} \quad = \quad a_0 + a_2\, m_\pi^2 + a_4\, m_\pi^4\,,$$

returns parameters

$$\begin{aligned} a_0 &= +1.74 \pm 0.15 \text{ GeV}, \\ a_2 &= +0.91 \pm 0.39 \text{ GeV}^{-1}, \\ a_4 &= -0.46 \pm 0.35 \text{ GeV}^{-3}\,. \end{aligned}$$

3.6.3 Summary

We have found a compelling signal for the $J^{PC} = 1^{-+}$ exotic meson , from which we can extrapolate a physical mass of $1.74(24)$ GeV. Thus for the first time in lattice studies, we find a 1^{-+} mass in agreement with the $\pi_1(1600)$ candidate.

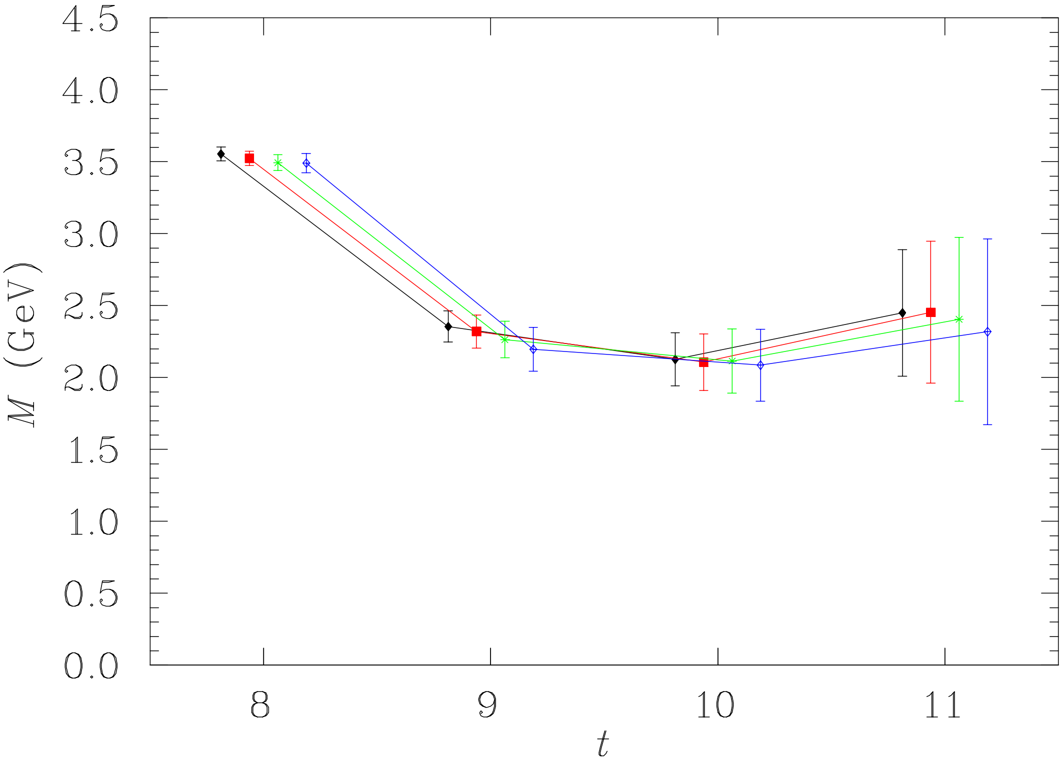

Fig. 3.25: As for Fig. 3.24, but for interpolator χ_3.

The χ_2 interpolating field appears to be extremely useful for avoiding contamination from the $a_1\eta'$ channel, and thus is an excellent choice for this kind of study.

We have also presented the first results for a strangeness ± 1 partner of the exotic 1^{-+} meson lying at $1.92(15)$ GeV.

Looking forward, it will be important to quantify the effects of the quenched approximation. We plan to revisit these calculations at some future point using full dynamical FLIC fermions [27, 28]. Of particular interest will be the extent to which the curvature observed in approaching the chiral regime is preserved in full QCD.

At some point, a detailed finite volume analysis should be performed in order to further explore the role of the two-body decay channel.

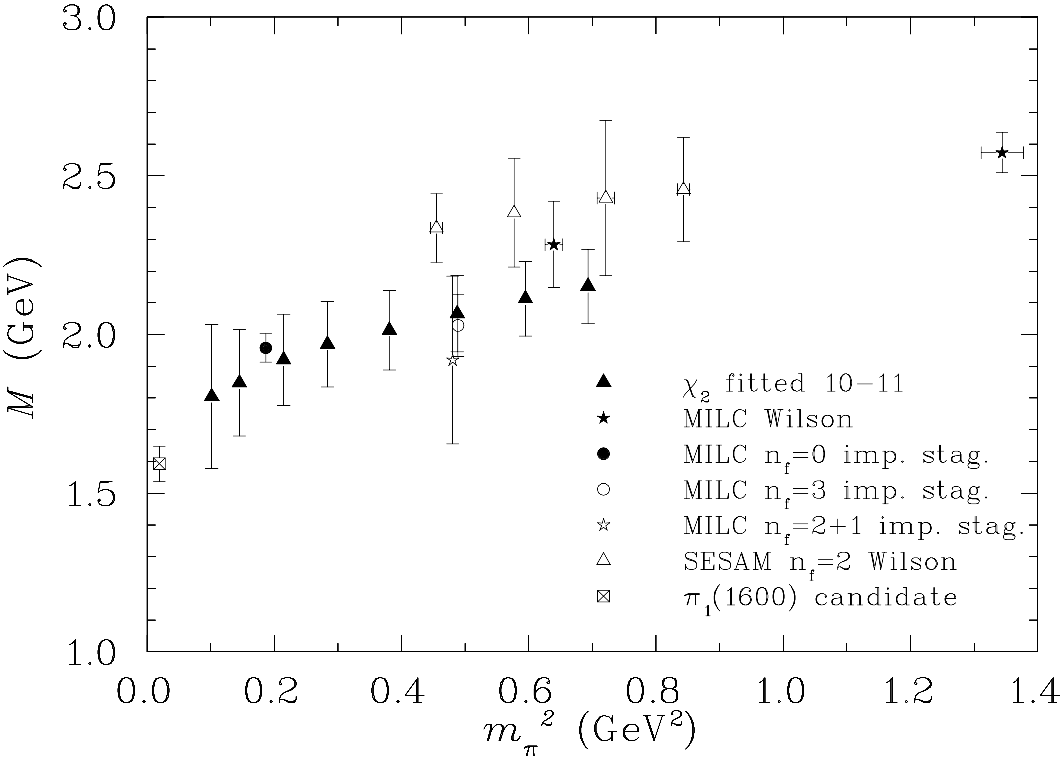

Fig. 3.26: A survey of results in this field. The MILC results are taken from [10] and show their Q^4, $1^{-+} \rightarrow 1^{-+}$ results, fitted from $t = 3$ to $t = 11$. Open and closed symbols denote dynamical and quenched simulations respectively.

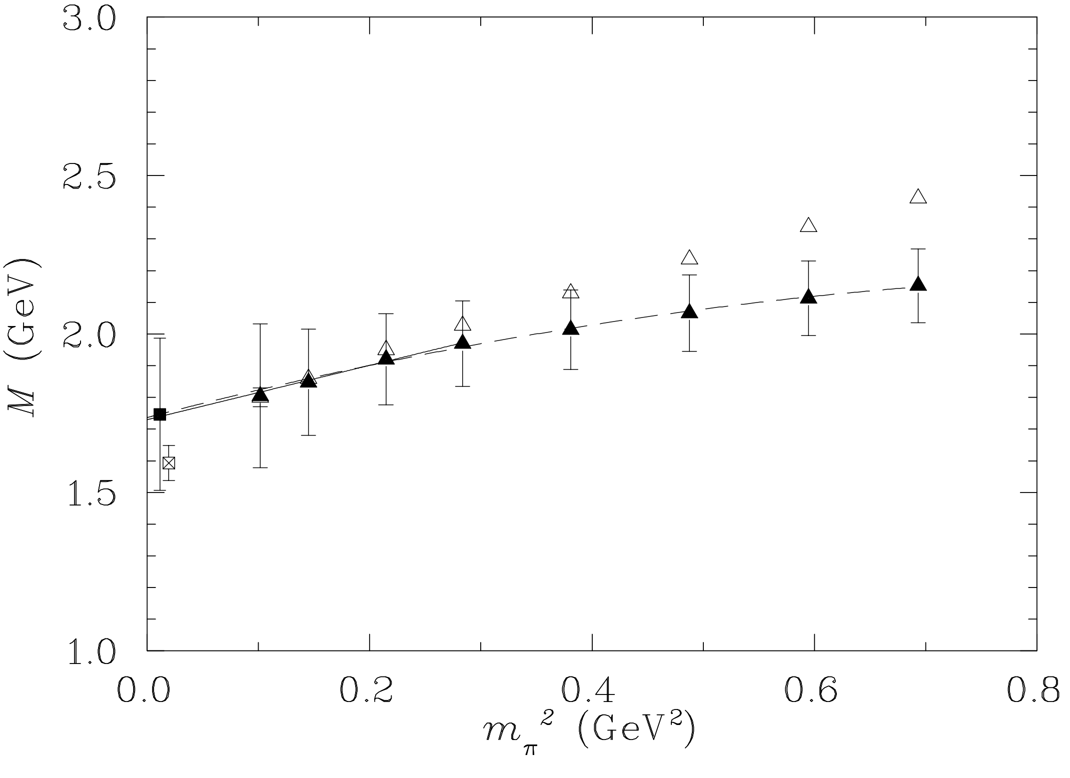

Fig. 3.27: The 1^{-+} exotic meson mass obtained from fits of the effective mass of the hybrid interpolator χ_2 from $t = 10 \rightarrow 12$ (full triangles) are compared with the $a_1\eta'$ two-particle state (open triangles). The extrapolation curves include a quadratic fit to all eight quark masses (dashed line) and a linear fit through the four lightest quark masses (solid line). The full square is result of linear extrapolation to the physical pion mass, while the open square (offset for clarity) indicates the $\pi_1(1600)$ experimental candidate.

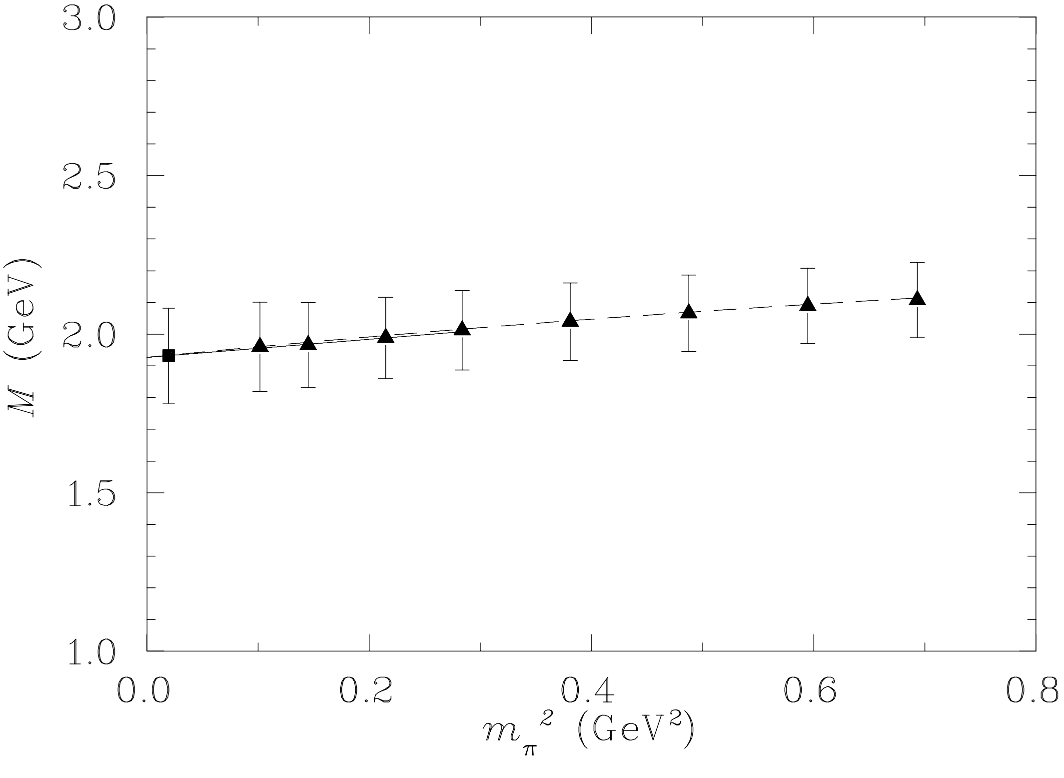

Fig. 3.28: Extrapolation of the associated strangeness ±1 $J^P = 1^-$ state obtained from χ_2. Symbols are as in Fig. 3.27.

4

Source dependence of Hybrid and Exotic signal

4.1 Introduction

In our simulations of conventional mesons we have several parameters which can be adjusted to optimise the overlap of the interpolators with particular mass eigenstates. These include

- $\alpha_{\mathrm{src}}, \alpha_{\mathrm{sink}}$: The smearing parameters for Gauge-invariant Gaussian smearing at Source and Sink
- $n_{\mathrm{src}}, n_{\mathrm{sink}}$: The number of sweeps of Gauge-invariant Gaussian Smearing at Source and Sink

.

By Gauge-invariant Gaussian smearing, we refer to the following procedure [24]: We start with a point source, $\psi_0(\vec{x}_0, t_0)$, at space-time location $(\vec{x}_0, t_0)$ and proceed via the iterative scheme,

$$\psi_i(x,t) = \sum_{x'} F(x,x')\, \psi_{i-1}(x',t)\,, \tag{4.1}$$

where

$$\begin{aligned} F(x,x') \;&=\; (1-\alpha)\delta_{x,x'} + \frac{\alpha}{6}\sum_{\mu=1}^{3}\big[U_\mu(x)\,\delta_{x',x+\widehat{\mu}} \\ &\qquad + U_\mu^\dagger(x-\widehat{\mu})\,\delta_{x',x-\widehat{\mu}}\big]\,. \end{aligned} \tag{4.2}$$

Repeating the procedure N times gives the resulting fermion field

$$\psi_N(x,t) = \sum_{x'} F^N(x,x')\, \psi_0(x',t)\,. \tag{4.3}$$

It has been shown that for reasonable values of N and α it is the product $N\alpha$ that is the significant parameter [14], so we shall hold α fixed at 0.7.

The inclusion of gauge functionals in our interpolators expands the parameter space with another three degrees of freedom:

- α_G: The gauge-field APE-smearing parameter
- n_G: The number of sweeps of APE-smearing performed on the links used in the gauge-functional
- Q_{paths}: The number of link paths used to construct the gauge-functionals.

The APE-smearing procedure [1,22] replaces a link, $U_\mu(x)$, with a sum of $(1-\alpha_G)$ times the link and α_G times its staples

$$\begin{aligned}
&U_\mu(x) \to U'_\mu(x) = (1-\alpha_G)U_\mu(x) \\
&+\frac{\alpha_G}{6}\sum_{\substack{\nu=1\\ \nu\neq\mu}}^{4}\Big[U_\nu(x)U_\mu(x+\nu a)U_\nu^\dagger(x+\mu a) \\
&+U_\nu^\dagger(x-\nu a)U_\mu(x-\nu a)U_\nu(x-\nu a+\mu a)\Big]\,,
\end{aligned} \tag{4.4}$$

followed by projection back to SU(3). We select the unitary matrix U_μ^{FL} which maximises

$$\mathcal{R}e\,\mathrm{tr}(U_\mu^{\mathrm{FL}}\,U_\mu'^{\dagger})$$

by iterating over the three diagonal SU(2) subgroups of SU(3). This procedure of smearing followed immediately by projection is repeated n_G times.

In order to obtain the chromo-electric and chromo-magnetic fields with which we build the hybrid operators, we make use of a modified version of APE smearing, in which the smeared links do not involve averages which include links in the temporal direction. In this way we preserve the notion of a Euclidean ‘time’ and avoid overlap of the creation and annihilation operators.

Each iteration of our modified APE-smearing algorithm proceeds as

$$\begin{aligned}
U_i(x) &\to (1-\alpha)\,U_i(x) \\
&+\ \frac{\alpha}{4}\sum_{j=1}^{3}(1-\delta_{ij})\,U_j(x)\,U_i(x+\hat{j})\,U_j^\dagger(x+\hat{\imath}) \\
&+\ \frac{\alpha}{4}\sum_{j=1}^{3}(1-\delta_{ij})\,U_j^\dagger(x-\hat{j})\,U_i(x-\hat{j})\,U_j(x-\hat{j}+\hat{\imath})\,, \\
U_4(x) &\to (1-\alpha)\,U_4(x) \\
&+\ \frac{\alpha}{6}\sum_{j=1}^{3}U_j(x)\,U_4(x+\hat{j})\,U_j^\dagger(x+\hat{4}) \\
&+\ \frac{\alpha}{6}\sum_{j=1}^{3}U_j^\dagger(x-\hat{j})\,U_4(x-\hat{j})\,U_j(x-\hat{j}+\hat{4})\,.
\end{aligned}$$

As above, it is the product $n_G\alpha_G$ which is of physical significance [14], so we shall hold α_G fixed at 0.7 and simply vary n_G.

In summary, we are left with three independent parameters to explore: n_{src}, n_G, and Q_{paths}. Here we perform a systematic exploration of this rather large parameter space in order to determine the optimal prescription for both a hybrid with $\bar{q}q$ quantum numbers and also for our χ_2 exotic meson interpolator.

4.2 Method

We calculate two-point correlation functions for our χ_2 ($i\epsilon_{jkl}\bar{q}^a\gamma_k B_l^{ab}q^b$) exotic interpolating field and also for the χ_3 ($i\bar{q}^a\gamma_j B_j^{ab}q^b$) and χ_4 ($i\bar{q}^a\gamma_4\gamma_j B_j^{ab}q^b$) hybrid pion interpolating fields. We use a lattice of dimensions $16^3 \times 32$ at $\beta = 1.100$ using a doubly-blocked Wilson-2 (DBW2) action, with a lattice spacing of 0.1273 fm.

On this lattice we are able to vary not only the n_G and $Q_{\rm paths}$, but also $n_{\rm src}$. In particular we choose $n_{\rm src} = \{0, 16, 48, 144\}$, $n_G = \{4, 6, 10, 20\}$, and a 1- or 3-loop construction of $F_{\mu\nu}$ [11]. Seven values for the hopping parameter κ are used, corresponding to pion masses between $300 - 800$ MeV.

We have also performed a similar calculation on the larger $20^3 \times 40$ lattice used in the previous section. These results can be found in appendix C.

4.3 Results

4.3.1 Hybrid Pion

We consider the two hybrid $J^{PC} = 0^{-+}$ interpolators of Table 3.1, and refer to them as χ_3 and χ_4. Comparing Figures (4.3) through (4.6), it is immediately apparent that the strongest signal is obtained for $n_{\rm src} = 0$, *i.e* for a point source. This is in strong contrast to the picture observed for a conventional pion interpolator, as in the following figure:

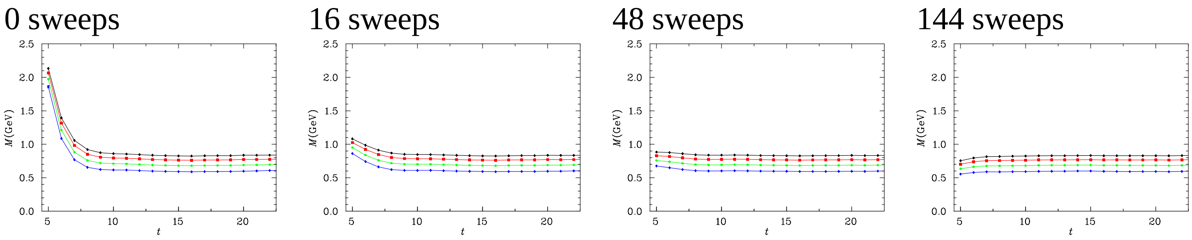
0 sweeps 16 sweeps 48 sweeps 144 sweeps

Fig. 4.1: Fermion-source smearing-dependence of conventional pion signal

This sensitive dependence on $n_{\rm src}$ is also observed for χ_4, suggesting that the ground state of these Fock-space components is one where the quarks are quite close together.

Considering the left-hand columns of Figures (4.3) and (4.7), we see that the hybrid pion interpolators exhibit increasing jitter with an increasing amount of APE-smearing of the gauge fields used to construct $F_{\mu\nu}$. Figure 4.2 summarizes the pattern for χ_4.

A more quantitative approach is taken in Table 4.1 which shows how varying the parameters affects our ability to extract a ground-state mass. The window $t = [8, 13]$ is chosen as it gives an acceptable χ^2 value for the $n_G = 4$ case. The heaviest input quark mass is chosen so as to give the strongest signal, and thus easiest comparison. In summary, the hybrid pion interpolators are best calculated with $n_{\rm src} = 0$, $n_G < 6$, and $Q_{\rm paths} = 1$. To put it plainly, the quarks are close together, and the source is fairly localised.

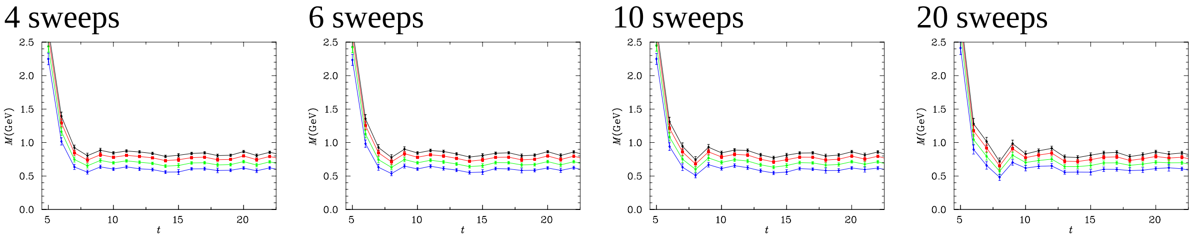

Fig. 4.2: Gauge-field smearing-dependence of χ_4 hybrid pion signal. Here $n_{\rm src} = 0$, i.e a point source is used for the quark fields.

Table 4.1: Effect of gauge-field smearing on χ_4 hybrid pion mass determination, $t = [8, 13]$

		$Q_{\rm paths} = 1$			$Q_{\rm paths} = 3$		
$n_{\rm src}$	n_G	Ma	σ	$\chi^2/$d.o.f	Ma	σ	$\chi^2/$d.o.f
0	4	0.5505	0.0061	1.034	0.5506	0.0061	0.811
	6	0.5511	0.0063	1.711	0.5513	0.0063	1.598
	10	0.5524	0.0069	2.573	0.5526	0.0067	2.376
	20	0.5498	0.0090	4.464	0.5501	0.0089	4.370
16	4	0.5523	0.0221	0.598	0.5548	0.0237	0.523
	6	0.5513	0.0198	0.605	0.5503	0.0203	0.480
	10	0.5555	0.0198	0.971	0.5563	0.0200	0.925
	20	0.5488	0.0235	1.254	0.5471	0.0237	1.064
48	4	0.5248	0.0841	0.258	0.5427	0.0988	0.199
	6	0.5183	0.0660	0.422	0.5242	0.0682	0.365
	10	0.5337	0.0489	0.873	0.5358	0.0502	0.750
	20	0.5473	0.0537	1.724	0.5472	0.0539	1.703
144	4	0.4989	0.1395	0.345	0.5540	0.1878	0.179
	6	0.5108	0.1003	0.627	0.5269	0.1105	0.469
	10	0.4891	0.0900	0.977	0.4988	0.0808	0.928
	20	0.4783	0.1287	1.103	0.4888	0.1148	1.051

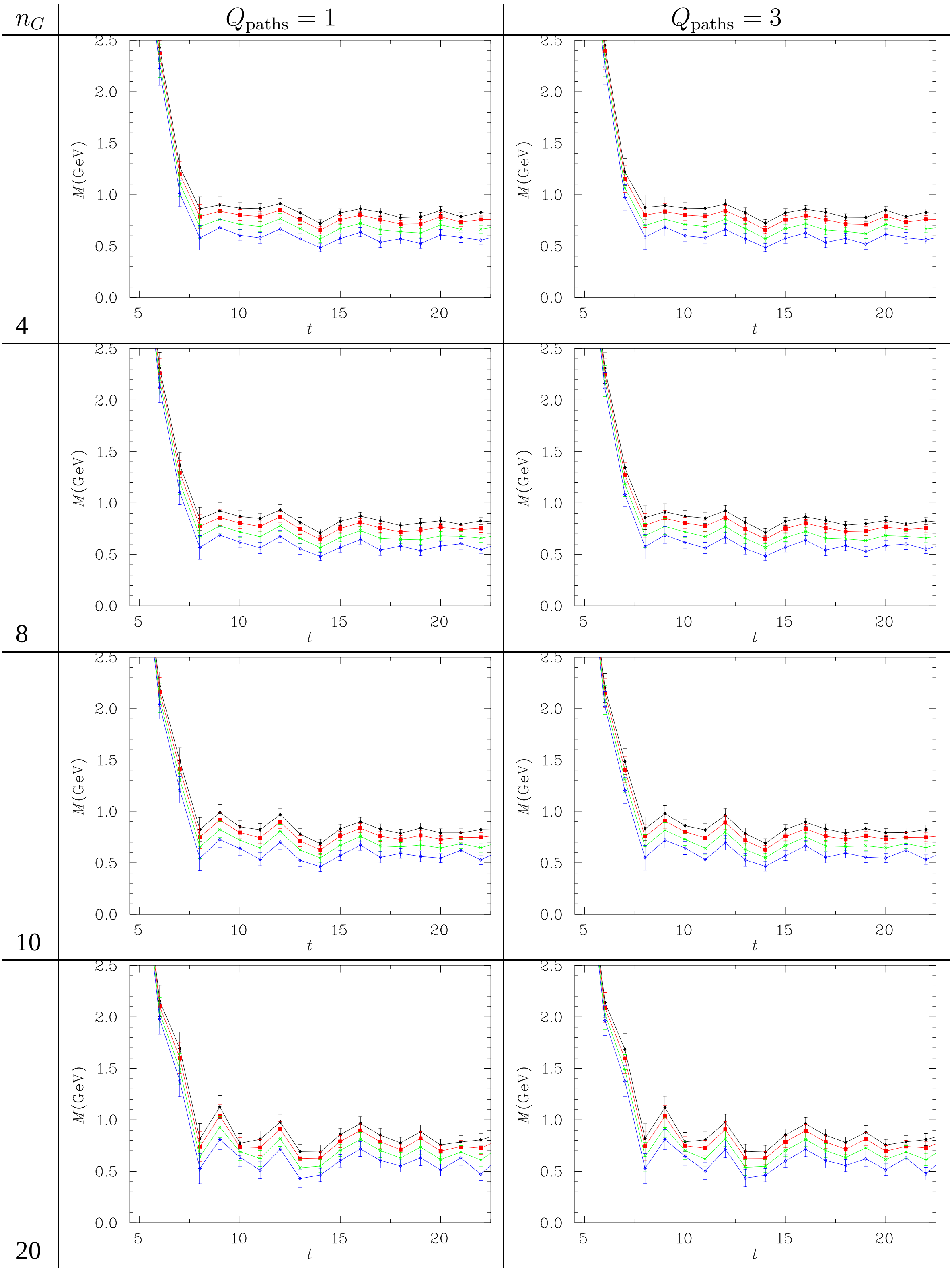

Fig. 4.3: Hybrid π- meson (χ_3) effective masses from the $16^3 \times 32$ lattice with $n_{\text{src}} = 0$. Results for the heaviest four quark masses are depicted.

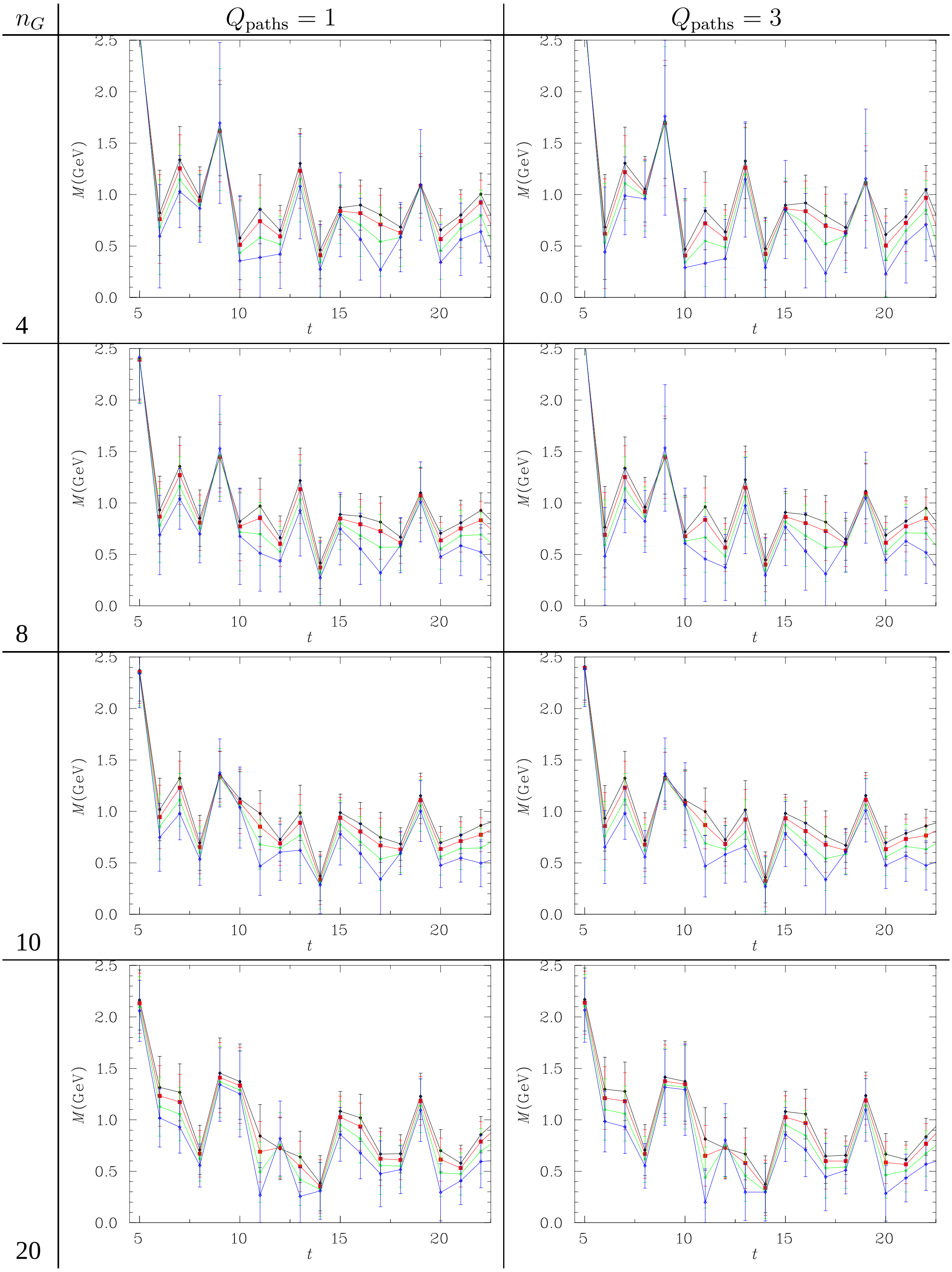

Fig. 4.4: Hybrid π- meson (χ_3) effective masses from the $16^3 \times 32$ lattice with $n_{\text{src}} = 16$. Results for the heaviest four quark masses are depicted.

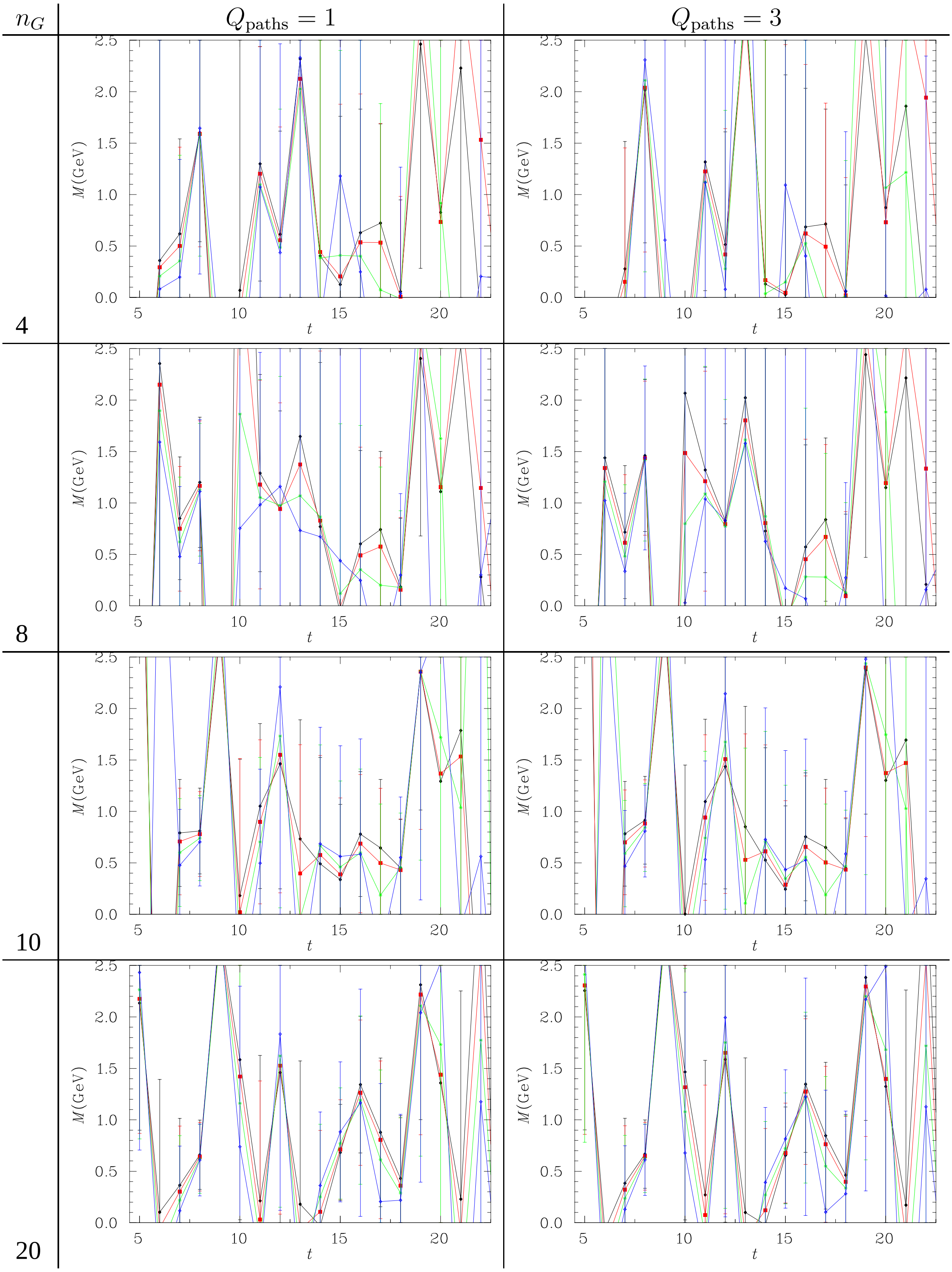

Fig. 4.5: Hybrid π- meson (χ_3) effective masses from the $16^3 \times 32$ lattice with $n_{\mathrm{src}} = 48$. Results for the heaviest four quark masses are depicted.

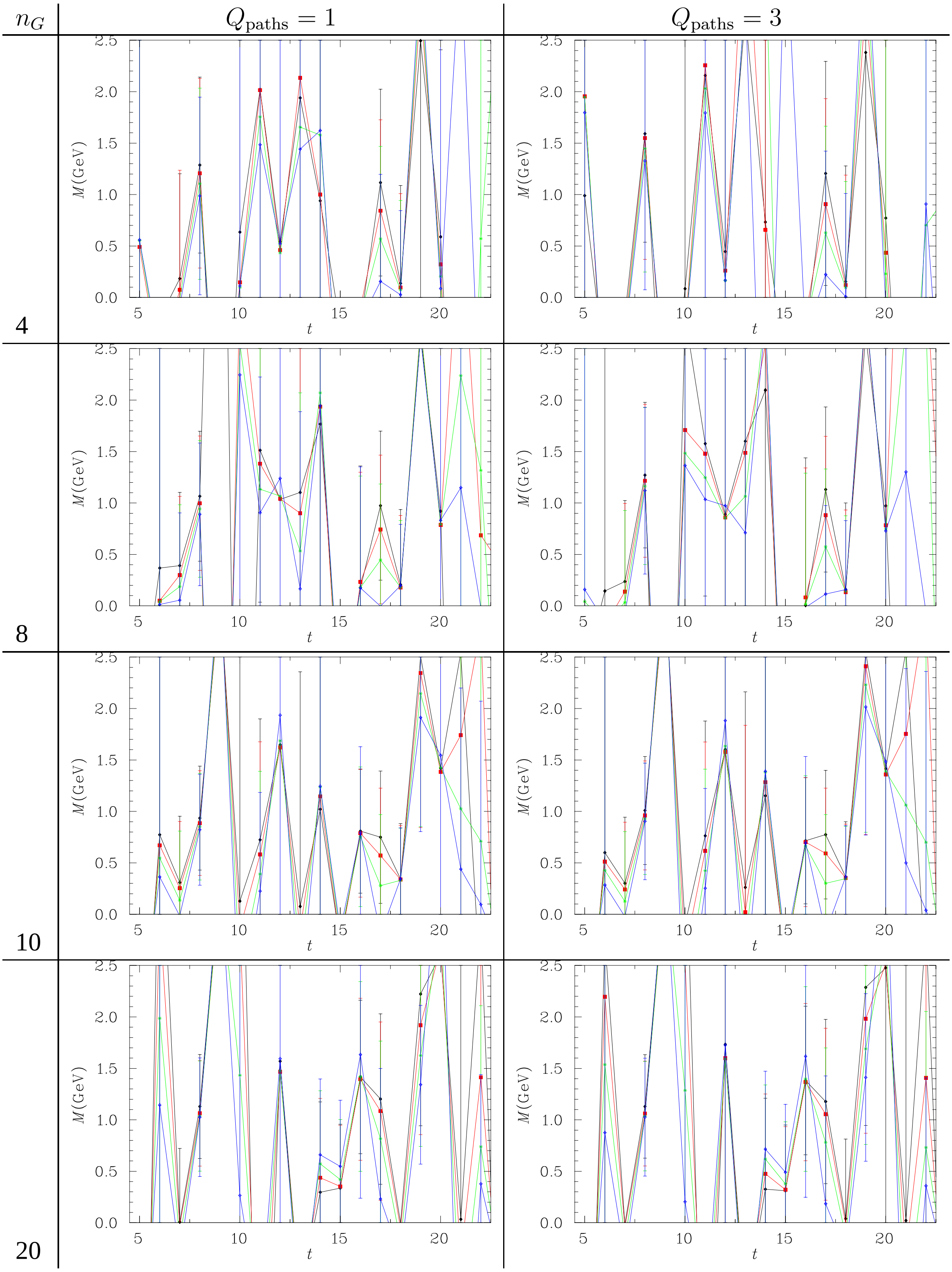

Fig. 4.6: Hybrid π- meson (χ_3) effective masses from the $16^3 \times 32$ lattice with $n_{\text{src}} = 144$. Results for the heaviest four quark masses are depicted.

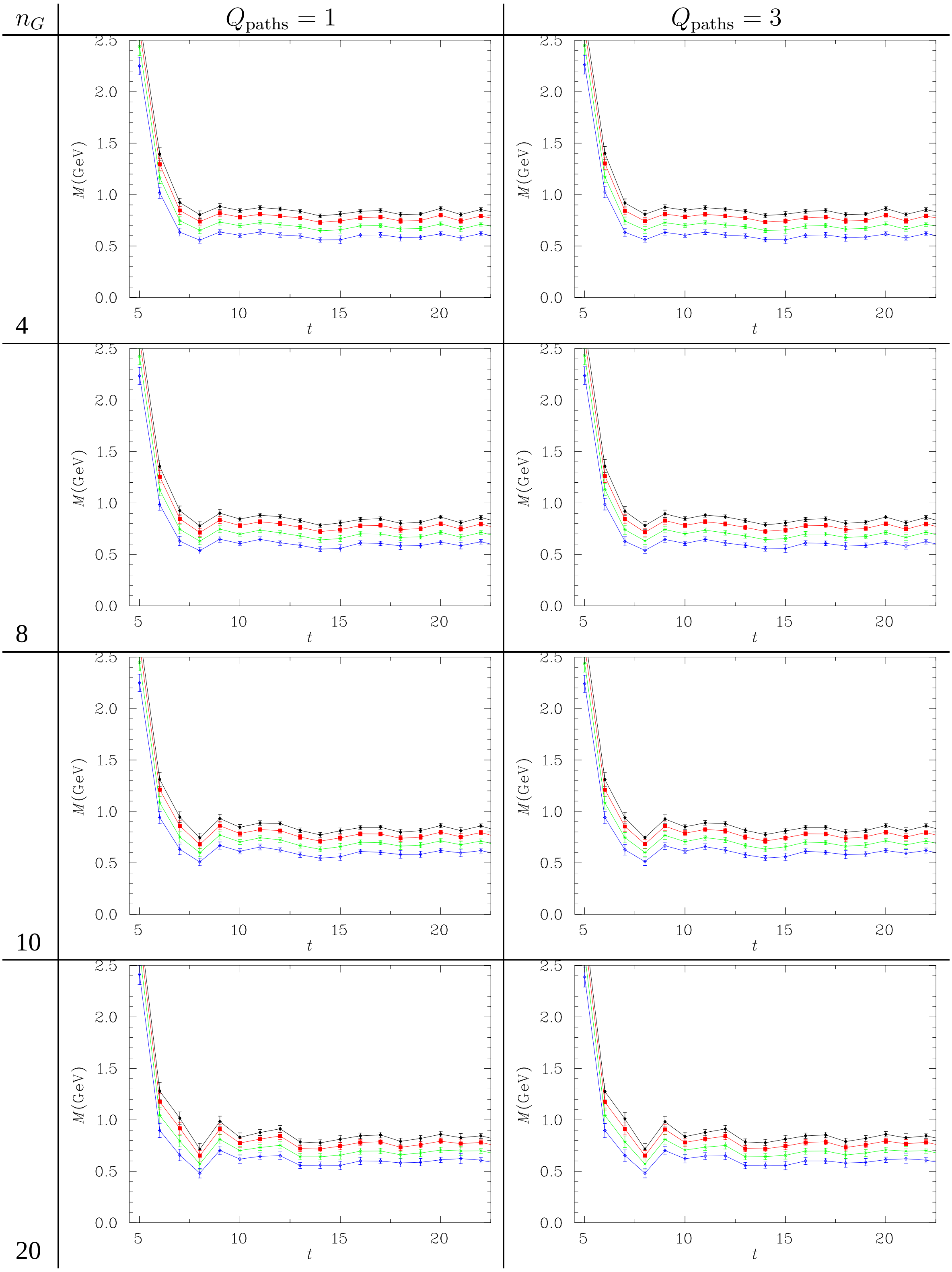

Fig. 4.7: Hybrid π- meson (χ_4) effective masses from the $16^3 \times 32$ lattice with $n_{\text{src}} = 0$. Results for the heaviest four quark masses are depicted.

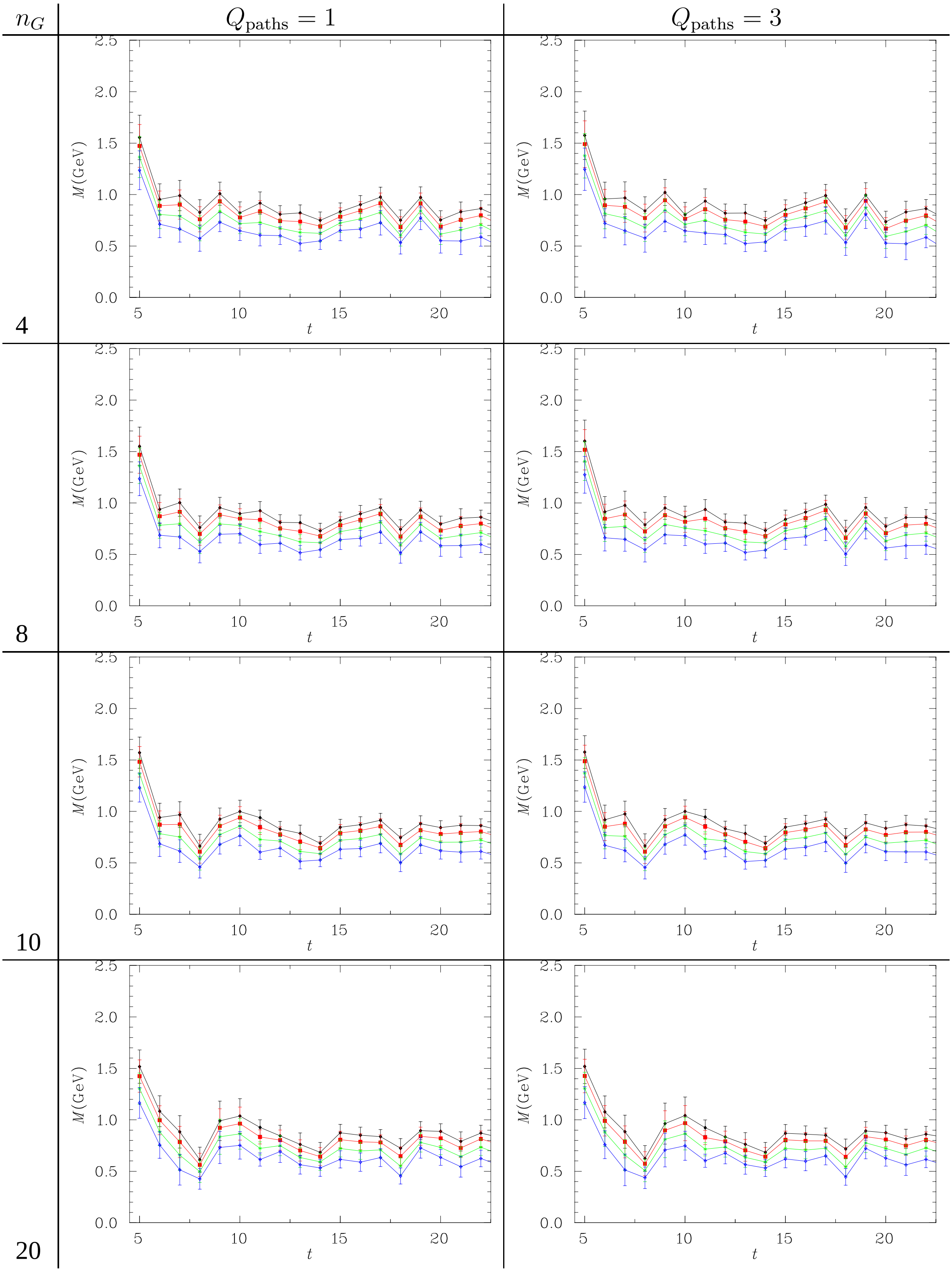

Fig. 4.8: Hybrid π- meson (χ_4) effective masses from the $16^3 \times 32$ lattice with $n_{\text{src}} = 16$. Results for the heaviest four quark masses are depicted.

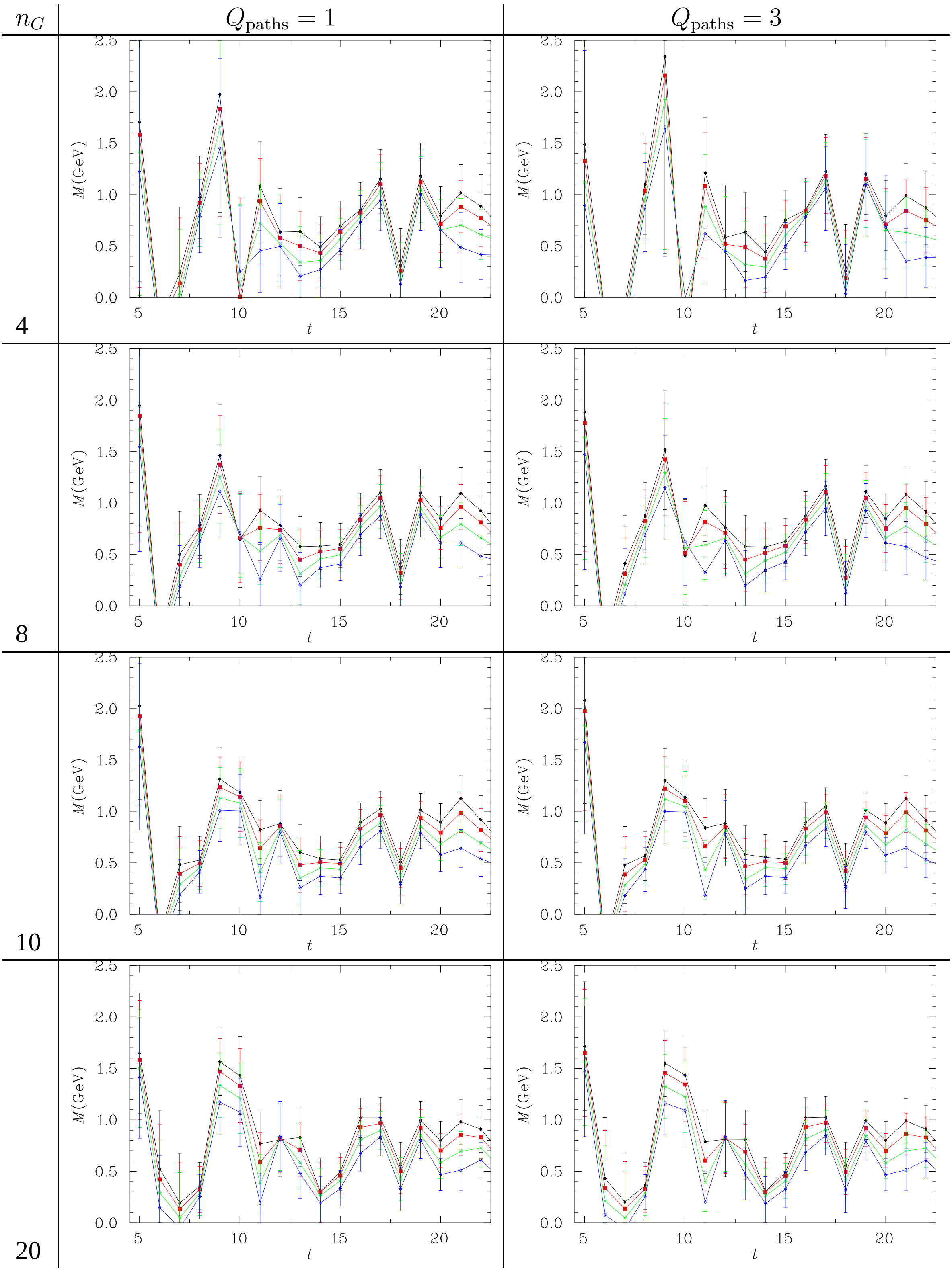

Fig. 4.9: Hybrid π- meson (χ_4) effective masses from the $16^3 \times 32$ lattice with $n_{\text{src}} = 48$. Results for the heaviest four quark masses are depicted.

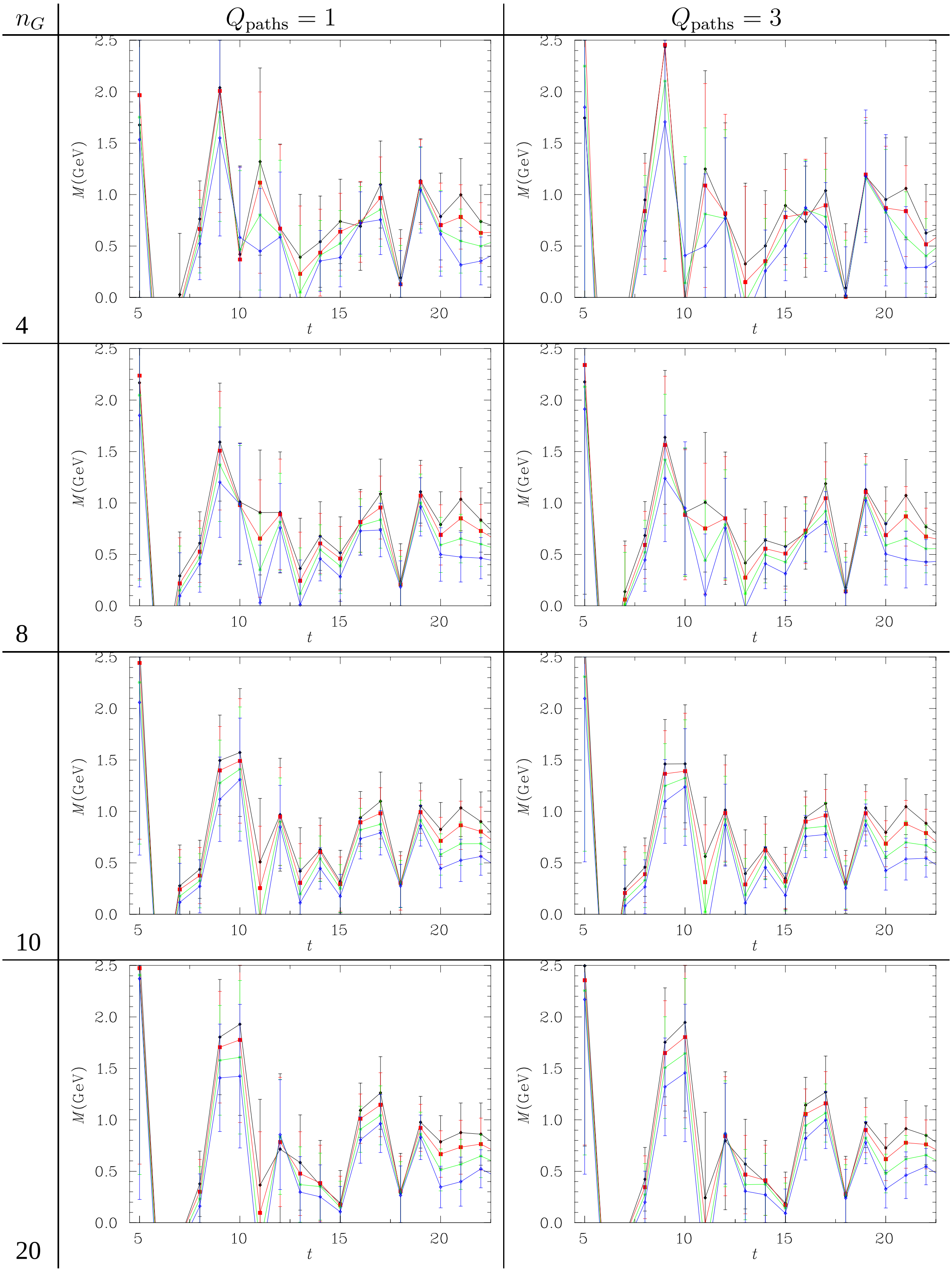

Fig. 4.10: Hybrid π- meson (χ_4) effective masses from the $16^3 \times 32$ lattice with $n_{\text{src}} = 144$. Results for the heaviest four quark masses are depicted.

4.3.2 Exotic

For the exotic interpolator, the situation is different. Greatest control of statistical error occurs where $n_{\text{src}} = 0$, but in contrast to the hybrid pion case, the signal is maximised for $n_G = 20$. In addition, whilst setting $n_{\text{src}} = 16$ effects a large increase in error bars, the central values in this case exhibit a plateau from $t = 5$, i.e immediately after the source. The net result is, however, an increase in uncertainty of the fit. Increasing n_{src} beyond 16 results in the effective mass ceasing to be positive definite close the source indicating that we are possibly accessing the two-particle $a_1\eta'$ decay channel instead of the desired exotic state. $Q_{\text{paths}} = 1$ gives approximately 10% smaller errors than $Q_{\text{paths}} = 3$ for a fit between $t = 6$ and $t = 8$ at $n_{\text{src}} = 0$ and $n_G = 20$.

Table 4.2: Effect of gauge-field smearing on 1^{-+} Exotic meson mass determination, $t = [5, 7]$

		$Q_{\text{paths}} = 1$			$Q_{\text{paths}} = 3$		
n_{src}	n_G	Ma	σ	$\chi^2/\text{d.o.f}$	Ma	σ	$\chi^2/\text{d.o.f}$
0	4	2.5986	0.0827	10.758	2.6471	0.0900	9.489
	6	2.4935	0.0783	16.246	2.5249	0.0824	15.255
	10	2.3777	0.0741	22.181	2.3913	0.0756	21.838
	20	2.2859	0.0813	20.403	2.2860	0.0810	20.394
16	4	1.7909	0.2414	0.552	1.8277	0.2708	0.347
	6	1.7806	0.2179	0.621	1.8615	0.2681	0.407
	10	1.7874	0.1976	0.360	1.8058	0.2136	0.413
	20	1.7208	0.1796	0.058	1.7492	0.1937	0.092

Table 4.3: Effect of gauge-field smearing on 1^{-+} Exotic meson mass determination, $t = [6, 8]$

		$Q_{\text{paths}} = 1$			$Q_{\text{paths}} = 3$		
n_{src}	n_G	Ma	σ	$\chi^2/\text{d.o.f}$	Ma	σ	$\chi^2/\text{d.o.f}$
16	4	2.1086	0.1156	0.708	2.1458	0.1285	0.523
	6	2.0101	0.0965	0.971	2.0298	0.1025	0.892
	10	1.9145	0.0858	0.675	1.9321	0.0875	0.741
	20	1.8422	0.0878	0.461	1.8441	0.0878	0.445

In summary, the ideal prescription for the exotic interpolating field is $n_{\text{src}} \in (0, 16)$, $n_G \simeq 20$, $Q_{\text{paths}} = 1$. As in the hybrid pion case the quarks remain close together, but this time they are surrounded by a large cloud of gluons.

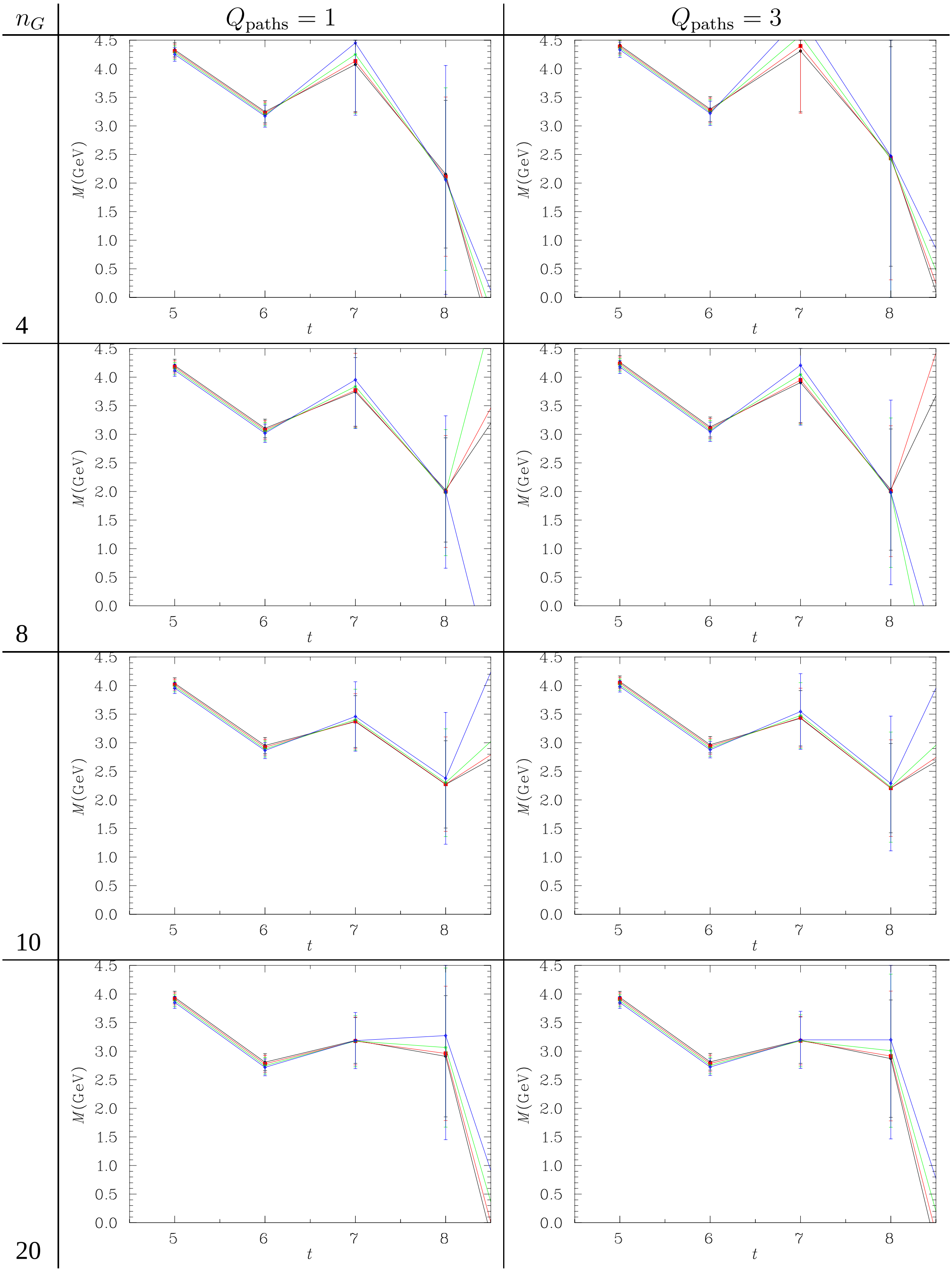

Fig. 4.11: Exotic meson effective masses from the $16^3 \times 32$ lattice with $n_{\text{src}} = 0$. Results for the heaviest four quark masses are depicted.

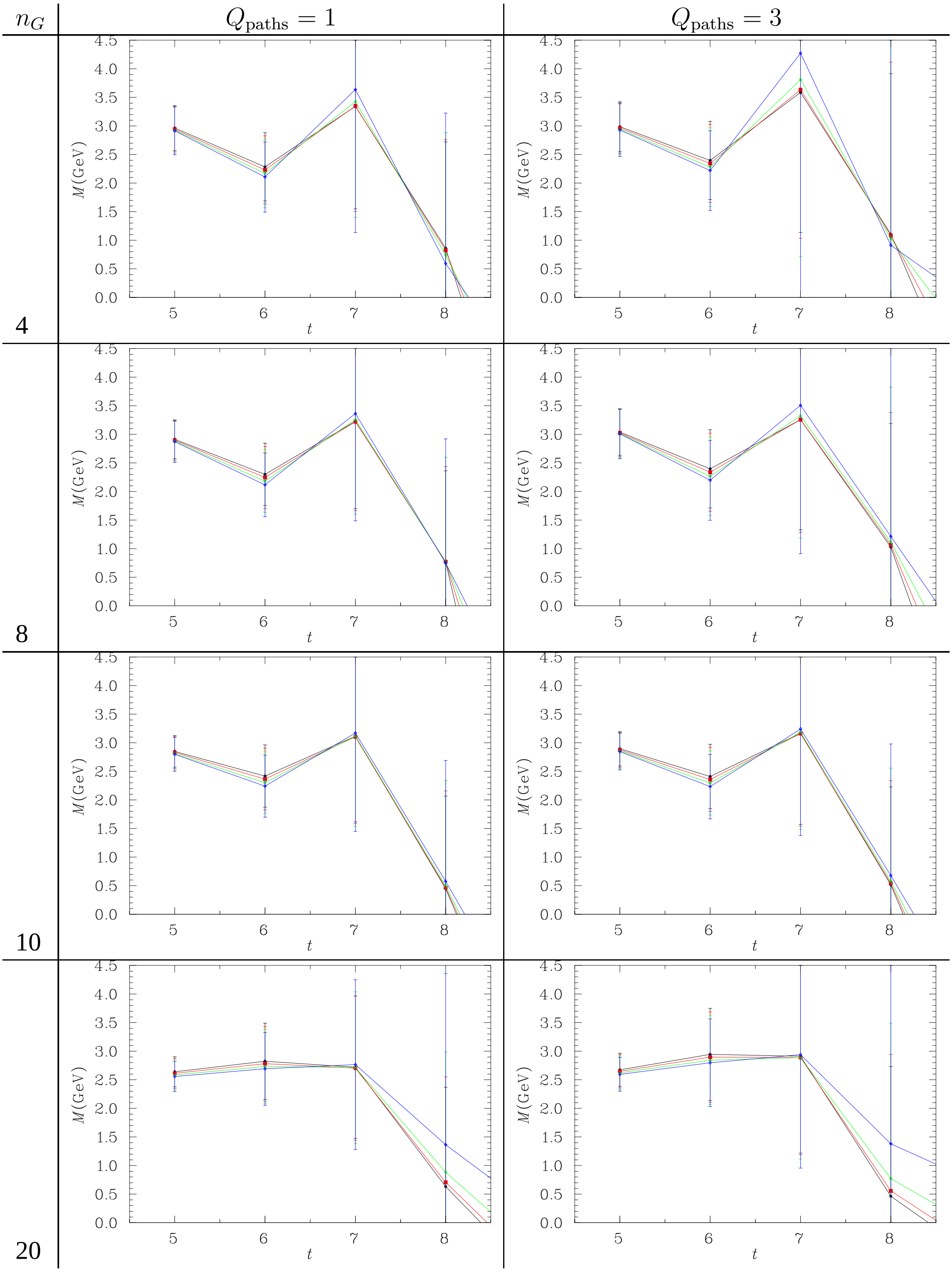

Fig. 4.12: Exotic meson effective masses from the $16^3 \times 32$ lattice with $n_{\text{src}} = 16$. Results for the heaviest four quark masses are depicted.

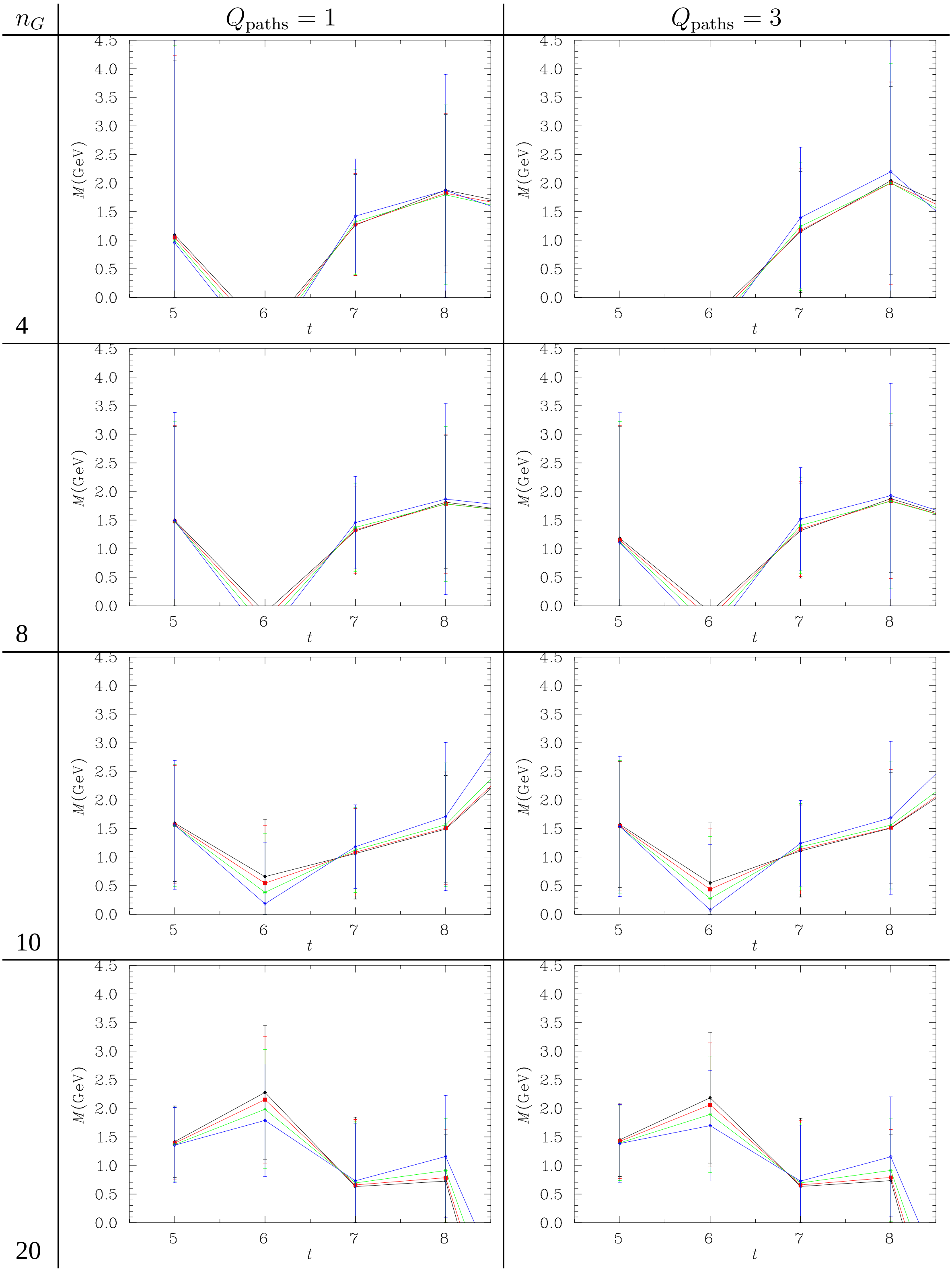

Fig. 4.13: Exotic meson effective masses from the $16^3 \times 32$ lattice with $n_{\text{src}} = 48$. Results for the heaviest four quark masses are depicted.

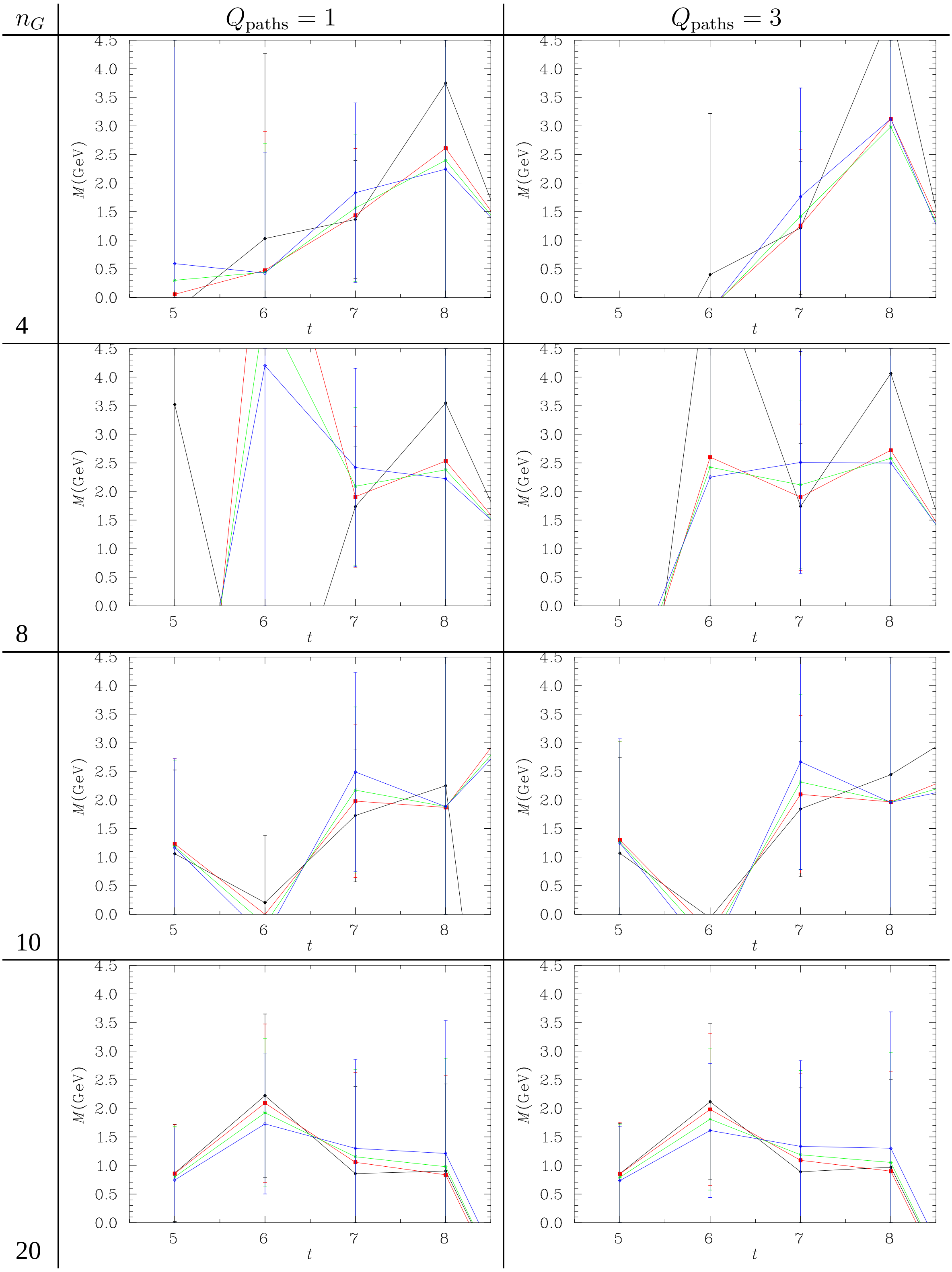

Fig. 4.14: Exotic meson effective masses from the $16^3 \times 32$ lattice with $n_{\text{src}} = 144$. Results for the heaviest four quark masses are depicted.

4.4 Discussion and Summary

Our hybrid and exotic interpolators show a signficant dependence on the spatial extent of the operators from which they are constructed. For the exotic meson in particular, good signal requires

- Considerable smearing of the gauge-fields in $F_{\mu\nu}$ ($n_G \simeq 10 - 20$)
- Very little smearing of the fermion source ($n_{\rm src} < 16$)

.

Taken together, these suggest a picture of hybrid mesons which have a quark-antiquark pair very close together with a gluon cloud surrounding them for some distance. This is different from the usual picture of a quark-antiquark pair joined by a flux tube.

For APE-smearing, N smearing sweeps with smearing fraction α applied to the gauge-fields corresponds to notionally replacing point sources with distributed objects of characteristic size $\frac{a}{\sqrt{3}}\sqrt{N\alpha}$ [14]. Thus, 10 sweeps of APE-smearing with $\alpha = 0.7$ corresponds on our lattice, which has lattice spacing of $a = 0.128\,\mathrm{fm}$, to an average spatial extent for the hybrid's gluon structure of approximately 0.2 fm, vs approximately 0.3 for the 1^{-+}. Neither the hybrid pion nor the 1^{-+} benefited from a highly-improved version of $F_{\mu\nu}$, so future calculations may use the far simpler single-loop variant.

In order to gain a deeper appreciation of this behaviour it would be instructive to perform calculations with greater statistics, examing at a higher resolution the region of $n_{\rm src} = [0, 16]$. A calculation of the electromagnetic form-factors of these hybrid particles would also be of assistance.

5

Meson form factors

5.1 Introduction

Masses are the simplest meson observables we can extract from the lattice, but we can in principle obtain many observables. Of particular interest are the form-factors, as these encode information about the charge radii, magnetic and quadrupole moments, *i.e.* they tell us about the shape of the hadrons, and give us valuable insight into the behaviour of the quarks inside.

In 1980, Arnold *e*t al. published a paper showing the general form for C- and T-invariant form-factors for a spin-1 object [7]. Calculations from QCD sum-rules followed, a notable papers being that of Ioffe and Smilga [26]. A light-cone calculation was later performed by Brodsky and Hiller [15].

Here we present the first lattice calculation of the ρ-meson quadrupole form-factor. Charge and magnetic form-factors are also calculated. From these we can extract the relevant static quantities of mean square charge-radius and magnetic moment.

We also analyse the dependence of light-quark contributions to these form-factors on their environment and contrast these with a new calculation of the corresponding pseudoscalar-sector result.

We begin by introducing some formalism, and proceed to outline the process for extracting these quantities for the π-meson and then the general case for a spin-1 meson.

5.2 Three-point function with current insertion

Consider the following three-point function:

$$G_{\mu\,\nu}^{\,\alpha}(t_2, t_1, \vec{p}\,', \vec{p}) = \sum_{\vec{x_2}, \vec{x_1}} e^{-i\vec{p'}.(\vec{x_2}-\vec{x_1})} e^{-i\vec{p}.\vec{x_1}} \langle\Omega|\chi_\mu(x_2) J^\alpha(x_1) \chi_\nu^\dagger(0)|\Omega\rangle\,. \qquad (5.1)$$

The quark-flow diagrams relevant to this calculation are shown in figure 5.2 for the case of a K^+. The relevant quark-level calculation is performed in appendix D. For our purposes, it is sufficient to observe that we may make use of the charge symmetry properties of the quarks to rewrite the second of these diagrams as the charge-conjugate of the s-quark contribution to a K^- meson and we may thus concern ourselves only with the case of the current striking a forward-going quark.

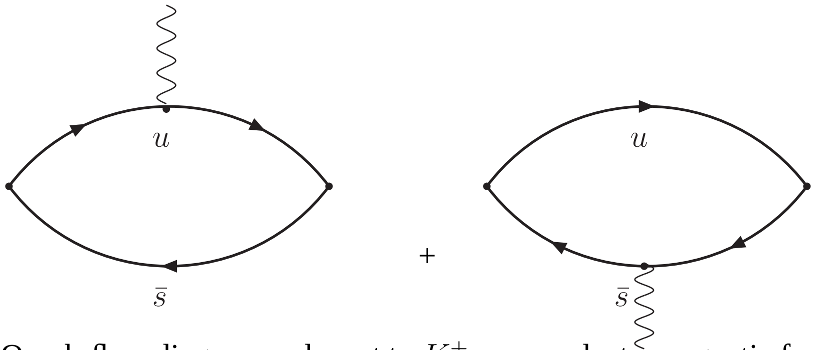

Fig. 5.1: Quark-flow diagrams relevant to K^+ meson electromagnetic form-factors.

Inserting two sets of complete states, we can rewrite Eq. (5.1) as

$$\begin{aligned}
& G^{\,\alpha}_{\mu\,\nu}(t_2, t_1, \vec{p'}, \vec{p}) \\
= \; & \sum_{\vec{x_2},\vec{x_1}} \sum_{p_i,p_f} \sum_{s,s'} e^{-i\vec{p'}.(\vec{x_2}-\vec{x_1})} e^{-i\vec{p}.\vec{x_1}} \langle\Omega|\chi_\mu(x_2)|p_f, s'\rangle\langle p_f, s'|J^\alpha(x_1)|p_i, s\rangle\langle p_i, s|\chi^\dagger_\nu(0)|\Omega\rangle \\
= \; & \sum_{\vec{x_2}\vec{x_1}} \sum_{j,k} \sum_{\vec{p_i},\vec{p_f}} \sum_{s,s'} e^{-i\vec{p'}.\vec{x_2}} e^{i\vec{p'}.\vec{x_1}} e^{-i\vec{p}.\vec{x_1}} e^{i\vec{p_f}.\vec{x_2}} e^{-iE^{(k)}_{\vec{p}_f} t_2} e^{-i\vec{p_f}.\vec{x_1}} e^{iE^{(k)}_{\vec{p}_f} t_1} e^{i\vec{p_i}.\vec{x_1}} e^{-iE^{(j)}_{\vec{p_i}} t_1} \\
\times \; & \langle\Omega|\chi_\mu|p_f, s'\rangle\langle p_f, s'|J^\alpha|p_i, s\rangle\langle p_i, s|\chi^\dagger_\nu|\Omega\rangle \\
= \; & \sum_{\vec{x_1}} \sum_{j,k} \sum_{\vec{p_i}} \sum_{s,s'} e^{-i(\vec{p}-\vec{p_i}).\vec{x_1}} e^{-iE^{(k)}_{\vec{p}'} t_2} e^{iE^{(k)}_{\vec{p}'} t_1} e^{-iE^{(j)}_{\vec{p_i}} t_1} \\
\times \; & \langle\Omega|\chi_\mu|p', s'\rangle\langle p', s'|J^\alpha|p_i, s\rangle\langle p_i, s|\chi^\dagger_\nu|\Omega\rangle \\
= \; & \sum_{i,j} \sum_{s,s'} e^{-iE^{(k)}_{\vec{p}'} t_2} e^{iE^{(k)}_{\vec{p}'} t_1} e^{-iE^{(j)}_{\vec{p}} t_1} \langle\Omega|\chi_\mu|p', s'\rangle\langle p', s'|J^\alpha|p, s\rangle\langle p, s|\chi^\dagger_\nu|\Omega\rangle \qquad (5.2)
\end{aligned}$$

We then perform an analytic continuation to Euclidean spacetime via the replacement $t \to -it$. For large t_1 and large $t_2 - t_1$ the ground state signal dominates.

The time dependence of Eq. (5.2) can be removed by taking ratios with the two-point function defined in Eq. (3.7). By careful choice of the form we can also remove any constants of normalisation. Thus we form the ratio

$$\begin{aligned}
R_{\mu\alpha\nu}(p', p) = & \sqrt{\frac{\Big\langle G_{\mu\alpha\nu}(\vec{p'}, \vec{p}, t, t_1)\Big\rangle \Big\langle G_{\nu\alpha\mu}(\vec{p}, \vec{p'}, t, t_1)\Big\rangle}{<G_{\mu\mu}(\vec{p'}, t)> <G_{\nu\nu}(\vec{p}, t)>}} \qquad (5.3) \\
= \; & \sum_{s,s'} \sqrt{\frac{\langle\Omega|\chi_\mu|p', s'\rangle\langle p', s'|J_\alpha|p, s\rangle\langle p, s|\chi^\dagger_\nu|\Omega\rangle\langle\Omega|\chi_\nu|p, s\rangle\langle p, s|J_\alpha|p', s'\rangle\langle p', s'|\chi^\dagger_\mu|\Omega\rangle}{\langle\Omega|\chi_\mu|p', s'\rangle\langle p', s'|\chi^\dagger_\mu|\Omega\rangle\langle\Omega|\chi_\nu|p, s\rangle\langle p, s|\chi^\dagger_\nu|\Omega\rangle}},
\end{aligned}$$

which has no remaining time-dependence. This method is a variant of that used by Draper *et al.* [19], differing in the choice of momenta used in the numerator.

5.2.1 π-meson case

For a pion, the vertex is extraordinarily simple. As the spin is zero, s and s' play a trivial role. Including the state normalization factors of $1/\sqrt{2E_{\vec{p}}}$

$$\langle p'|J_\alpha|p\rangle = \frac{1}{2\sqrt{E_p E_{p'}}}\,[p_\alpha + p'_\alpha]F_1(Q^2) = \langle p|J_\alpha|p'\rangle\ . \tag{5.4}$$

Defining

$$\langle\Omega|\chi(0)|p\rangle = \frac{1}{\sqrt{2E}}\lambda(p)\,,$$

$$\langle\Omega|\chi(0)|p'\rangle\langle p'|J_\alpha|p\rangle\langle p|\chi^\dagger(0)|\Omega\rangle = \lambda(p')\tilde{\lambda}(p)\frac{1}{4E_p E_{p'}}\,[p_\alpha + p'_\alpha]F_1(Q^2)\ . \tag{5.5}$$

Using the same parameterisation, the expressions in the denominator evaluate to

$$\begin{aligned}&\langle\Omega|\chi_\mu(0)|p',s'\rangle\langle p',s'|\chi^\dagger_\mu(0)|\Omega\rangle\langle\Omega|\chi_\nu(0)|p,s\rangle\langle p,s|\chi^\dagger_\nu(0)|\Omega\rangle\\ &= \frac{1}{4E_p E_{p'}}\,\lambda(p')\tilde{\lambda}(p')\lambda(p)\tilde{\lambda}(p)\,.\end{aligned} \tag{5.6}$$

Thus we have no remaining couplings λ in the ratio, and we can rewrite 5.4 as

$$\sqrt{\frac{\left(\frac{1}{4E_pE_{p'}}\,[p_\alpha + p'^\alpha]F_1(Q^2)\right)^2}{\frac{1}{4E_pE_{p'}}}} \tag{5.7}$$

This reduces to simply

$$R_{\alpha\mu\nu}(p',p) \to R_\alpha(p',p) = \frac{1}{2\sqrt{E_pE_{p'}}}\,[p^\alpha + p'^\alpha]F_1(Q^2)\,, \tag{5.8}$$

such that the large Euclidean time limits of the ratio R_α is a direct measure of $F_1(Q^2)$ up to kinematical factors.

Inverting to give F_1, or G_C to use the notation we will adopt for the vector case gives:

$$F_1(Q^2) = G_C(Q^2) = \frac{2\sqrt{E_pE'_p}}{p^\alpha + p'^\alpha}R^\alpha(p,p') \tag{5.9}$$

5.2.2 Spin-1 case

Following [15], we may write the vector current matrix element as

$$\langle p's'|J^\mu|ps\rangle = \frac{1}{2\sqrt{E_pE_{p'}}}\,\epsilon'^\star_\alpha(p',s')\epsilon_\beta(p,s)J^{\alpha\mu\beta}(p',p)$$

where

$$J^{\alpha\mu\beta}(p',p) = -\left\{ G_1(Q^2)\, g^{\alpha\beta}\, [p^\mu + p'^\mu] + G_2(Q^2)[g^{\mu\beta}q^\alpha - g^{\mu\alpha}q^\beta] - G_3(Q^2)\, q^\beta q^\alpha\, \frac{p^\mu + p'^\mu}{2m^2} \right\} \tag{5.10}$$

defines the covariant vertex functions $G_{1,2,3}$.

As in Chapter 3, we denote the vacuum couplings as follows:

$$\begin{aligned} \langle\Omega|\, \chi^i_\mu \,|n, \vec{p}\,', s\rangle &= \lambda^i_n\, \epsilon_\mu(p\,', s) \\ \langle n, \vec{p}\,', s|\, \chi^{j\,\dagger}_\nu \,|\Omega\rangle &= \lambda^{j\star}_{\;n}\, \epsilon^\star_\nu(p\,', s) \end{aligned}$$

where the on-shell four-vector $p\,' = (E_n, \vec{p}\,')$ is introduced, with $E_n = \sqrt{\vec{p}^{\,2} + m_n^2}$.

The Sachs form-factors are related to the covariant vertex functions as follows [15]:

$$G_Q(Q^2) = G_1(Q^2) - G_2(Q^2) + (1+\eta)G_3(Q^2) \tag{5.11}$$

$$G_M(Q^2) = G_2(Q^2) \tag{5.12}$$

$$G_C(Q^2) = G_1(Q^2) + \frac{2}{3}\eta G_Q(Q^2)\,, \tag{5.13}$$

where $\eta = Q^2/4m^2$ and $Q^2 = -q^2 = \vec{q}^{\,2} - q_0^2$.

The expression for $J^{\alpha\mu\beta}(p',p)$ may be written directly in terms of the Sachs form-factors:

$$\begin{aligned} J^{\alpha\mu\beta}(p',p) = \\ -\Bigg\{\; & G_M(Q^2)\Big([g^{\mu\beta}q^\alpha - g^{\mu\alpha}q^\beta] - g^{\alpha\beta}\frac{p^\mu + p'^\mu}{2(1+\eta)m^2}\Big) \\ & + G_C(Q^2)[p^\mu + p'^\mu]\Big(g^{\alpha\beta} - \frac{q^\alpha q^\beta}{2(1+\eta)m^2}\Big) \\ & - G_Q(Q^2)[p^\mu + p'^\mu]\Big(\frac{2\eta}{3}g^{\alpha\beta} + (2\eta+3)\frac{q^\alpha q^\beta}{6(\eta+1)m^2}\Big) \;\Bigg\} \end{aligned} \tag{5.14}$$

The quantity of interest is

$$\begin{aligned} & \sum_{s,s'} \langle\Omega|\chi_\mu|p'\,s'\rangle\langle p'\,s'|J^\alpha|p\,s\rangle\langle p\,s|\chi^\dagger_\nu|\Omega\rangle \\ = \; & -\frac{1}{4E_pE_{p'}}\,\lambda(p')\tilde{\lambda}^\star(p)(g_{\mu\alpha} - \frac{p'_\mu p'_\alpha}{m^2})\, J^{\alpha\mu\beta}(g_{\beta\mu} - \frac{p_\beta p_\mu}{m^2})\,, \end{aligned} \tag{5.15}$$

where we have made use of the transversality condition,

$$\sum_s \epsilon_\mu(p,s)\, \epsilon^\star_\nu(p,s) = -\left(g_{\mu\nu} - \frac{p_\mu p_\nu}{m^2}\right)\,,$$

to evaluate the sum over spin states.

As can be seen, the vacuum couplings cancel in the ratio of Eq. (5.4) to provide

$$R_{\mu\alpha\nu}(p',p) = \frac{1}{2\sqrt{E_p E_{p'}}} \times$$
$$\sqrt{\frac{(g_{\mu\rho} - \frac{p'_\mu p'_\rho}{m^2}) J^{\rho\alpha\sigma}(p',p)(g_{\sigma\nu} - \frac{p_\sigma p_\nu}{m^2})(g_{\nu\gamma} - \frac{p_\nu p_\gamma}{m^2}) J^{\gamma\alpha\delta}(p,p')(g_{\delta\mu} - \frac{p'_\delta p'_\mu}{m^2})}{(g_{\mu\mu} - \frac{p'_\mu p'_\mu}{m^2})(g_{\nu\nu} - \frac{p_\nu p_\nu}{m^2})}}$$

From Eq. (5.10) we have the following symmetry

$$J^{\alpha\mu\beta}(p',p) = J^{\beta\mu\alpha}(p,p')$$

and we may thus take the square root, yielding

$$R_{\mu\alpha\nu}(p',p) = \frac{1}{2\sqrt{E_p E_{p'}}} \frac{(g_{\mu\rho} - \frac{{p'}_\mu {p'}_\rho}{m^2}) J^{\rho\alpha\sigma}(p',p)(g_{\sigma\nu} - \frac{p_\sigma p_\nu}{m^2})}{\sqrt{(g_{\mu\mu} - \frac{{p'}_\mu {p'}_\mu}{m^2})(g_{\nu\nu} - \frac{p_\nu p_\nu}{m^2})}} \tag{5.16}$$

In our calculations, we have chosen $p' = k = (E, p_x, 0, 0)$ and $p = l = (m, 0, 0, 0)$. In this case, the following identity holds

$$\left(g_{\alpha\beta} - \frac{l_\alpha l_\beta}{m^2}\right) = \delta_{\alpha\beta}\left(\delta_{\beta 0} - 1\right), \tag{5.17}$$

and we can simplify Eq. (5.16) to

$$R_{\mu\alpha\nu}(k,l) = \frac{1}{2\sqrt{Em}} \left(g_{\mu\rho} - \frac{k_\mu k_\rho}{m^2}\right) J^{\rho\alpha\nu}(k,l) \sqrt{\frac{(\delta_{\nu 0} - 1)}{(g_{\mu\mu} - \frac{k_\mu k_\mu}{m^2})}}\,. \tag{5.18}$$

Henceforth, when we refer to R we shall mean $R(k,l)$. A straightforward calculation (see appendix E for a REDUCE script that implements this) yields the following:

$$\begin{aligned}
R_{101} &= \frac{G_3(Q^2)\,(E+m)p_x^2 - 2\,G_2(Q^2)\,mp_x^2 + 2G_1(Q^2)\,Em(E+m)}{4m^2\sqrt{Em}} \\
R_{133} = R_{331} &= \frac{p_x}{2\sqrt{Em}}\,G_2(Q^2) \\
R_{202} = R_{303} &= \frac{(E+m)}{2\sqrt{Em}}\,G_1(Q^2)\,.
\end{aligned}$$

In terms of the Sachs form-factors,

$$\begin{aligned}
R_{101} &= \frac{p_x^2}{3m\sqrt{Em}} G_Q(Q^2) + \frac{E+m}{2\sqrt{Em}} G_C(Q^2) \\
R_{202} = R_{303} &= -\frac{p_x^2}{6m\sqrt{Em}} G_Q(Q^2) + \frac{E+m}{2\sqrt{Em}} G_C(Q^2) \\
R_{133} = R_{331} &= \frac{p_x}{2\sqrt{Em}} G_M(Q^2)\,.
\end{aligned}$$

Rearranging, we see that the linear combinations isolating the form-factors are the following:

$$
\begin{aligned}
G_C(Q^2) &= \frac{2}{3}\frac{\sqrt{Em}}{E+m}\left(R_{101}+R_{202}+R_{303}\right) && (5.19)\\
G_M(Q^2) &= \frac{\sqrt{Em}}{p_x}\left(R_{133}+R_{331}\right) && (5.20)\\
G_Q(Q^2) &= \frac{m\sqrt{Em}}{p_x^2}\left(2R_{101}-R_{202}-R_{303}\right) && (5.21)
\end{aligned}
$$

5.2.3 Extracting static quantities

At $Q^2 = 0$, the Sachs form factors are proportional to various static quantities of interest. Specifically:

$$
\begin{aligned}
eG_C(0) &= e,\\
eG_M(0) &= 2m\mu_1,\\
eG_Q(0) &= m^2 Q_1, && (5.22)
\end{aligned}
$$

where m is the mass of the spin-1 system, μ_1 is the magnetic moment, Q_1 is the quadrupole moment, and e is the charge of the system.

Our calculations will be performed at a single, finite Q^2. At $Q^2 = 0$, $q_x = q_y = q_z = 0$, and therefore in the laboratory frame considered here, $p_x = p_y = p_z = 0$. The presence of p_x in the denominator of expressions for G_M and G_Q in Eq. (5.19) prevents us, in this case, from extracting information about the magnetic and quadrupole form-factors. Moreover, our use of a conserved vector current guarantees that $G_C(Q^2 = 0) = 1$, and this fact has been used to test our implementation of the above formalism.

It remains to show how we can extrapolate to zero momentum transfer. We do so as follows.

Charge form-factor and $\langle r^2\rangle$

The mean squared charge radius is given by $\langle r^2\rangle = \int dr\, r^2\rho(r)$, where r is the distance from the centre of mass of the system. We can obtain $\langle r^2\rangle$ from the charge form-factor through the following relation[1]:

$$
\langle r^2\rangle = -6\frac{\partial}{\partial Q^2}G(Q^2)\Big|_{Q^2=0}. \qquad (5.23)
$$

We extrapolate to $Q^2 = 0$ through a 1-parameter phenomenological form for G_C. A convenient form is the monopole:

$$
G_C(Q^2) = \left(\frac{1}{\frac{Q^2}{\Lambda^2}+1}\right). \qquad (5.24)
$$

---

[1] This is derived explicitly in Appendix B

Inserting this form into Eq. (5.23) gives

$$\langle r^2 \rangle = \frac{6}{\Lambda^2} \,. \tag{5.25}$$

Rearranging Eq. (5.24) to give Λ^2 yields

$$\Lambda^2 = \frac{Q^2}{(\frac{1}{G_C(Q^2)} - 1)} \tag{5.26}$$

Substituting this back in to the previous expression for $\langle r^2 \rangle$ gives

$$\langle r^2 \rangle = \frac{6}{Q^2} \left(\frac{1}{G_C(Q^2)} - 1 \right) \tag{5.27}$$

Choosing a dipole form instead of the above yields a result which is smaller by approximately 7%, which is comparable to the statistical error in this calculation.

Magnetic moment

From studies of nucleon moments, it is observed that the scaling of G_M and G_C in Q^2 is very similar when Q^2 is small [36]. *i.e.* if

$$G_M(Q^2) = F(Q^2) G_M(0)$$

for some function F then

$$G_C(Q^2) \simeq F(Q^2) G_C(0) \,.$$

Rearranging gives

$$\frac{G_M(0)}{G_C(0)} \simeq \frac{G_M(Q^2)}{G_C(Q^2)} \,. \tag{5.28}$$

We shall simply assume that this scaling will also hold for a meson. Since for a ρ^+ meson, $G_C(0) = 1$, this is simply

$$G_M(0) \simeq \frac{G_M(Q^2)}{G_C(Q^2)} \,. \tag{5.29}$$

Quadrupole form-factor

The Quadrupole tensor is defined as

$$Q_{ij} = \int d^3 r \rho(\vec{r}) (3 r_i r_j - \delta_{ij} r^2) \,. \tag{5.30}$$

Then

$$Q_{11} = \int d^3 r \rho(\vec{r}) (3 r_1^2 - r^2) = \int d^3 r \rho(\vec{r}) (2 r_1^2 - r_2^2 - r_3^2) \tag{5.31}$$

which is exactly the form of our G_Q - recall:

$$G_Q(Q^2) = \frac{m\sqrt{Em}}{p_x^2}\left(2\tilde{R}_{101} - \tilde{R}_{202} - \tilde{R}_{303}\right)$$

We can clearly see that a negative value of G_Q corresponds to an oblate deformation - a shape which is larger in the directions perpendicular to the spin than parallel to it.

More rigorously, write

$$J^{\alpha\mu\beta}(p,p') = -G_M(Q^2)F_M^{\alpha\mu\beta}(p,p') + G_C(Q^2)F_C^{\alpha\mu\beta}(p,p') + G_Q(Q^2)F_Q^{\alpha\mu\beta}(p,p')$$

then by comparison with Eq. (5.14) we have:

$$F_Q^{\alpha\mu\beta}(p,p') = \frac{2\eta}{3}[p^\mu + p'^\mu](-F_C(p,p') + \frac{4\eta+3}{4\eta(\eta+1)m^2}q^\alpha q^\beta)\,.$$

Recalling that $p' = k = (E, p_x, 0, 0)$ and $p = l = (m, 0, 0, 0)$, we have $q = (E - m, p_x, 0, 0)$, and so

$$F_Q^{\alpha\mu\beta}(p,p') = \frac{2\eta}{3}[p^\mu + p'^\mu](-F_C(p,p') + (\frac{2E+m}{mp_x^2})q^\alpha q^\beta)\,.$$

For spatial α and β, this is

$$F_Q^{\alpha\mu\beta}(p,p') = \frac{2\eta}{3}[p^\mu + p'^\mu]\left(-F_C(p,p') + (1 + \frac{2E}{m})\delta_{\alpha 1}\delta_{\beta 1}\right)\,.$$

which we recognise as a difference of terms involving the charge form-factor in all directions and the chosen 1 direction. Comparing with Eq. (5.30), we see that this in turn corresponds to a quadrupole moment about the 1 axis.

Whilst a similar scaling to that used in the case of the magnetic form-factor could be used to relate our quadrupole form-factor to the moment, we believe that the form-factor at our small finite Q^2 ($\simeq 0.22\mathrm{GeV}$) will be of greater phenomenological interest.

5.3 Method

Two- and three-point correlation functions of the kind described above were calculated on a lattice of dimensions $20^3 \times 40$, with lattice parameter $\beta = 4.53$, corresponding to a lattice spacing of $0.128(2)\,\mathrm{fm}$. For full details of this lattice, the reader may refer to Chapter 3 of this text.

Three point propagators, detailed in appendix D, encoding a quark interacting with a photon at some intermediate time between creation and annhilation, were created using the sequential source technique (SST) [19]. An improved lattice definition of the conserved vector current [39] was employed, with the current insertion occuring at time $t = 14$. The strange quark mass is chosen to be the third heaviest quark mass. This provides a pseudoscalar mass of 697 MeV which compares well with the experimental value of $(2M_K^2 - M_\pi^2)^{1/2} = 693\,\mathrm{MeV}$ motivated by leading order chiral perturbation theory.

An ensemble of 379 configurations was used, with error analysis of the correlation function ratios performed via a second-order, single-elimination jack-knife. We then performed a series of fits through the ratios after the current insertion at $t = 14$. Through examining the χ^2 value as determined through the covariance matrix we are able to establish a valid window through which we may fit in order to extract our observables. In all cases, we required a value of χ^2 no larger than 1.4. The data from which these graphs are derived is presented in tabular form in appendix F. Values quoted on a per quark-sector basis correspond exclusively to values for single quarks of unit charge.

5.4 Results

The following plots show the time-evolution behaviour of the correlation function ratios we use to measure form-factors. Vertical bars depict the limits of the fit windows we have used in this analysis. Care has been taken to choose consistent windows across the quark-sectors in order to eliminate systematic errors in comparisons we will later undertake to determine mass and environment sensitivities.

We perform direct fits to the correlators for the 3 heaviest quark masses, and fit the splittings between adjacent quark masses (*i.e.* $G_i - G_{i+1}$) for the five lightest quark masses. By fitting the splittings significant cancellation of excited state contributions is observed. Indeed, the $\chi^2/\mathrm{d.o.f}$ analysis encourages fits at earlier time slices and confirms that systematic errors are within the statistical errors.

Figures 5.2, 5.3, and 5.4 show the Charge form-factor ratio for the light quark in a pion, the light-quark in a Kaon, and the strange quark in a Kaon respectively. Statistical fluctuations are very small, allowing as many as twelve timeslices to be used in constraining our fit.

Figures 5.5, 5.6, and 5.7 show the Charge form-factor ratio for the light quark in a ρ-meson, the light-quark in a K^*, and the strange quark in a K^* respectively. Statistical fluctuations are larger than for the pseudoscalar case, but we have no particular difficulty establishing a consistent and valid fit regime across all three quark-sectors.

In figures 5.8, 5.9, and 5.10 we show the Magnetic form-factor for the light quark in a ρ-meson, the light-quark in a K^*, and the strange quark in a K^* respectively. This data is considerably noisier than for G_C, and exhibits a rapid die-off of signal with time as we go to lighter quark-masses. Care must be taken when attempting to fit a constant to this data, but we are nevertheless able to obtain a consistent fit regime across all quark-sectors with a good χ^2 value.

Figures 5.11, 5.12, and 5.13 we show the Quadrupole form-factor for the light quark in a ρ-meson, the light-quark in a K^*, and the strange quark in a K^* respectively. The signal is noisier again than for the magnetic case, but we are able to fit self-consistently to the data across all quark-sectors.

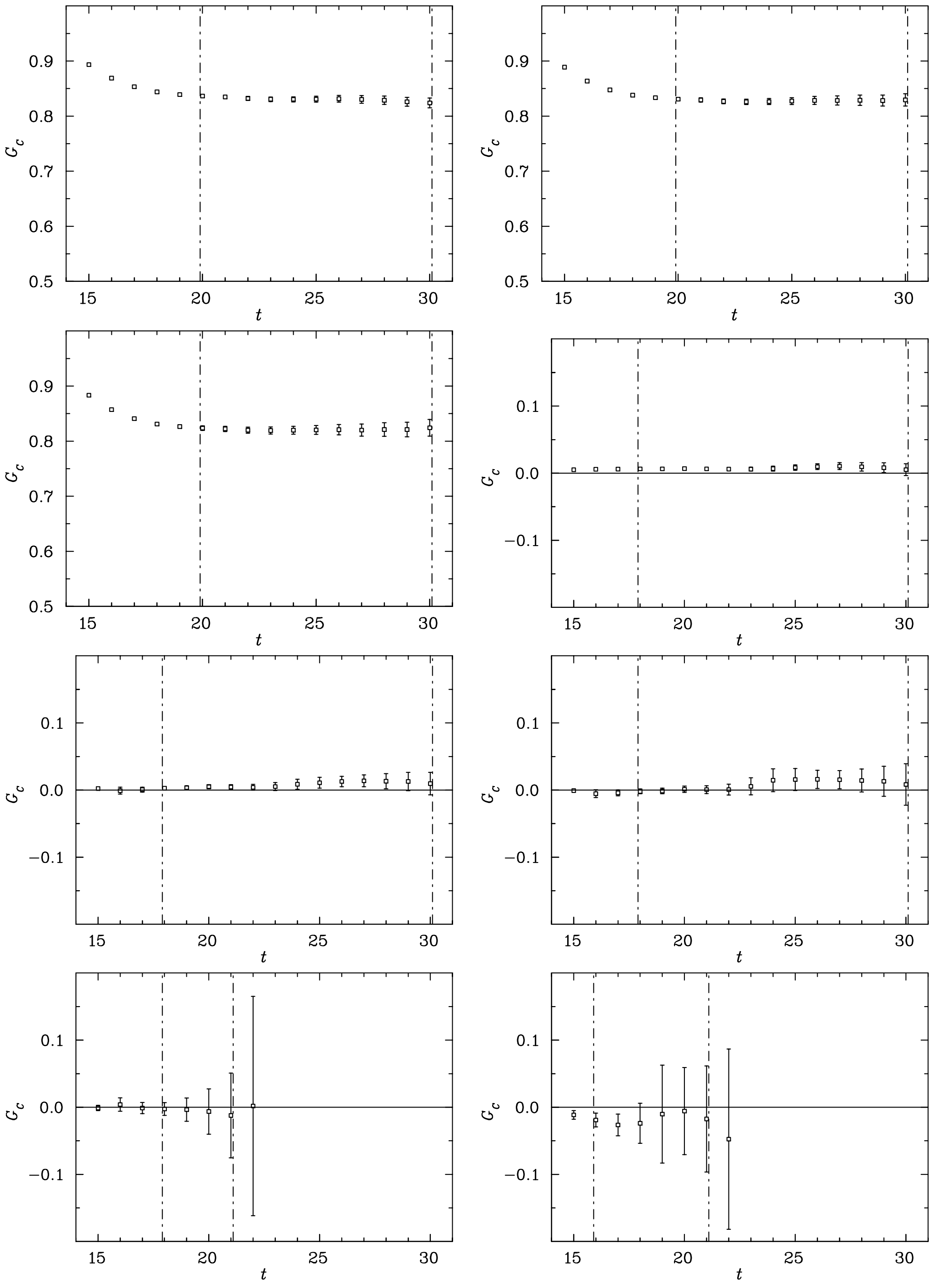

Fig. 5.2: The up-quark contribution to pion charge form factor. The data correspond to $m_\pi \simeq 830\,\mathrm{MeV}$ (top left), $770\,\mathrm{MeV}$ (top right), $700\,\mathrm{MeV}$ (second row left), $616\,\mathrm{MeV}$ (second row right), $530\,\mathrm{MeV}$ (third row left), $460\,\mathrm{MeV}$ (third row right), $367\,\mathrm{MeV}$ (bottom row left), and $290\,\mathrm{MeV}$ (bottom row right). For the five lightest quark masses, the splitting between the values for i_κ and $i_\kappa+1$ is shown. The data are illustrated only to the point at which the error bars diverge.

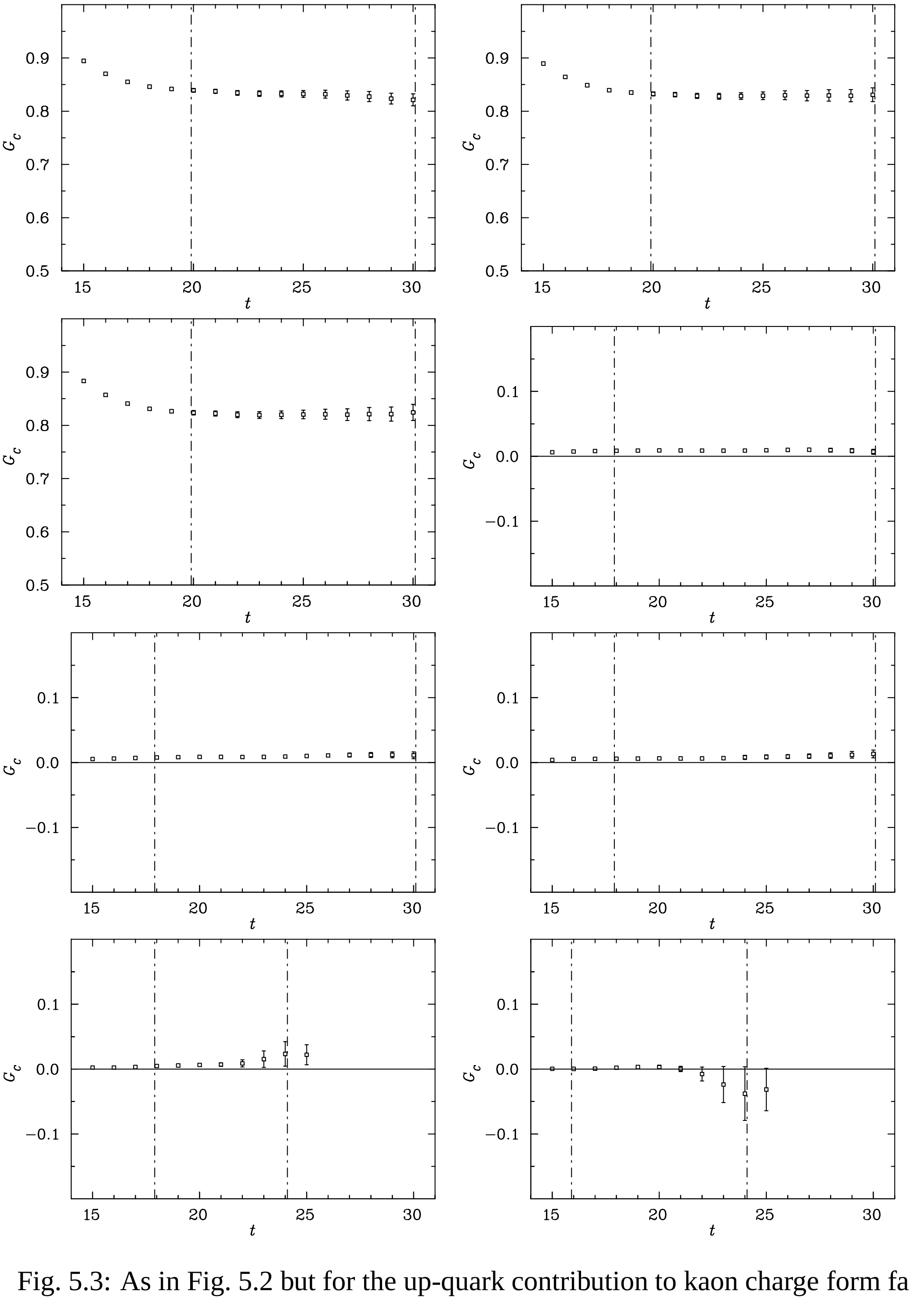

Fig. 5.3: As in Fig. 5.2 but for the up-quark contribution to kaon charge form factor.

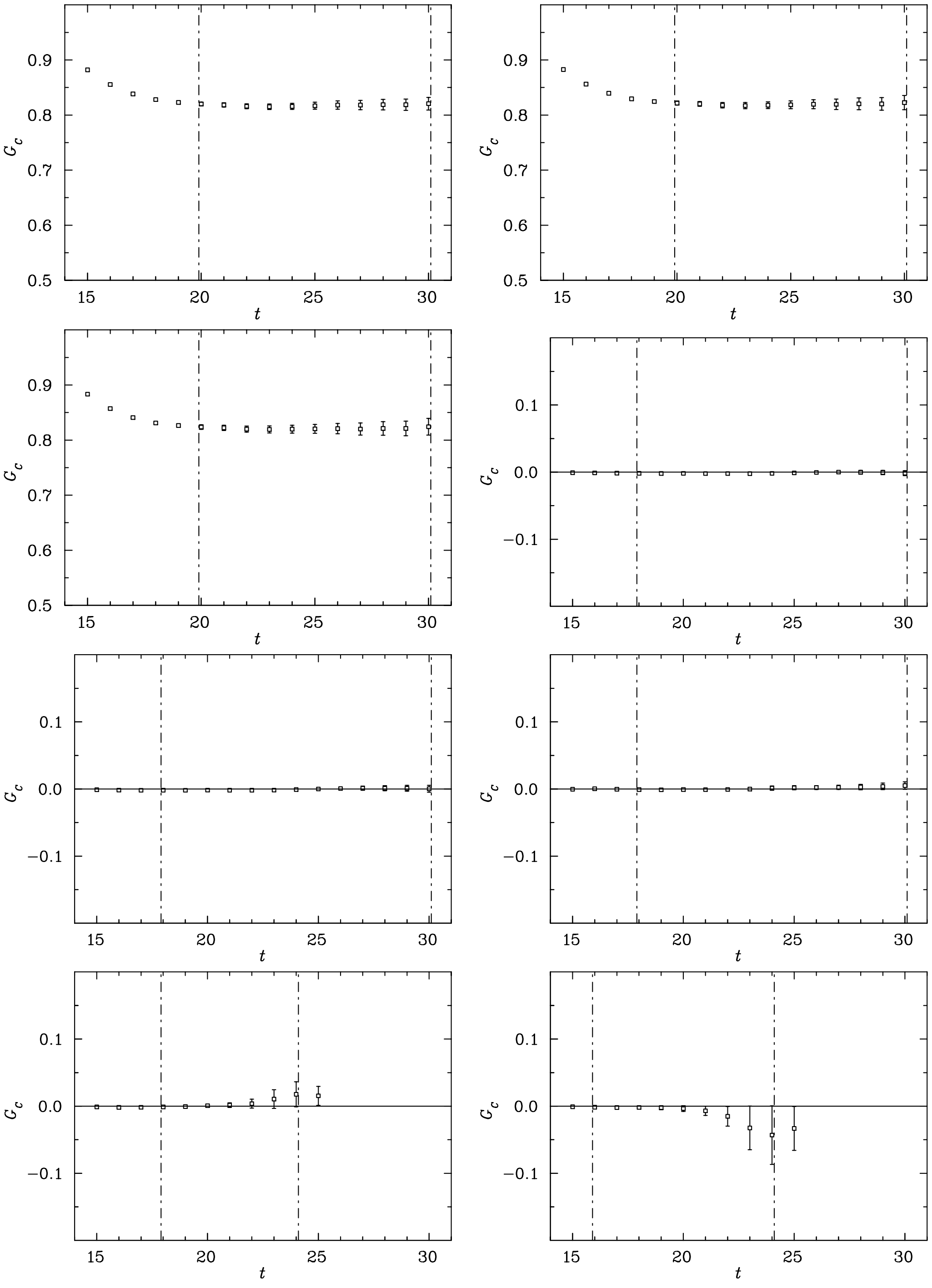

Fig. 5.4: As in Fig. 5.2 but for the strange-quark contribution to kaon charge form factor.

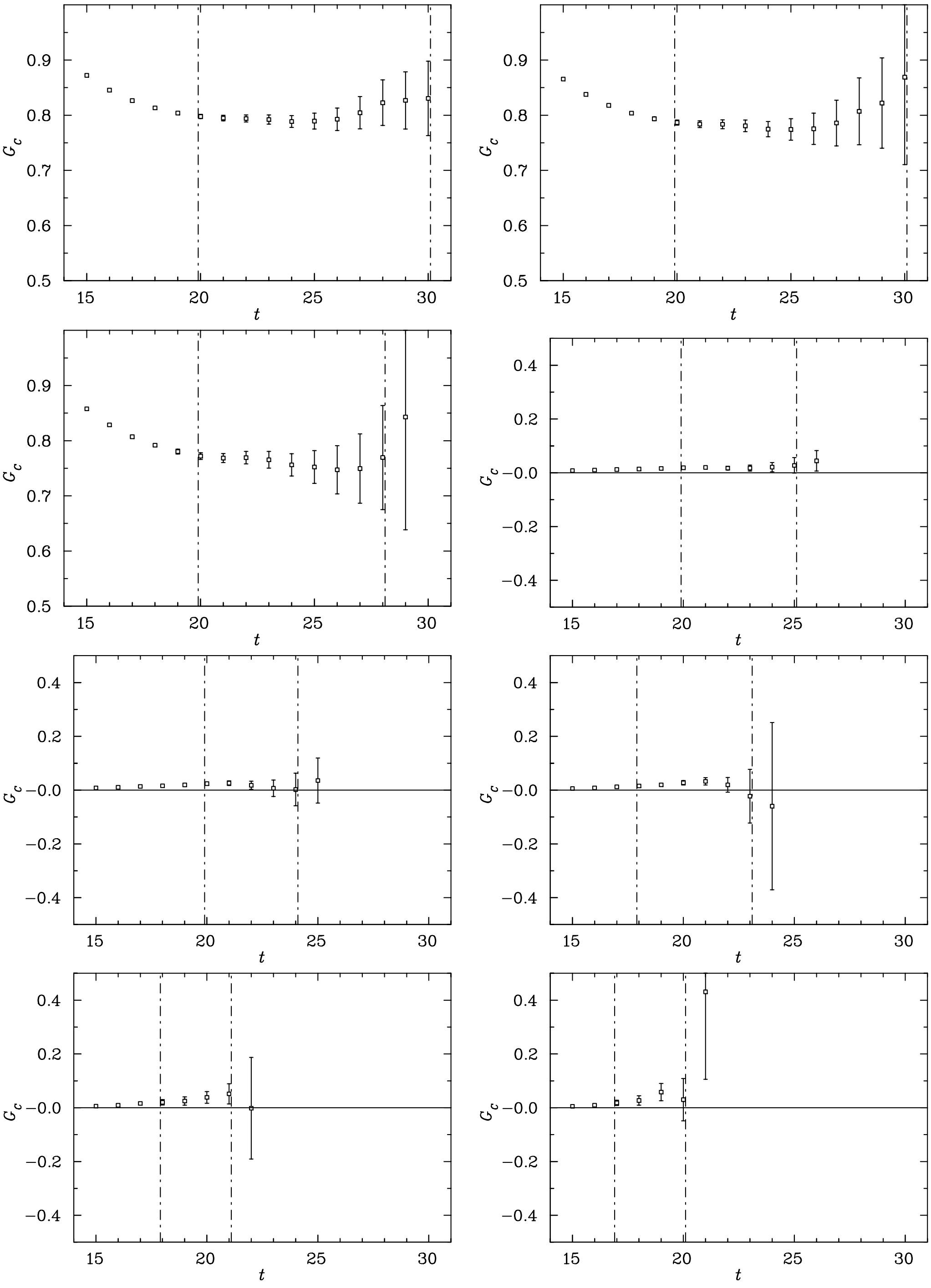

Fig. 5.5: As in Fig. 5.2 but for the up-quark contribution to ρ charge form factor.

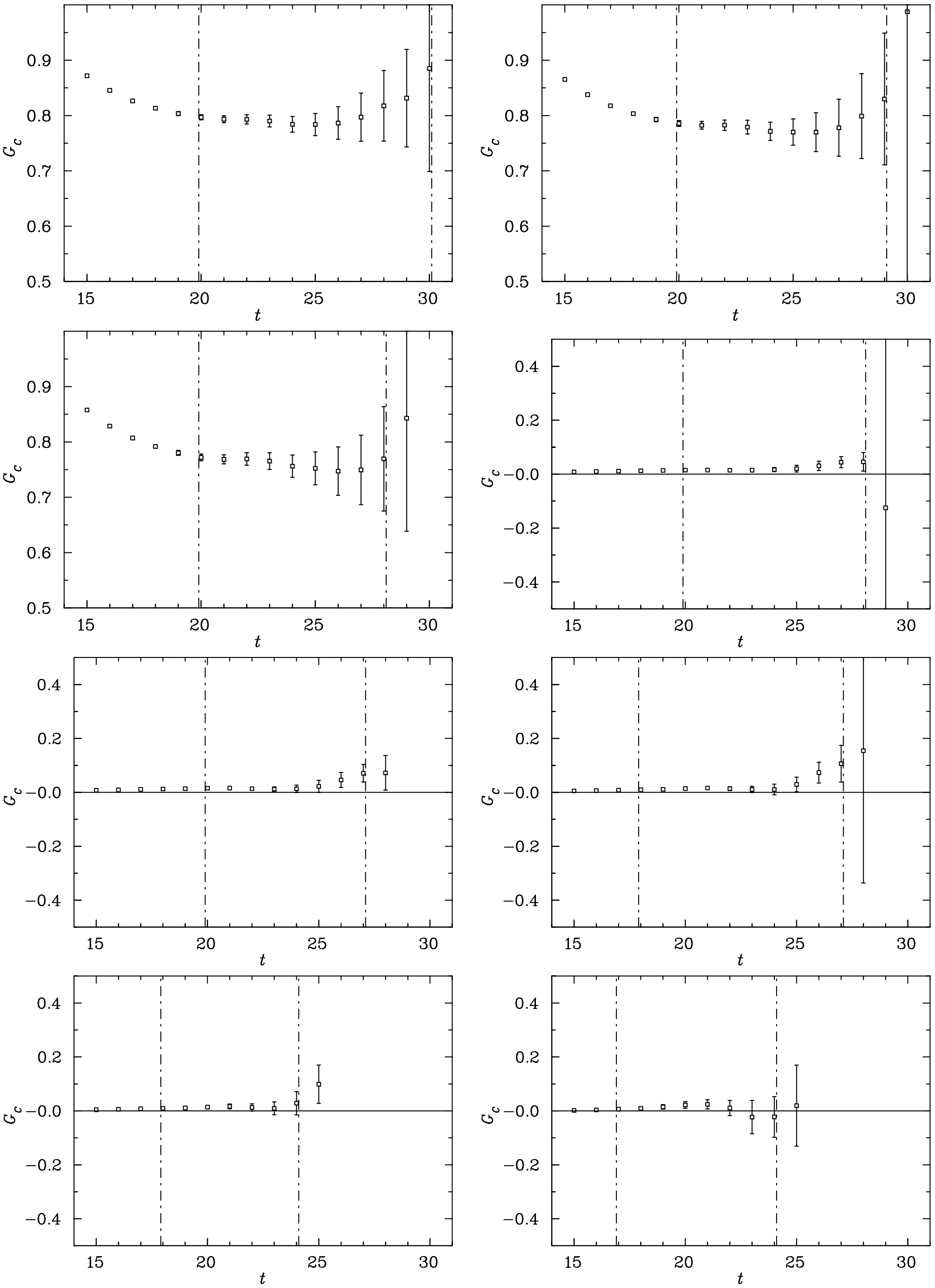

Fig. 5.6: As in Fig. 5.2 but for the up-quark contribution to K^* charge form factor.

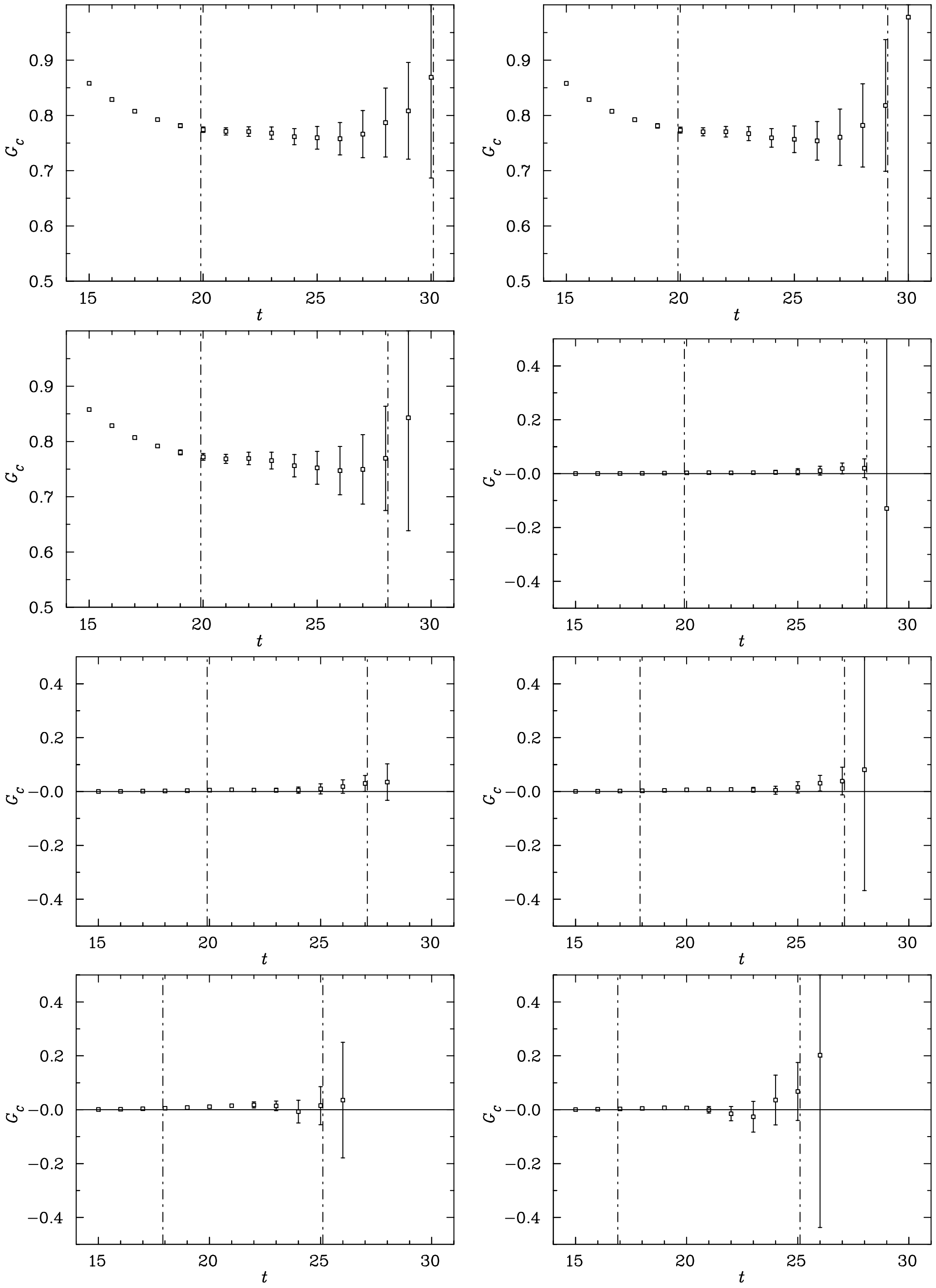

Fig. 5.7: As in Fig. 5.2 but for the strange-quark contribution to K^* charge form factor.

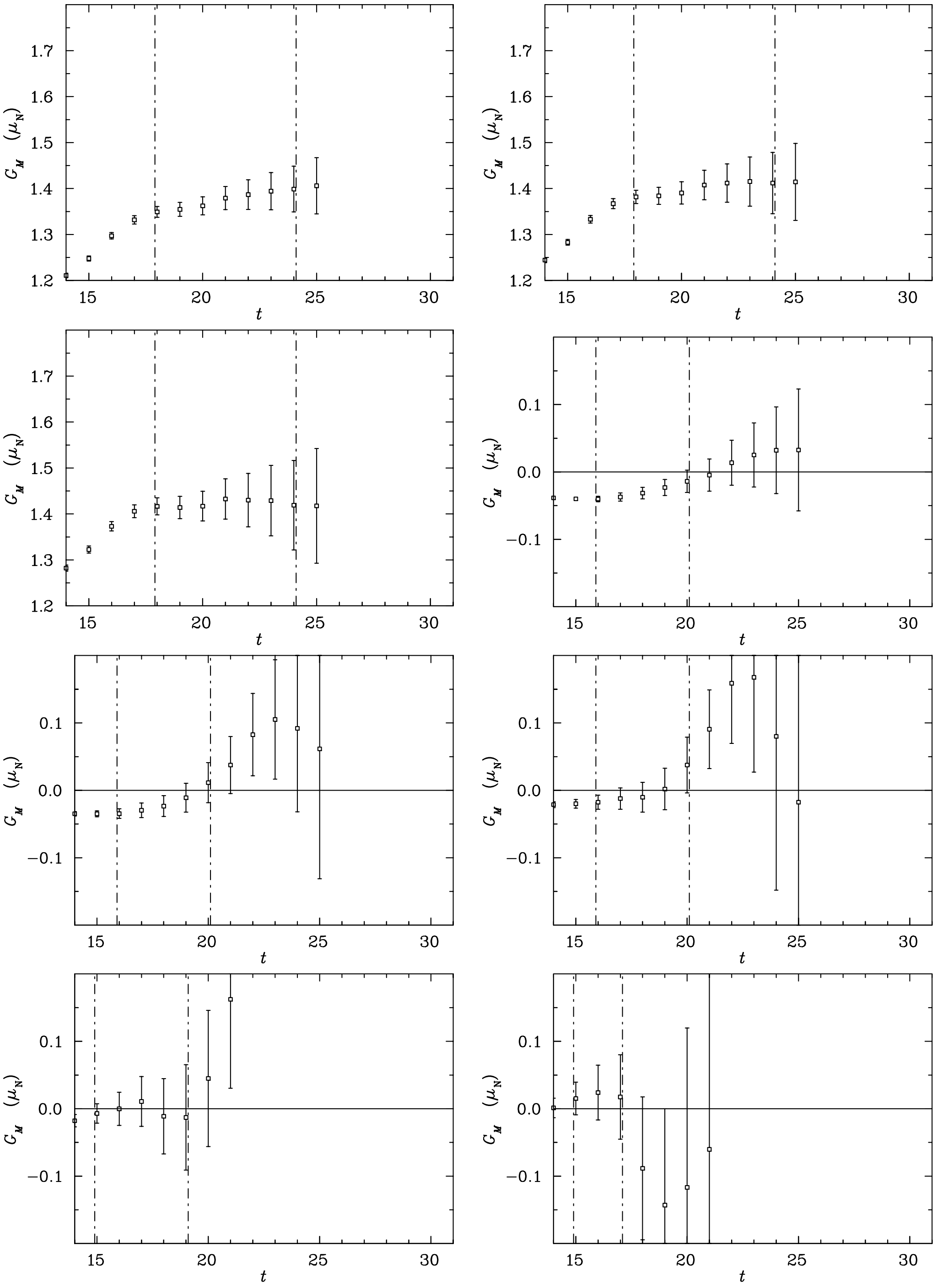

Fig. 5.8: As in Fig. 5.2 but for the up-quark contribution to ρ magnetic form factor. We note that for the fifth and sixth quark mass, good $\chi^2/\mathrm{d.o.f}$ is achieved for fits including points to $t = 25$, and central value of the fit is not afected significantly. We prefer to focus on regions of good signal.

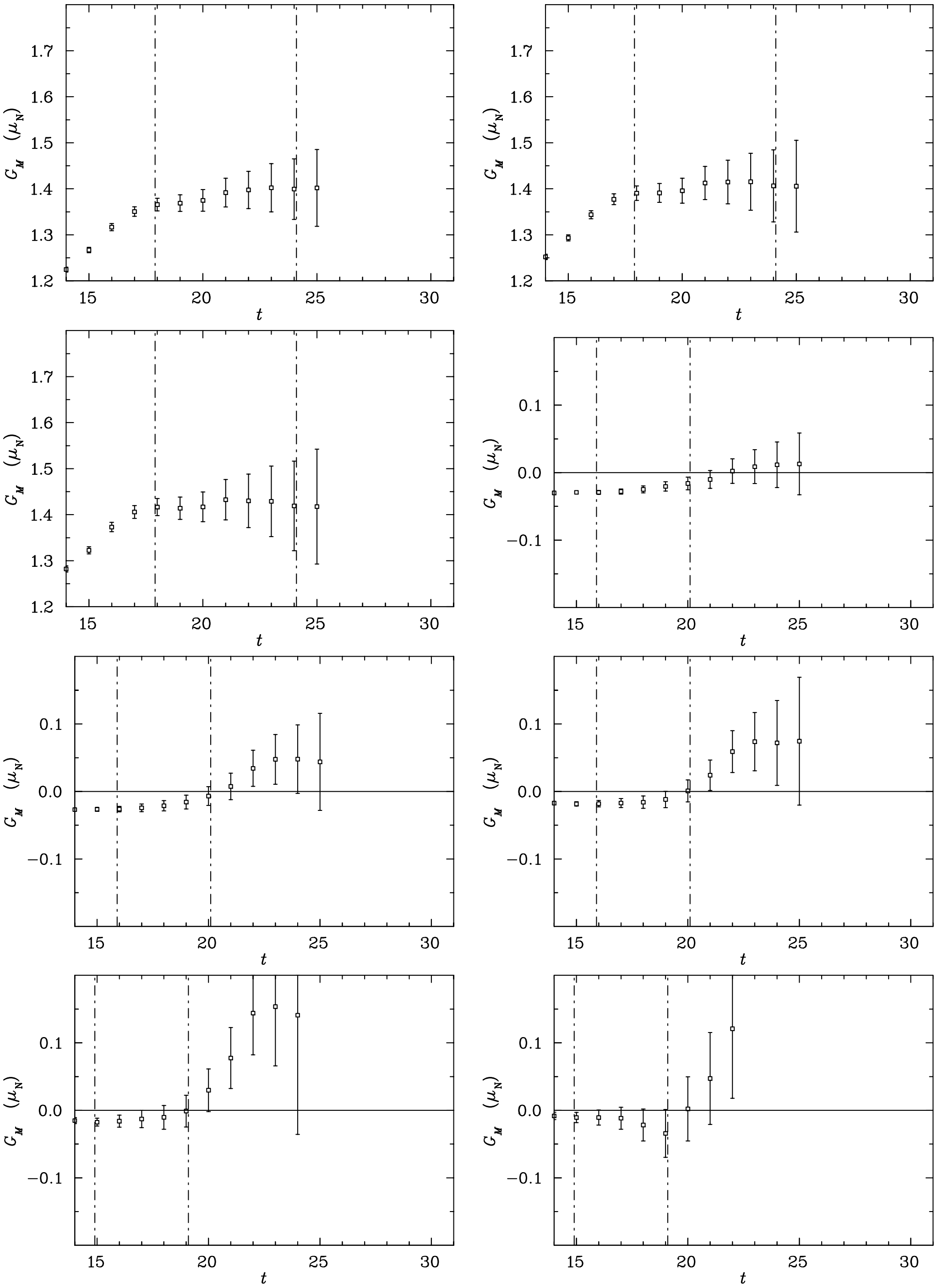

Fig. 5.9: As in Fig. 5.2 but for the up-quark contribution to K^* magnetic form factor. As for the up contributions, we can achieve a good χ^2 even fitting out to $t = 25$ for the fifth, sixth and seventh quark masses without significantly affecting the central values, but prefer to focus on regions of strong signal.

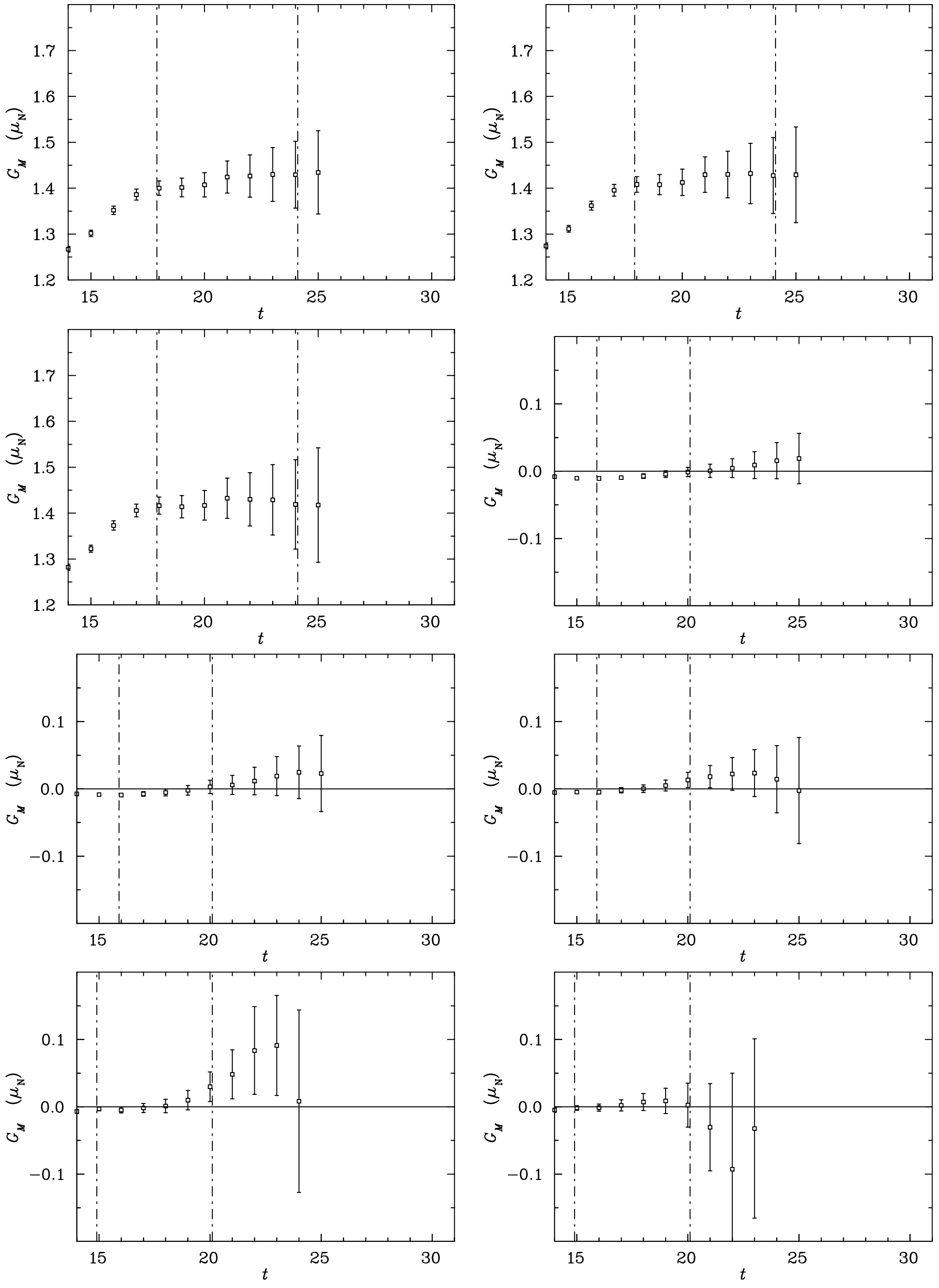

Fig. 5.10: As in Fig. 5.2 but for the strange-quark contribution to K^* magnetic form factor.

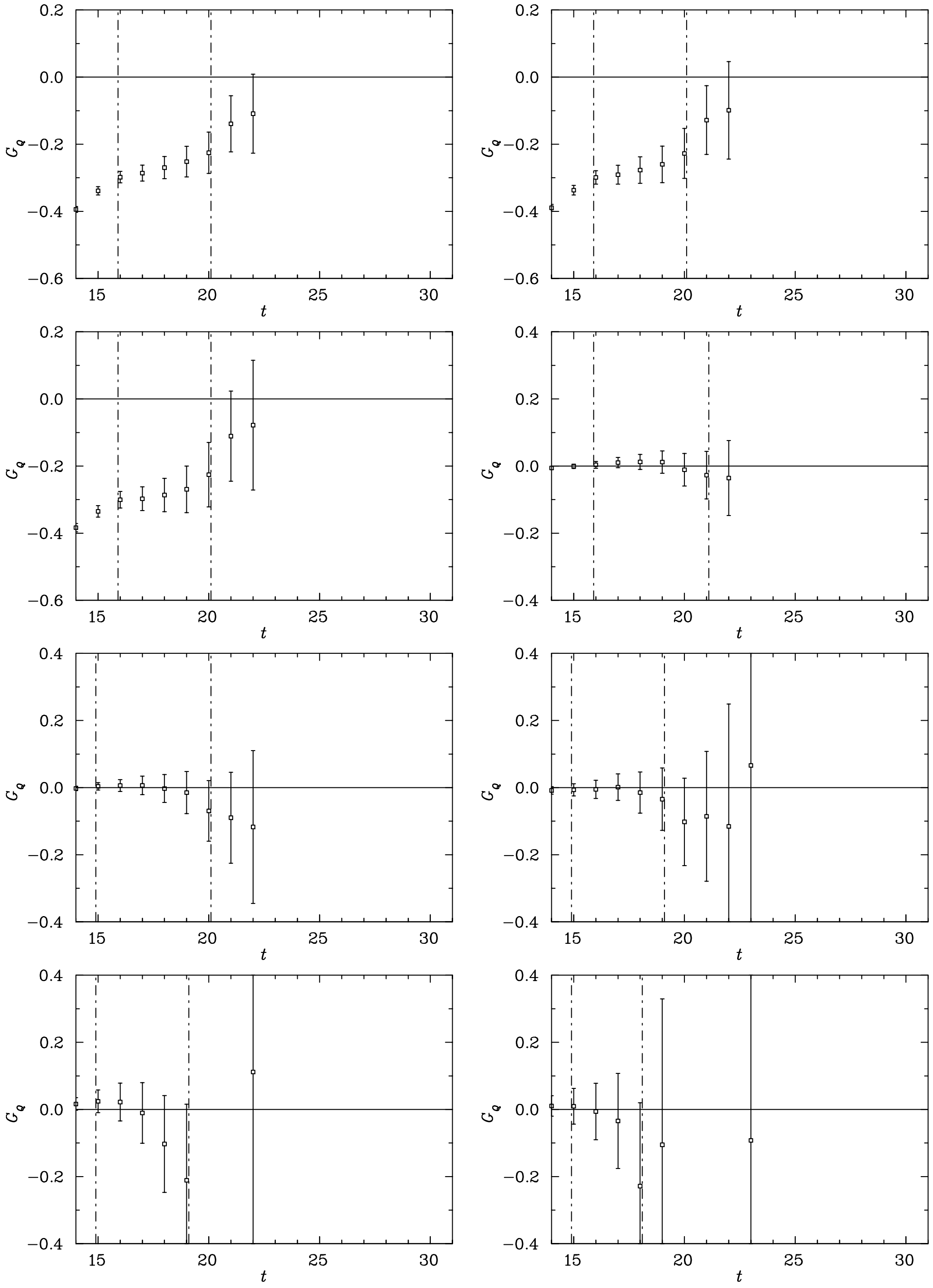

Fig. 5.11: As in Fig. 5.2 but for the up-quark contribution to ρ Quadrupole form factor.

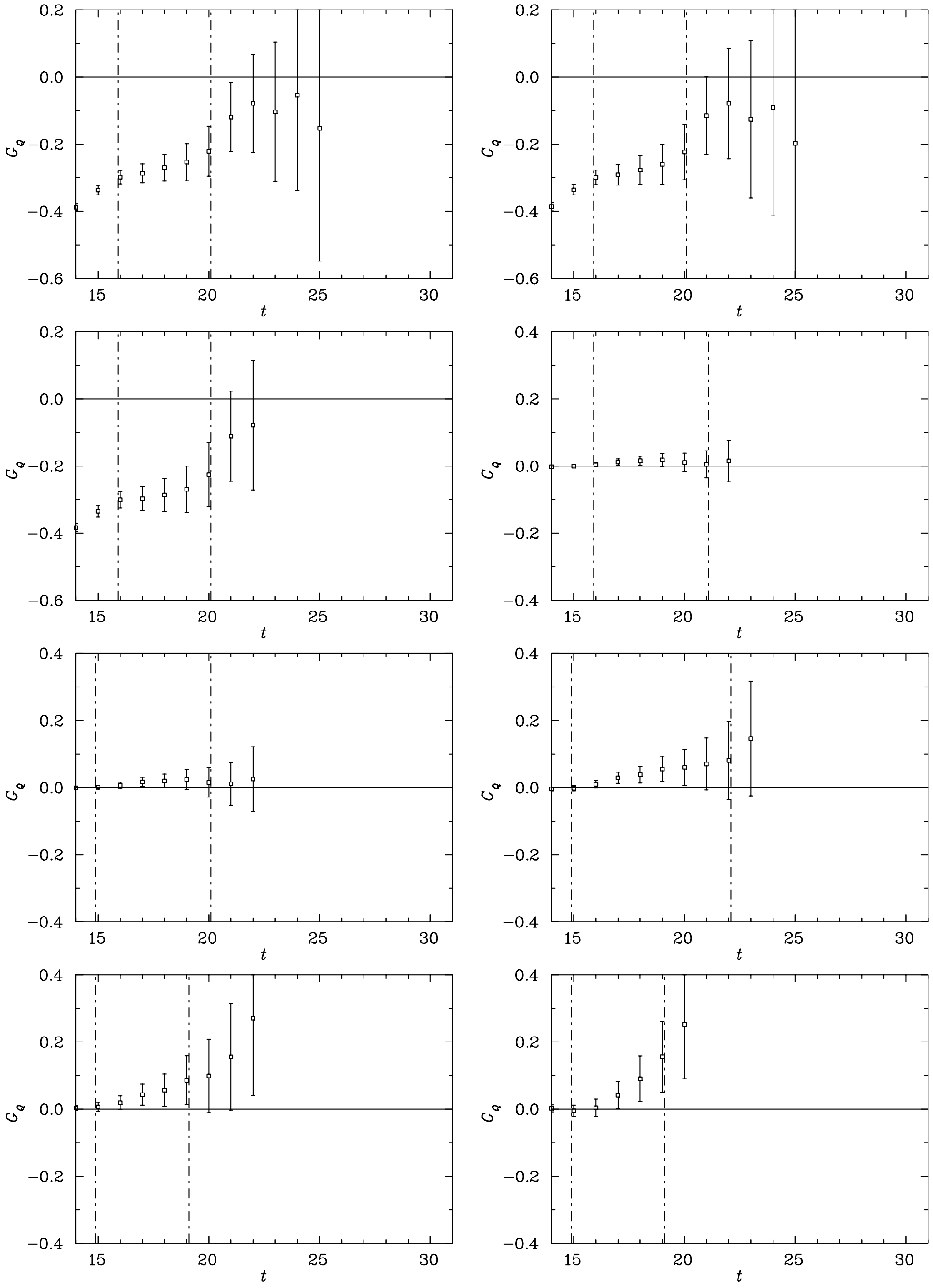

Fig. 5.12: As in Fig. 5.2 but for the up-quark contribution to K^* Quadrupole form factor.

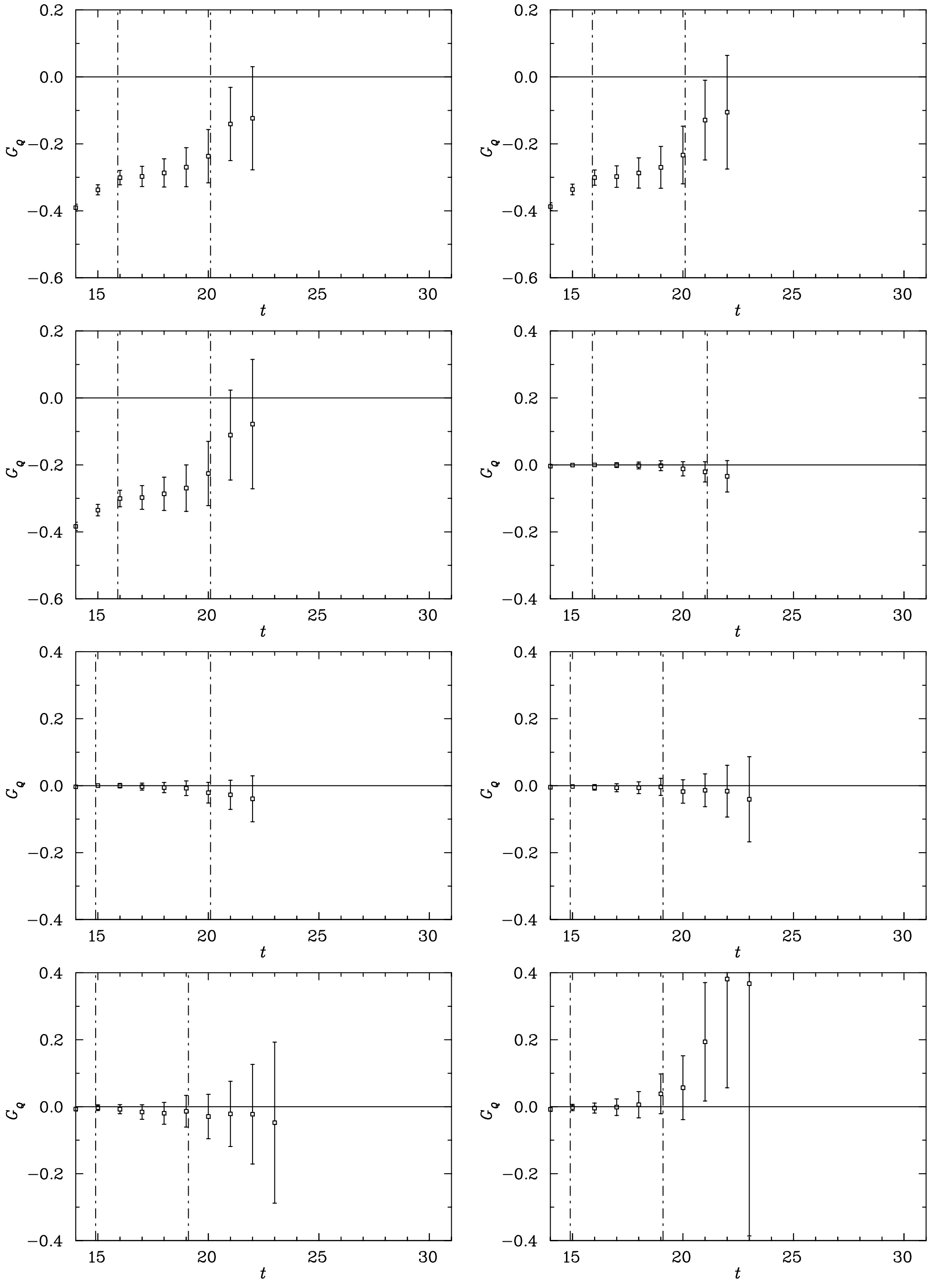

Fig. 5.13: As in Fig. 5.2 but for the strange-quark contribution to K^* Quadrupole form factor.

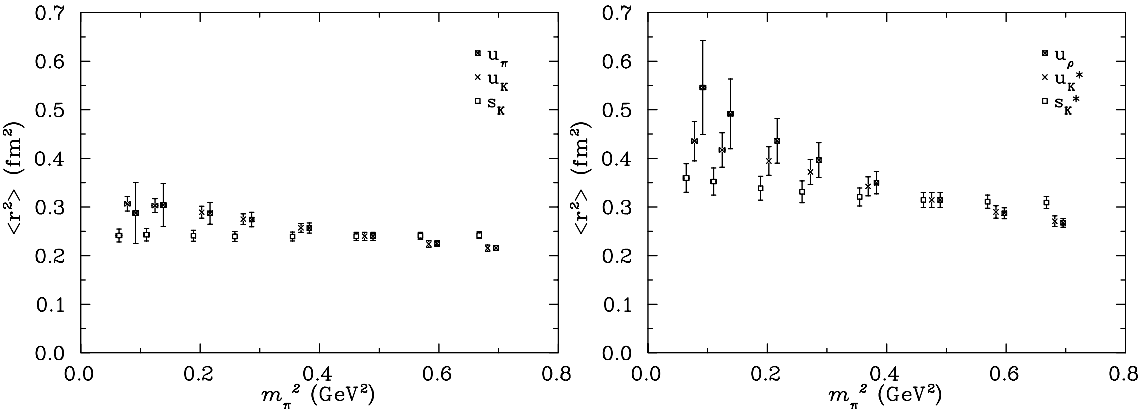

Fig. 5.14: Mean squared charge radius for each quark sector for pseudoscalar (left) and vector (right) cases. u_π and u_ρ symbols are centred on the relevant value of m_π^2, other symbols are offset for clarity.

Figure 5.14 shows the contributions to $\langle r^2 \rangle$ from each of the quark sectors examined in this study. It is clear that the ρ-meson has a much larger RMS charge radius than does the π. This behaviour is consistent with quark-model physics, where we would expect a hyperfine term proportional to $\frac{\vec{\sigma_1}\cdot\vec{\sigma_2}}{m_1 m_2}$. Such a term would be attractive for a π and repulsive for a ρ. Nevertheless, it is fascinating that the heavier particle is exhibiting the larger characteristic size, despite a smaller Compton wavelength. As we might expect, the $\langle r^2 \rangle$ values are smaller for the case of an up quark in the presence of a strange quark as the denominator of the hyperfine term is the product of the quark masses.

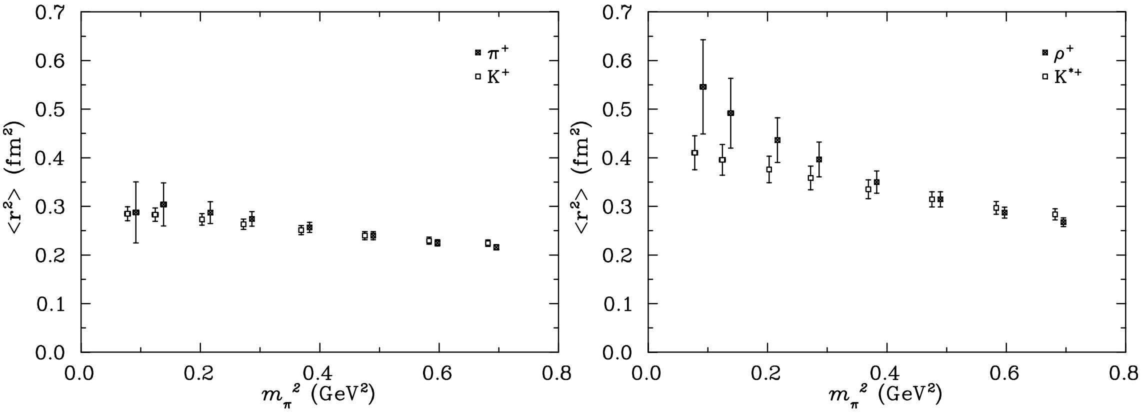

Fig. 5.15: Strange and non-strange meson mean squared charge radii for charged pseudoscalar (left) and vector (right) cases. Symbols are offset as in fig. 5.14

The strange neutral pseudoscalar and vector meson mean squared charge radii are shown in Figure 5.16. For the neutral strange mesons, we see a negative value for $\langle r^2 \rangle$, indicating that the negatively charged d-quark is lying further from the centre of mass on average than the $\bar{s}$. We should expect just such a behaviour for two reasons, both stemming from the fact that the $\bar{s}$ quark is considerably heavier than the d: the centre of mass must lie closer to the $\bar{s}$, and the d-quark will also have a larger Compton wavelength.

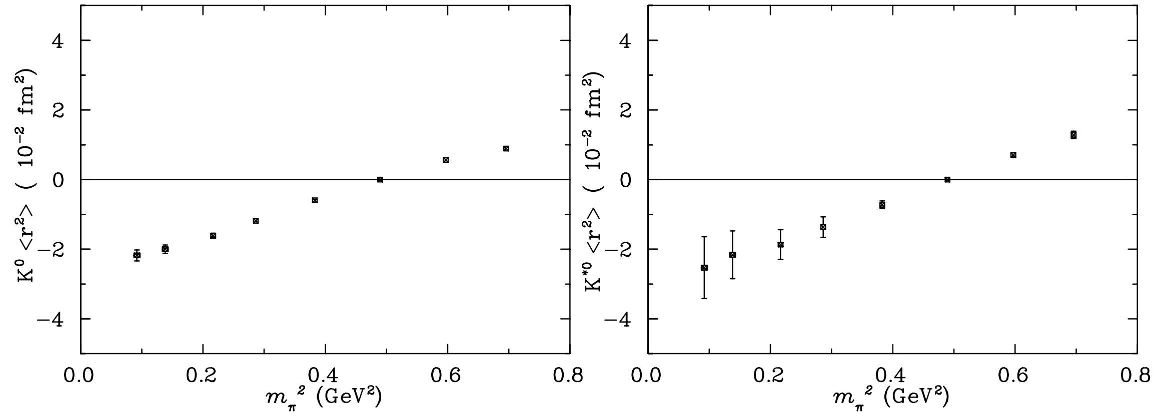

Fig. 5.16: Strange meson mean squared charge radii for neutral pseudoscalar (left) and vector (right) cases.

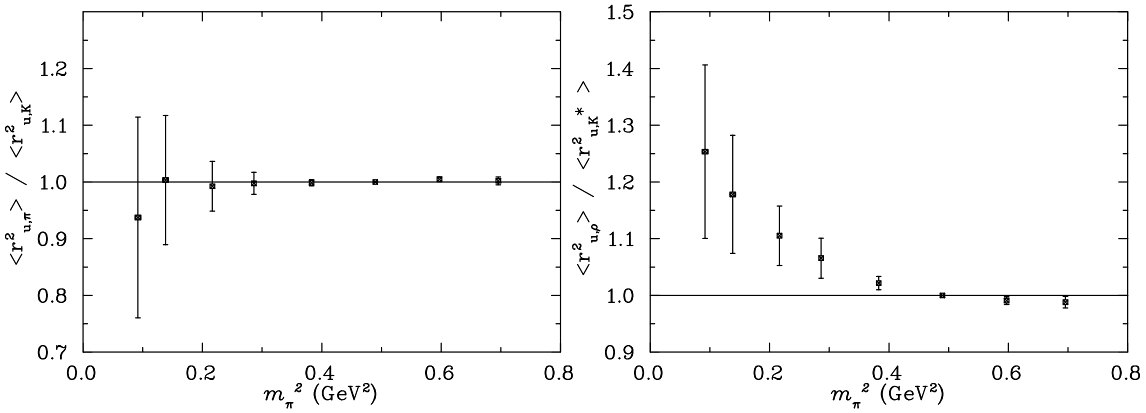

Fig. 5.17: Ratio of mean squared charge radius for a light quark in the environment of light and heavy quarks. Pseudoscalar (left) and vector (right) results are shown for comparison.

In Figure 5.17, we contrast the environment-dependence of the up-quark contributions to the pseudoscalar and vector mesons. The difference is striking: for the pseudoscalar case it could be argued that we see no environment-dependence at all, whereas in the vector case we see that the presence of a strange quark acts to heavily suppress the light charge distribution. This is the effect one predicts from a quark model, where hyperfine repulsion is reduced in the environment of an s-quark.

Figure 5.18 places our new results in some context. A previous study [18] has suggested that the π^+, ρ^+ and proton should have a very similar RMS charge radius at larger quark masses. In contrast to this, we find a significant splitting, most clearly present at heavier quark masses. It is possible that the agreement obtained in the previous study reflects finite-volume effects attendant with their combination of a small spatial volume.

Regarding the magnetic moment, we present Figures 5.19 and 5.20. At the SU(3) flavour limit, where we take the light quark flavours to have the same mass as the strange quark, quark model arguments suggest the magnetic moment for a ρ^+ should be -3 times the strange magnetic moment of the Λ (assuming no environmental dependence). The

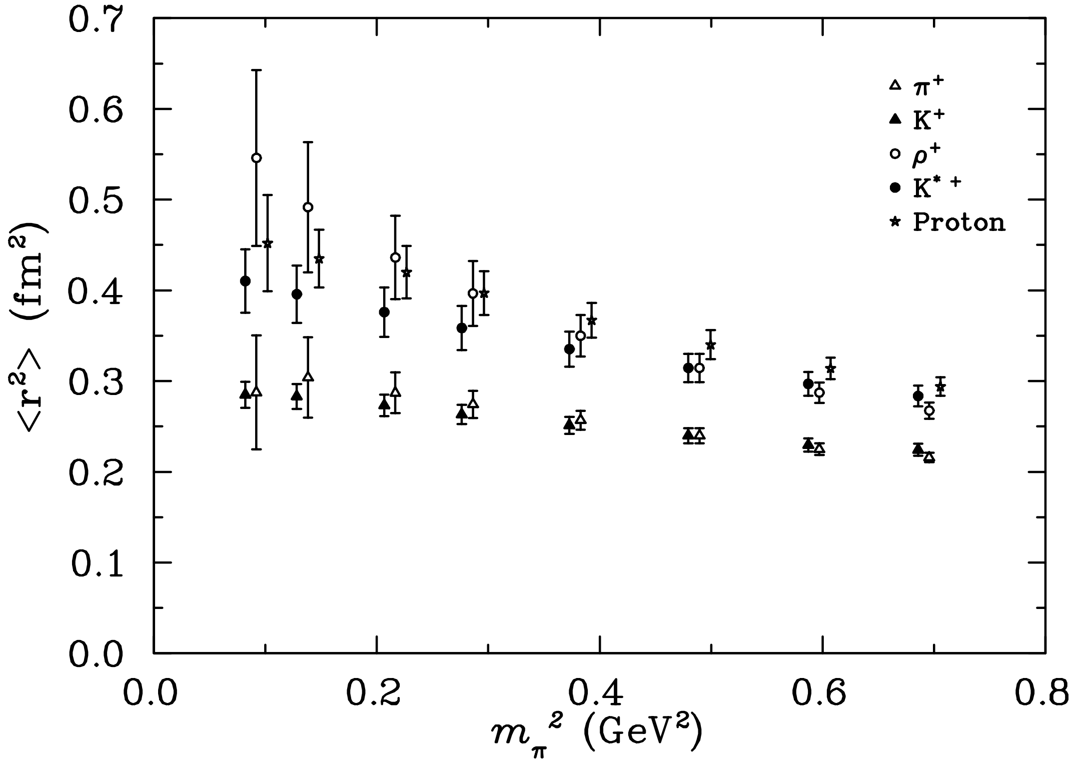

Fig. 5.18: Mean squared charge radii for positively charged baryons.

PDG [21] gives this figure as $-0.613\,\mu_N$, so we would naively expect a value of $1.84\,\mu_N$. The agreement displayed by the results is surprisingly good.

Figure 5.21 shows the ρ-meson g-factor g, essentially the ρ-meson magnetic moment in natural magnetons. Anderson *et al* [5] have argued that this quantity should be approximately 2 at large quark masses, which we do indeed observe. At light quark masses, however, we do see some evidence of chiral curvature, which would indicate that perhaps the linear chiral extrapolations of that paper should be treated with caution.

As the d-quark becomes lighter than the $\bar{s}$ in our calculations we see the magnetic moment exhibiting a very linear negative slope. The magnitude of the magnetic moment is quite small, but clearly differentiable from zero everywhere except at the SU(3) flavour limit where symmetry forces it to be exactly zero.

The magnetic moment of the vector meson, like the RMS charge radius, shows considerable environment dependence. The larger contribution of an up quark in a ρ relative to a K^* is consistent with what we have already observed with the RMS charge radius, as follows: since $\langle r^2 \rangle$ is larger for the up quark in a ρ meson than for the up quark in a K^*, the effective mass is reciprocally smaller for the up quark in a ρ. This smaller effective mass gives rise in turn to a larger magnetic moment. Figure 5.23 shows this pattern.

The Quadrupole form-factor, shown in Figure 5.24 on a per quark-sector basis and in Figure 5.25 for the ρ^+ and K^{*+} mesons, is observed to be categorically negative. The statistical fluctuations attendant to our finite ensemble hide any information that might

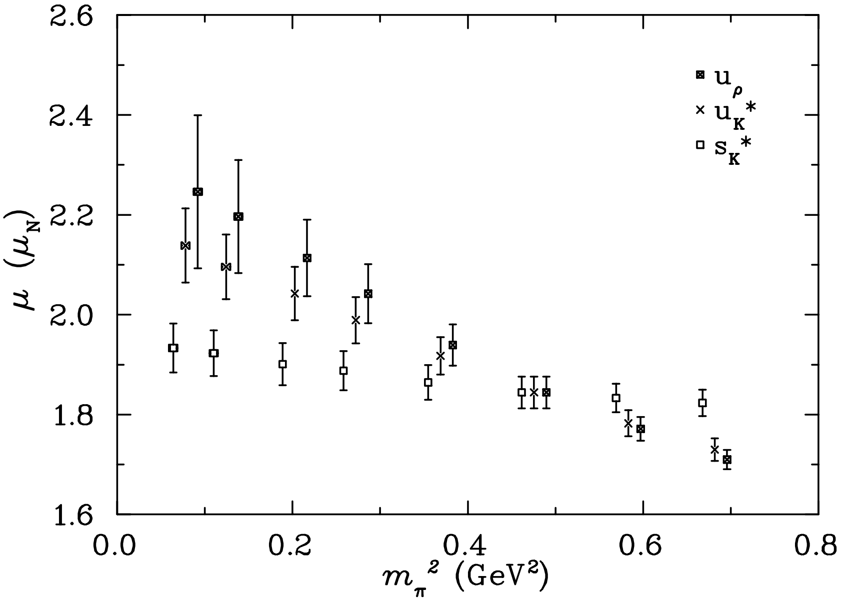

Fig. 5.19: Per quark-sector (left) and corresponding charged vector meson (right) magnetic moments.

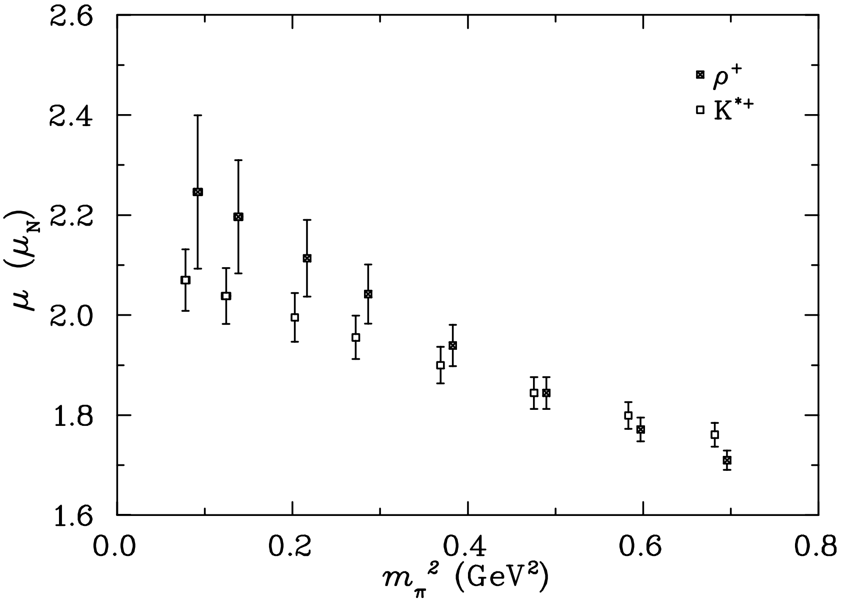

Fig. 5.20: Charged vector meson magnetic moments.

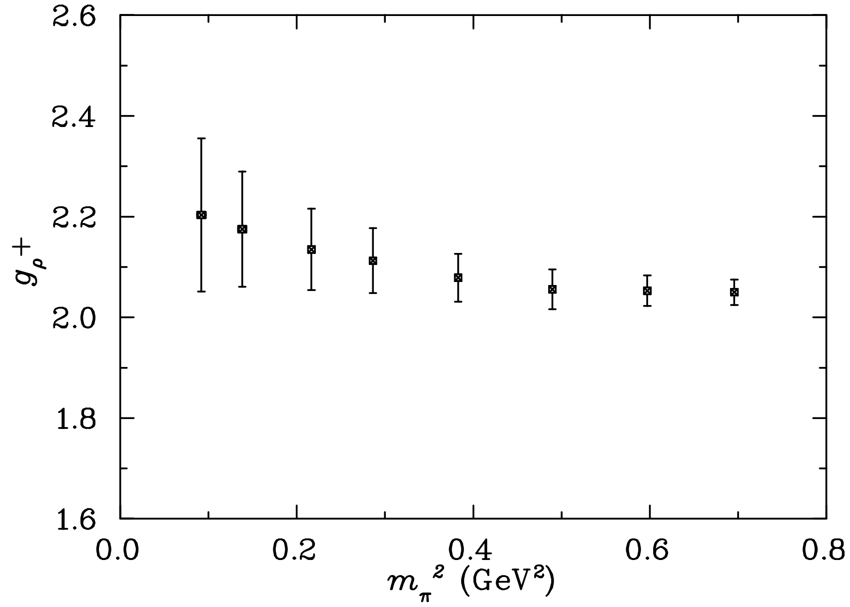

Fig. 5.21: g factor for ρ meson.

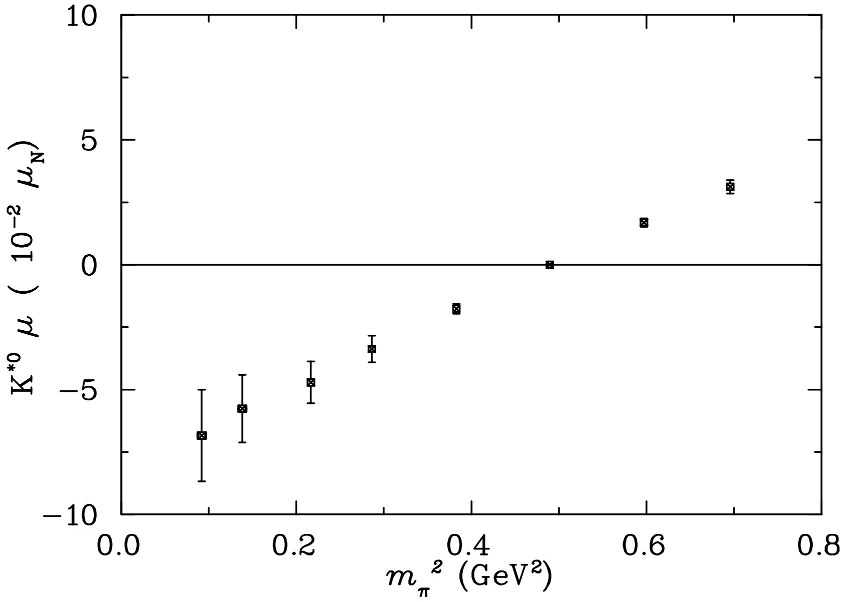

Fig. 5.22: Neutral K^*-meson magnetic moment.

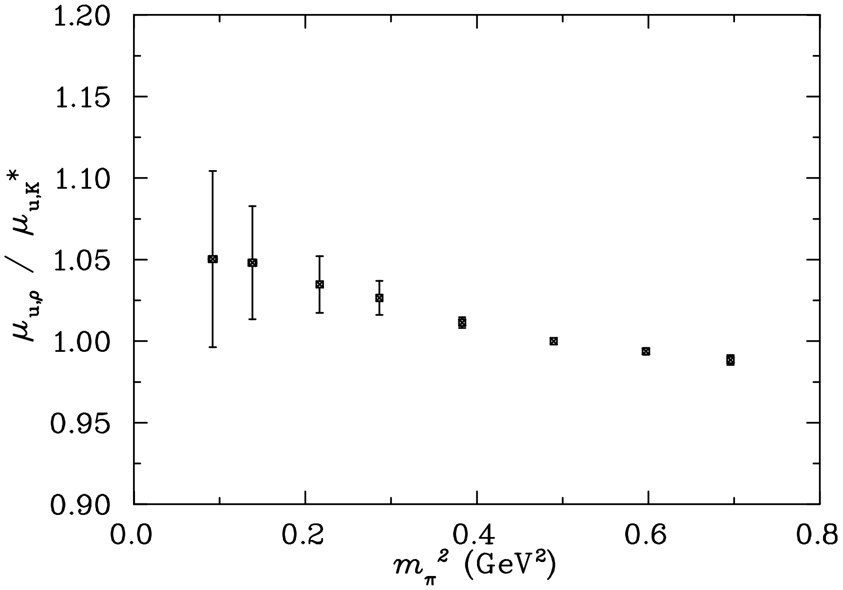

Fig. 5.23: Environment-dependence for light-quark contribution to vector meson magnetic moment.

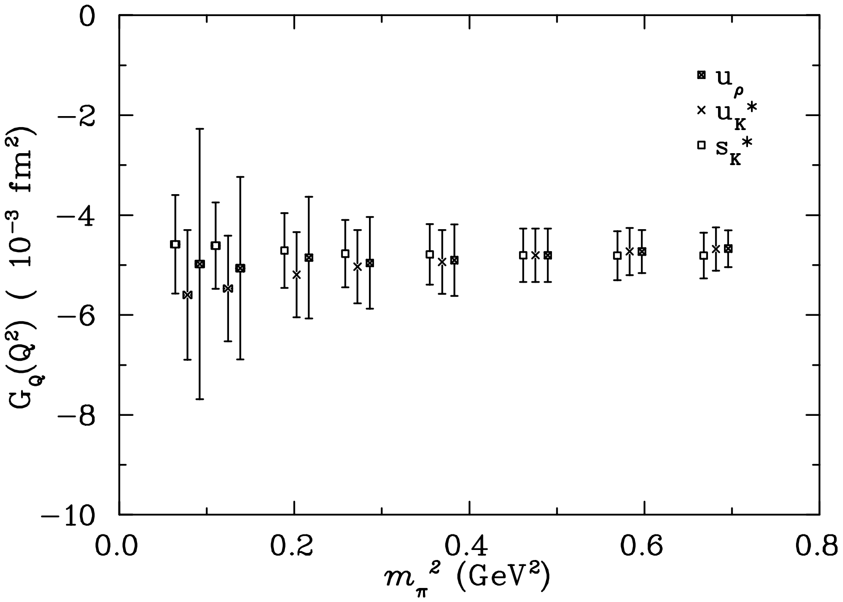

Fig. 5.24: Per quark-sector quadrupole form-factors.

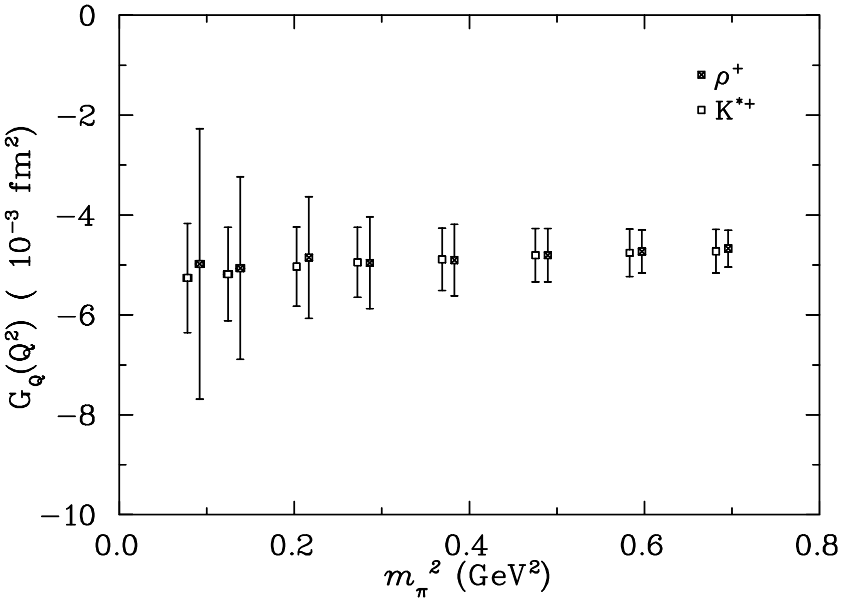

Fig. 5.25: Vector meson quadrupole form factors for ρ^+ and K^{*+}.

exist about a systematic dependence on quark mass, but the central values show no particular pattern as we vary this. A negative quadrupole moment corresponds to an oblate shape - one which is compressed along the spin axis. This coincides with the calculation of Alexandrou *e*t al. [3] who observed a negative quadrupole moment for spin ± 1 ρ-meson states in a density-density analysis. A simple quark model would predict a value of zero for this quantity, requiring an admixture of s- and d-wave-functions in order to admit such asymmetry. Importantly, the quadrupole form-factor is shown to be negative at heavy quark masses, indicating that the simplest of quark models is insufficient even in this regime.

Environmental sensitivity for the quadrupole form-factor (5.26) is masked to some degree by the amount of statistical uncertainty present in our results. Nevertheless, the central values show a downward trend at light quark masses. The mass-dependence plot shows that most of the contribution of the K^* deformation is due to the up quark.

At light quark masses we see a small positive quadrupole moment for the K^{*0} meson, but with little statistical significance. It would be very interesting to re-examine this with better statistics in order to more precisely determine the expected value at the very lightest quark masses.

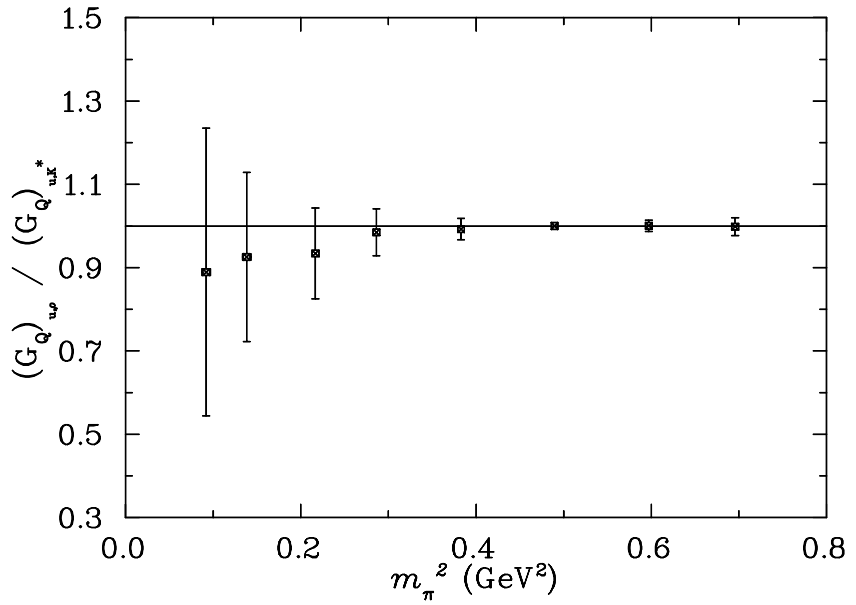

Fig. 5.26: Environment-dependence for light-quark contribution to vector meson quadrupole form-factor.

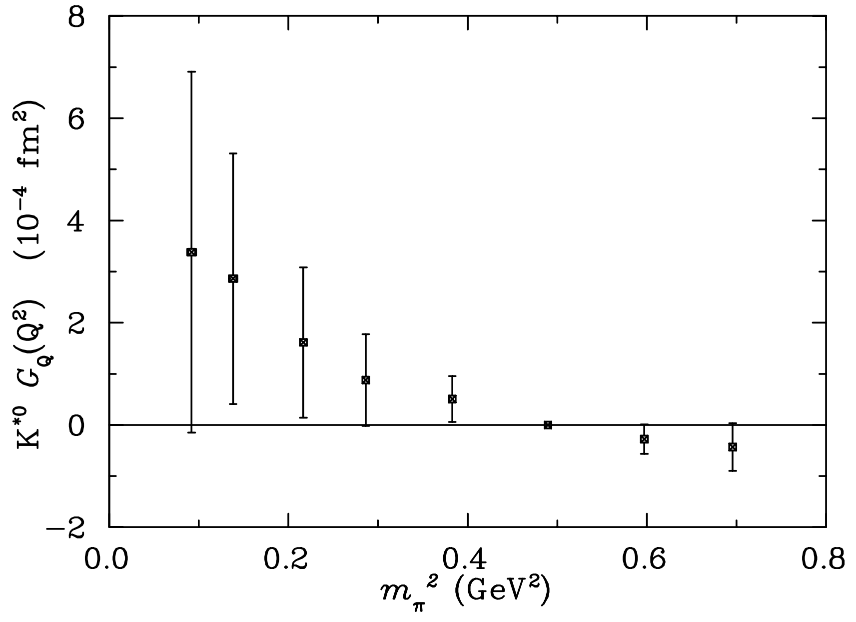

Fig. 5.27: Quadrupole form-factor for neutral K^* meson.

5.5 Conclusions

We have obtained the electric, magnetic, and quadrupole form-factors (and associated static quantities). Of particular interest is a firm prediction of a negative Quadrupole moment. The ratio of quadrupole moment to mean square charge radius is approximately $1:30$, so the deformation is small but not negligible. A larger ensemble of configurations would enable better control of statistical uncertainties and potentially enable some work in extrapolating these quantities, but this is beyond the scope of this thesis. Further work will encompass examining the form-factors of the a_1 meson, and the $\rho \rightarrow \pi\gamma$ electromagnetic decay, as well as a repeat of this work using dynamical (Full QCD) propagators.

6

Conclusions

We have completed a comprehensive analysis of mesons from Lattice QCD in the quenched approximation. Some striking results include:

- a first-ever first-principles calculation of all three of the vector meson form-factors, including the environment and mass-sensitivity of the quark contributions to each form-factor
- a high precision calculation of the pseudoscalar meson form-factor
- a potential reconciliation of the lattice and experimental results for the mass of the 1^{-+} exotic meson
- a determination that the optimal smearing prescription for local hybrid interpolating fields is different from what one might natively expect from a flux-tube picture
- a calculation of meson excited states
- a comprehensive survey of conventional and hybrid meson operators
- a determination that the ρ-meson is oblate, and not spherically symmetric as a naive quark model would predict. Importantly, this holds even at heavy quark masses.

It is hoped that the results of this work will be of assistance to physicists in constraining model parameters, especially as experimental values for the ρ-meson are difficult to come by due to the short lifetime of the particle. In particular, the result for the quadrupole may help constrain the amount of D-wave admixture in quark-model wave functions of the ρ, and the source-dependence results may result in more success obtaining precise calculations of the properties of the exotic mesons.

Scope for future work lies in addressing the two main limitations of this work, both imposed by the current state-of-the-art in computational power. These are the quenched approximation, whereby sea-quark loops are omitted, which becomes increasingly important at light quark-masses, and the finite size of our ensemble. By addressing the former we would greatly simplify the physical interpretation of our results, and by increasing our ensemble we would gain better control of statistical errors. In particular, a four-fold increase in statistics would afford us much greater insight into the environment dependence of the light-quark contributions to the vector meson electromagnetic form-factors.

Bibliography

[1] M. Albanese et al. Glueball masses and string tension in lattice qcd. *Phys. Lett.*, B192:163, 1987.

[2] D. Alde et al. Evidence for a 1-+ exotic meson. *Phys. Lett.*, B205:397, 1988.

[3] C. Alexandrou, P. de Forcrand, and A. Tsapalis. Probing hadron wave functions in lattice qcd. *Phys. Rev.*, D66:094503, 2002.

[4] C. R. Allton, W. Armour, D. B. Leinweber, A. W. Thomas, and R. D. Young. Chiral and continuum extrapolation of partially-quenched lattice results. *Phys. Lett.*, B628:125–130, 2005.

[5] William Andersen and Walter Wilcox. Lattice charge overlap. i. elastic limit of pi and rho mesons. *Annals Phys.*, 255:34–59, 1997.

[6] W. Armour, C. R. Allton, D. B. Leinweber, A. W. Thomas, and R. D. Young. Unified chiral analysis of the vector meson spectrum from lattice qcd. 2005.

[7] R. G. Arnold, Carl E. Carlson, and Franz Gross. Polarization transfer in elastic electron scattering from nucleons and deuterons. *Phys. Rev.*, C23:363, 1981.

[8] William A. Bardeen, A. Duncan, E. Eichten, Nathan Isgur, and H. Thacker. Chiral loops and ghost states in the quenched scalar propagator. *Phys. Rev.*, D65:014509, 2002.

[9] C. Bernard et al. Exotic hybrid mesons from improved kogut-susskind fermions. *Nucl. Phys. Proc. Suppl.*, 119:260–262, 2003.

[10] Claude W. Bernard et al. Exotic mesons in quenched lattice qcd. *Phys. Rev.*, D56:7039–7051, 1997.

[11] Sundance O. Bilson-Thompson, Derek B. Leinweber, and Anthony G. Williams. Highly-improved lattice field-strength tensor. *Ann. Phys.*, 304:1–21, 2003.

[12] Sharada Boinepalli, Waseem Kamleh, Derek B. Leinweber, Anthony G. Williams, and James M. Zanotti. Improved chiral properties of flic fermions. *Phys. Lett.*, B616:196–202, 2005.

[13] Frederic D. R. Bonnet, Derek B. Leinweber, and Anthony G. Williams. General algorithm for improved lattice actions on parallel computing architectures. *J. Comput. Phys.*, 170:1–17, 2001.

[14] Frederic D. R. Bonnet, Derek B. Leinweber, Anthony G. Williams, and James M. Zanotti. Improved smoothing algorithms for lattice gauge theory. *Phys. Rev.*, D65:114510, 2002.

[15] Stanley J. Brodsky and John R. Hiller. Universal properties of the electromagnetic interactions of spin one systems. *Phys. Rev.*, D46:2141–2149, 1992.

[16] N. Cabibbo and E. Marinari. A new method for updating su(n) matrices in computer simulations of gauge theories. *Phys. Lett.*, B119:387–390, 1982.

[17] S. U. Chung et al. Evidence for exotic j(pc) = 1-+ meson production in the reaction pi- p -> eta pi- p at 18-gev/c. *Phys. Rev.*, D60:092001, 1999.

[18] T. Draper, R. M. Woloshyn, and Keh-Fei Liu. Electromagnetic properties of nucleons from lattice qcd. *Phys. Lett.*, B234:121–126, 1990.

[19] T. Draper, R. M. Woloshyn, Walter Wilcox, and Keh-Fei Liu. Electromagnetic form-factors of hadrons. *Nucl. Phys. Proc. Suppl.*, 9:175–180, 1989.

[20] A. R. Dzierba, R. Mitchell, A. P. Szczepaniak, M. Swat, and S. Teige. A search for j(pc) = 1-+ exotic mesons in the pi- pi- pi+ and pi- pi0 pi0 systems. 2005.

[21] S. Eidelman et al. Review of particle physics. *Phys. Lett.*, B592:1, 2004.

[22] M. Falcioni, M. L. Paciello, G. Parisi, and B. Taglienti. Again on su(3) glueball mass. *Nucl. Phys.*, B251:624–632, 1985.

[23] Brian J. Gough, George M. Hockney, Aida X. El-Khadra, Andreas S. Kronfeld, Paul B. Mackenzie, Bart P. Mertens, Tetsuya Onogi, and James N. Simone. The light quark masses from lattice gauge theory. *Phys. Rev. Lett.*, 79(9):1622–1625, Sep 1997.

[24] S. Gusken. A study of smearing techniques for hadron correlation functions. *Nucl. Phys. Proc. Suppl.*, 17:361–364, 1990.

[25] A. Holl, A. Krassnigg, P. Maris, C. D. Roberts, and S. V. Wright. Electromagnetic properties of ground and excited state pseudoscalar mesons. *Phys. Rev.*, C71:065204, 2005.

[26] B. L. Ioffe and A. V. Smilga. Meson widths and form-factors at intermediate momentum transfer in nonperturbative qcd. *Nucl. Phys.*, B216:373, 1983.

[27] W. Kamleh, D. B. Leinweber, and A. G. Williams. Dynamical flic fermions. *Nucl. Phys. Proc. Suppl.*, 129:826–828, 2004.

[28] Waseem Kamleh, Derek B. Leinweber, and Anthony G. Williams. Hybrid monte carlo with fat link fermion actions. *Phys. Rev.*, D70:014502, 2004.

[29] P. Lacock, C. Michael, P. Boyle, and P. Rowland. Orbitally excited and hybrid mesons from the lattice. *Phys. Rev.*, D54:6997–7009, 1996.

[30] P. Lacock and K. Schilling. Hybrid and orbitally excited mesons in full qcd. *Nucl. Phys. Proc. Suppl.*, 73:261–263, 1999.

[31] D. B. Leinweber et al. Flic fermions and hadron phenomenology. 2002.

[32] D. B. Leinweber et al. Precise determination of the strangeness magnetic moment of the nucleon. *Phys. Rev. Lett.*, 94:212001, 2005.

[33] D. B. Leinweber et al. Systematic uncertainties in the precise determination of the strangeness magnetic moment of the nucleon. *Nucl. Phys. Proc. Suppl.*, 141:287–294, 2005.

[34] Derek B. Leinweber and Thomas D. Cohen. Unquenching the rho meson. *Phys. Rev.*, D49:3512–3518, 1994.

[35] Derek B. Leinweber, Anthony G. Williams, Jian-bo Zhang, and Frank X. Lee. Topological charge barrier in the markov-chain of qcd. *Phys. Lett.*, B585:187–191, 2004.

[36] J. Litt et al. Measurement of the ratio of the proton form-factors, g(e) / g(m), at high momentum transfers and the question of scaling. *Phys. Lett.*, B31:40–44, 1970.

[37] M. Lu et al. Exotic meson decay to omega pi0 pi-. *Phys. Rev. Lett.*, 94:032002, 2005.

[38] M. Luscher and P. Weisz. On-shell improved lattice gauge theories. *Commun. Math. Phys.*, 97:59, 1985.

[39] G. Martinelli, Christopher T. Sachrajda, and A. Vladikas. A study of 'improvement' in lattice qcd. *Nucl. Phys.*, B358:212–230, 1991.

[40] Craig McNeile and Chris Michael. Mixing of scalar glueballs and flavour-singlet scalar mesons. *Phys. Rev.*, D63:114503, 2001.

[41] Zhong-Hao Mei and Xiang-Qian Luo. Exotic mesons from quantum chromodynamics with improved gluon and quark actions on the anisotropic lattice. *Int. J. Mod. PHys.*, A18:5713, 2003.

[42] C. Michael. Hybrid mesons from the lattice. 2003.

[43] Yu. D. Prokoshkin and S. A. Sadovsky. Analysis of d wave in pi- p → a2(0) (1320) n reaction. *Phys. Atom. Nucl.*, 58:606–612, 1995.

[44] Stephen R. Sharpe. Quenched chiral logarithms. *Phys. Rev.*, D46:3146–3168, 1992.

[45] Anthony W. Thomas and Adam P. Szczepaniak. Chiral extrapolations and exotic meson spectrum. *Phys. Lett.*, B526:72–78, 2002.

[46] S. F. Tuan, T. Ferbel, and R. H. Dalitz. Comments on evidence for a 1-+ exotic meson. *Phys. Lett.*, B213:537, 1988.

[47] Kenneth G. Wilson. Confinement of quarks. *Phys. Rev.*, D10:2445–2459, 1974.

[48] Matthew Wingate, Thomas A. DeGrand, Sara Collins, and Urs M. Heller. Properties of the a1 meson from lattice qcd. *Phys. Rev. Lett.*, 74:4596–4598, 1995.

[49] R. D. Young, D. B. Leinweber, and A. W. Thomas. Leading quenching effects in the proton magnetic moment. *Phys. Rev.*, D71:014001, 2005.

[50] R. D. Young, D. B. Leinweber, Anthony W. Thomas, and S. V. Wright. Chiral analysis of quenched baryon masses. *Phys. Rev.*, D66:094507, 2002.

[51] J. M. Zanotti et al. Novel fat-link fermion actions. *Nucl. Phys. Proc. Suppl.*, 109A:101–105, 2002.

[52] J. M. Zanotti et al. Spin-3/2 nucleon and delta baryons in lattice qcd. *Phys. Rev.*, D68:054506, 2003.

[53] J. M. Zanotti, B. Lasscock, D. B. Leinweber, and A. G. Williams. Scaling of flic fermions. *Phys. Rev.*, D71:034510, 2005.

[54] James M. Zanotti et al. Hadron masses from novel fat-link fermion actions. *Phys. Rev.*, D65:074507, 2002.

A

Data pertaining to the calculation of meson effective masses

These results were generated on a lattice of spacing $0.128\,\mathrm{fm}$. The conversion factor from dimensionless masses to GeV is thus $0.1973\mathrm{GeVfm}/0.128\mathrm{fm} = 1.5414\mathrm{GeV}$. We shall use the symbol s to refer to our ‘strange’ (heavy) quark. The relationship between κ values and pion masses is given in Table A.1.

Table A.1: κ values, and corresponding pion masses (and uncertainties) in GeV.

i_κ	κ	m_π
1	0.12780	0.8356(14)
2	0.12830	0.7744(15)
3	0.12885	0.7012(15)
4	0.12940	0.6201(15)
5	0.12990	0.5354(16)
6	0.13025	0.4660(20)
7	0.13060	0.3732(79)
8	0.13080	0.3076(63)

Table A.2: a_0 scalar meson mass fits. Column headings are in order, the $kappa$ number, the lower and upper bounds of the fit window, the mass, error and χ^2 from our analysis.

i_κ	t_{start}	t_{end}	Ma	σ	$\chi^2/\text{d.o.f}$
1	9	11	0.942468	0.008561	0.569828
2	9	11	0.927582	0.010346	0.550105
3	9	11	0.918652	0.013697	0.624862
4	9	11	0.928701	0.020547	0.989549

Table A.3: As in Table A.2, but for the $K_0^\star$.

i_κ	t_{start}	t_{end}	Ma	σ	$\chi^2/\text{d.o.f}$
1	9	11	0.928457	0.010659	0.580351
2	9	11	0.922306	0.011843	0.579739
3	9	11	0.918652	0.013697	0.624862
4	9	11	0.921341	0.016632	0.785677

Table A.4: As in Table A.2 but for conventional π meson operator $\bar{q}\gamma_5 q$.

i_κ	t_{start}	t_{end}	Ma	σ	$\chi^2/\text{d.o.f}$
1	16	26	0.542076	0.000933	1.050107
2	16	26	0.502415	0.000966	1.066433
3	16	26	0.454885	0.000991	0.850827
4	16	26	0.402287	0.001030	0.735460
5	16	26	0.347436	0.001105	0.781297
6	16	26	0.302289	0.001287	0.943519
7	16	26	0.242118	0.005106	0.963553
8	16	26	0.199537	0.004086	0.974327

Table A.5: As in Table A.2 but for conventional K meson operator $\bar{s}\gamma_5 q$.

i_κ	$t_{\rm start}$	$t_{\rm end}$	Ma	σ	$\chi^2/{\rm d.o.f}$
1	16	26	0.500447	0.000975	1.073315
2	16	26	0.479317	0.000983	0.990409
3	16	26	0.454885	0.000991	0.850827
4	16	26	0.429533	0.001014	0.810890
5	16	26	0.405371	0.001059	0.837823
6	16	26	0.387684	0.001123	0.923336
7	16	26	0.368507	0.001670	0.888473
8	16	26	0.358399	0.001425	1.156427

Table A.6: As in Table A.2 but for axial-vector pion interpolator $\bar{q}\gamma_5\gamma_4 q$.

i_κ	$t_{\rm start}$	$t_{\rm end}$	Ma	σ	$\chi^2/{\rm d.o.f}$
1	11	20	0.540293	0.001238	0.598628
2	11	20	0.500503	0.001278	0.521659
3	11	20	0.453187	0.001334	0.471202
4	11	20	0.400662	0.001405	0.468622
5	11	20	0.345862	0.001506	0.525954
6	11	20	0.300941	0.001632	0.542129
7	11	20	0.247653	0.002655	0.754260
8	11	20	0.207590	0.004310	0.978518

Table A.7: As in Table A.2 but for axial-vector K interpolator $\bar{s}\gamma_5\gamma_4 q$

i_κ	$t_{\rm start}$	$t_{\rm end}$	Ma	σ	$\chi^2/{\rm d.o.f}$
1	11	20	0.498332	0.001292	0.522991
2	11	20	0.477352	0.001308	0.492776
3	11	20	0.453187	0.001334	0.471202
4	11	20	0.427686	0.001372	0.464957
5	11	20	0.403065	0.001430	0.474499
6	11	20	0.384818	0.001499	0.451416
7	11	20	0.365499	0.001662	0.418255
8	11	20	0.354341	0.001804	0.328788

Table A.8: As in Table A.2 but for hybrid pion interpolating field $i\bar{q}^a\gamma_j B_j^{ab} q^b$.

i_κ	t_{start}	t_{end}	Ma	σ	$\chi^2/\text{d.o.f}$
1	14	20	0.540098	0.007257	0.977018
2	14	20	0.499982	0.007463	0.920785
3	14	20	0.452610	0.007801	0.852279
4	14	20	0.400714	0.008351	0.809458
5	14	20	0.346413	0.009261	0.842781
6	14	20	0.301686	0.010280	1.010559
7	14	20	0.248318	0.011460	1.252199
8	14	20	0.194288	0.020123	0.667699

Table A.9: As in Table A.2 but for hybrid K interpolating field $i\bar{s}^a\gamma_j B_j^{ab} q^b$.

i_κ	t_{start}	t_{end}	Ma	σ	$\chi^2/\text{d.o.f}$
1	14	20	0.497599	0.007541	0.923259
2	14	20	0.476691	0.007634	0.888033
3	14	20	0.452610	0.007801	0.852279
4	14	20	0.427266	0.008067	0.828729
5	14	20	0.402446	0.008470	0.833725
6	14	20	0.383880	0.008929	0.904069
7	14	20	0.363574	0.009673	1.061964
8	14	20	0.352858	0.010477	1.067675

Table A.10: As in Table A.2 but for hybrid pion interpolating field $i\bar{q}^a\gamma_j\gamma_4B_j^{ab}q^b$.

i_κ	$t_{\rm start}$	$t_{\rm end}$	Ma	σ	$\chi^2/{\rm d.o.f}$
1	12	26	0.545971	0.002851	0.832075
2	12	26	0.506394	0.002804	0.742263
3	12	26	0.458760	0.002777	0.656149
4	12	26	0.405994	0.002895	0.598155
5	12	26	0.350475	0.003298	0.533417
6	12	26	0.304385	0.003804	0.606792
7	12	26	0.249358	0.004178	1.360696
8	12	26	0.208625	0.006253	1.052875

Table A.11: As in Table A.2 but for hybrid K interpolating field $i\bar{s}^a\gamma_j\gamma_4B_j^{ab}q^b$.

i_κ	$t_{\rm start}$	$t_{\rm end}$	Ma	σ	$\chi^2/{\rm d.o.f}$
1	12	30	0.507508	0.002329	1.103564
2	12	30	0.486136	0.002295	1.053223
3	12	30	0.461294	0.002267	0.984236
4	12	30	0.435686	0.002312	0.937038
5	12	30	0.411526	0.002464	0.941930
6	12	30	0.393909	0.002702	0.972512
7	12	30	0.375299	0.003155	0.957629
8	12	30	0.364972	0.003837	0.946693

Table A.12: As in Table A.2 but for conventional ρ-meson interpolating field $\bar{q}\gamma_jq$ for equal (left) and unequal (right) input quark masses.

i_κ	$t_{\rm start}$	$t_{\rm end}$	Ma	σ	$\chi^2/{\rm d.o.f}$
1	16	22	0.727977	0.003081	1.430645
2	16	22	0.703885	0.003569	1.443563
3	16	22	0.677396	0.004380	1.419843
4	16	22	0.651460	0.005776	1.376014
5	16	22	0.628950	0.008230	1.270934
6	16	22	0.613760	0.011680	1.056854
7	16	22	0.600671	0.019740	0.371343
8	16	22	0.610257	0.033558	0.314031

Table A.13: As in Table A.2 but for conventional K^*-meson interpolating field $\bar{s}\gamma_j q$.

i_κ	$t_{\rm start}$	$t_{\rm end}$	Ma	σ	$\chi^2/{\rm d.o.f}$
1	16	21	0.702220	0.003712	1.226565
2	16	21	0.690099	0.004005	1.165699
3	16	21	0.676832	0.004436	1.087662
4	16	21	0.663954	0.005059	1.028479
5	16	21	0.652908	0.005924	0.993326
6	16	21	0.645702	0.006864	0.995203
7	16	21	0.638674	0.008543	0.980531
8	16	21	0.639873	0.010192	0.541121

Table A.14: As in Table A.2 but for conventional ρ-meson interpolating field $\bar{q}\gamma_j\gamma_4 q$.

i_κ	$t_{\rm start}$	$t_{\rm end}$	Ma	σ	$\chi^2/{\rm d.o.f}$
1	14	19	0.730291	0.003023	1.277665
2	14	19	0.706060	0.003362	1.222823
3	14	19	0.679365	0.003920	1.144671
4	14	19	0.652795	0.004849	1.027337
5	14	19	0.629165	0.006514	0.842173
6	14	19	0.611177	0.008703	0.750687
7	14	19	0.591406	0.013972	1.174988
8	14	19	0.571187	0.025088	0.980223

Table A.15: As in Table A.2 but for conventional K^*-meson interpolating field $\bar{q}\gamma_j\gamma_4 q$.

i_κ	$t_{\rm start}$	$t_{\rm end}$	Ma	σ	$\chi^2/{\rm d.o.f}$
1	14	19	0.705001	0.003419	1.212617
2	14	19	0.692769	0.003622	1.186451
3	14	19	0.679365	0.003920	1.144671
4	14	19	0.666161	0.004340	1.093618
5	14	19	0.654555	0.004935	1.025103
6	14	19	0.646385	0.005571	0.977872
7	14	19	0.638678	0.006803	0.940564
8	14	19	0.636179	0.008225	0.602243

Table A.16: As in Table A.2 but for Hybrid ρ-meson interpolator $\bar{q}E_jq$. Error bars are larger than signal for lightest quark mass, so this line is omitted

i_κ	t_{start}	t_{end}	Ma	σ	$\chi^2/\text{d.o.f}$
1	12	19	0.742066	0.031162	1.236414
2	12	19	0.728289	0.038336	1.217807
3	12	19	0.721750	0.051659	1.125934
4	12	19	0.727662	0.076253	0.949960
5	12	19	0.716127	0.117422	0.887201
6	12	19	0.739333	0.182135	0.179079
7	12	19	0.563291	0.256713	1.428986

Table A.17: As in Table A.2 but for Hybrid K^*-meson interpolator $\bar{q}E_jq$. Error bars are larger than signal for 3 lightest quark masses.

i_κ	t_{start}	t_{end}	Ma	σ	$\chi^2/\text{d.o.f}$
1	15	19	0.664570	0.079990	0.951697
2	15	19	0.650558	0.096416	0.952065
3	15	19	0.632943	0.126131	0.902783
4	15	19	0.606679	0.184527	0.773465
5	15	19	0.540478	0.326554	0.553247

Table A.18: As in Table A.2 but for Hybrid ρ-meson interpolator $i\bar{q}^a\gamma_5 B_j^{ab}q^b$.

i_κ	t_{start}	t_{end}	Ma	σ	$\chi^2/\text{d.o.f}$
1	12	22	0.755673	0.019271	1.379385
2	12	22	0.728676	0.021446	1.381606
3	12	22	0.698463	0.024823	1.310405
4	12	22	0.667503	0.030086	1.159886
5	12	20	0.638159	0.037711	1.267486
6	12	22	0.620516	0.049515	1.293002
7	12	22	0.599346	0.092423	1.242542
8	12	22	0.482873	0.166664	1.150640

Table A.19: As in Table A.2 but for Hybrid K^*-meson interpolator $i\bar{q}^a\gamma_5 B_j^{ab} q^b$.

i_κ	t_{start}	t_{end}	Ma	σ	$\chi^2/\text{d.o.f}$
1	12	16	0.727823	0.026971	1.856496
2	12	16	0.714623	0.027849	1.823662
3	12	16	0.700190	0.029151	1.767746
4	12	16	0.685916	0.031003	1.695327
5	12	16	0.673457	0.033508	1.583995
6	12	16	0.667761	0.036388	1.480800
7	12	16	0.666913	0.041800	1.304392
8	12	16	0.670980	0.048906	1.033869

Table A.20: As in Table A.2 but for Hybrid ρ-meson interpolator $i\bar{q}^a\gamma_4\gamma_5 B_j^{ab} q^b$.

i_κ	t_{start}	t_{end}	Ma	σ	$\chi^2/\text{d.o.f}$
1	12	19	0.748734	0.018952	1.161976
2	12	19	0.725957	0.021154	1.054827
3	12	19	0.702988	0.024949	0.868723
4	12	19	0.683667	0.031311	0.650179
5	12	19	0.670175	0.040881	0.477861
6	12	19	0.665139	0.051335	0.381633
7	12	19	0.663100	0.067830	0.322528
8	12	19	0.645117	0.092296	0.616030

Table A.21: As in Table A.2 but for Hybrid K-meson interpolator $i\bar{q}^a\gamma_4\gamma_5 B_j^{ab} q^b$.

i_κ	t_{start}	t_{end}	Ma	σ	$\chi^2/\text{d.o.f}$
1	12	22	0.728549	0.020418	0.762931
2	12	22	0.717493	0.021863	0.709354
3	12	22	0.705967	0.023989	0.637575
4	12	22	0.695830	0.026968	0.567746
5	12	22	0.688051	0.030813	0.514944
6	12	22	0.684327	0.034726	0.487495
7	12	22	0.680818	0.039806	0.551833
8	12	22	0.678415	0.044186	0.566844

Table A.22: As in Table A.2 but for pseudovector interpolating field $\bar{q}\gamma_5\gamma_4\gamma_j q$ with equal quark-antiquark masses.

i_κ	$t_{\rm start}$	$t_{\rm end}$	Ma	σ	$\chi^2/{\rm d.o.f}$
1	11	16	1.032468	0.008605	0.655486
2	11	16	1.012554	0.009433	0.636995
3	11	16	0.991178	0.010702	0.668774
4	11	16	0.970774	0.012717	0.756178
5	11	16	0.954319	0.016296	0.860163
6	11	16	0.943740	0.021157	1.035939
7	11	16	0.944531	0.036163	1.114880
8	11	16	0.964143	0.067878	0.832436

Table A.23: As in Table A.2 but for pseudovector interpolating field $\bar{q}\gamma_5\gamma_4\gamma_j q$ with unequal quark-antiquark masses.

i_κ	$t_{\rm start}$	$t_{\rm end}$	Ma	σ	$\chi^2/{\rm d.o.f}$
1	11	17	1.012299	0.009573	0.761536
2	11	17	1.002074	0.010059	0.760418
3	11	17	0.991242	0.010736	0.771770
4	11	17	0.981190	0.011679	0.799178
5	11	17	0.973582	0.013056	0.842819
6	11	17	0.969448	0.014549	0.908081
7	11	17	0.970464	0.018018	0.951555
8	11	17	0.979468	0.023043	0.983875

Table A.24: As in Table A.2 but for axial-vector interpolating field $\bar{q}\gamma_5\gamma_i q$ for equal quark-antiquark masses. No appropriate fit window exists for the two lightest quark-masses.

i_κ	$t_{\rm start}$	$t_{\rm end}$	Ma	σ	$\chi^2/{\rm d.o.f}$
1	11	15	1.024361	0.007554	1.324197
2	11	15	1.005865	0.008140	1.322558
3	11	15	0.986890	0.009012	1.376443
4	11	15	0.970093	0.010275	1.431509
5	11	15	0.957989	0.012059	1.447858
6	11	15	0.953572	0.014024	1.486133

Table A.25: As in Table A.2 but for axial-vector interpolating field $\bar{q}\gamma_5\gamma_i q$ for unequal quark-antiquark masses. No appropriate fit window exists for the two lightest quark-masses.

i_κ	$t_{\rm start}$	$t_{\rm end}$	Ma	σ	$\chi^2/{\rm d.o.f}$
1	11	15	1.005589	0.008229	1.337163
2	11	15	0.996364	0.008559	1.347139
3	11	15	0.986890	0.009012	1.376443
4	11	15	0.978504	0.009616	1.405811
5	11	15	0.972625	0.010402	1.413036
6	11	15	0.971012	0.011214	1.426639
7	11	15	0.974346	0.012624	1.393397
8	11	15	0.983868	0.014333	1.351058

B

Obtaining the form of $\langle r^2 \rangle$

Consider $G_C(\vec{q})$, the Breit-frame fourier transform of the spatial charge density

$$G_C(\vec{q}) = \int \mathrm{dx}^3\, e^{i\vec{q}.\vec{x}} \rho(\vec{x})\,, \tag{B.1}$$

$$-\frac{\partial}{\partial q_i}\frac{\partial}{\partial q_i} G_C((\vec{q}) = \int \mathrm{dx}^3\, x_i x_i e^{i\vec{q}.\vec{x}} \rho(\vec{x})\,,$$

$$-\frac{\partial}{\partial q_i}\frac{\partial}{\partial q_i} G_C((\vec{q})\Big|_{\vec{q}=\vec{0}} = \int \mathrm{dx}^3\, x_i x_i e^{i\vec{q}.\vec{x}} \rho(\vec{x})\Big|_{\vec{q}=\vec{0}}. = \langle r^2 \rangle$$

We can rewrite the LHS via the chain rule as

$$-\frac{\partial}{\partial q_i}\frac{\partial Q^2}{\partial q_i}\frac{\partial}{\partial Q^2} G_C(Q^2)\Big|_{Q^2=0}\,, \tag{B.2}$$

where

$$Q^2 = -\vec{q}^2 = q_i q_i - q_0 q_0 = q_i q_i$$

in the Breit frame.

Recall that

$$\frac{\partial Q^2}{\partial q_i} = 2 q_i\,. \tag{B.3}$$

Thus we may write

$$\langle r^2 \rangle = -\frac{\partial}{\partial q_i} 2 q_i \frac{\partial}{\partial Q^2} G(Q^2)\Big|_{Q^2=0}. \tag{B.4}$$

$\frac{\partial}{\partial q_i} q_i = 3$ in 3-dimensions, so this is simply

$$\langle r^2 \rangle = -6 \frac{\partial}{\partial Q^2} G(Q^2)\big|_{Q^2=0} \quad \blacksquare \tag{B.5}$$

Source dependence results for the SU(3) $\beta = 4.60$, $20^3 \times 40$ lattice

n_G	$Q_{\text{paths}} = 1$	$Q_{\text{paths}} = 3$
4	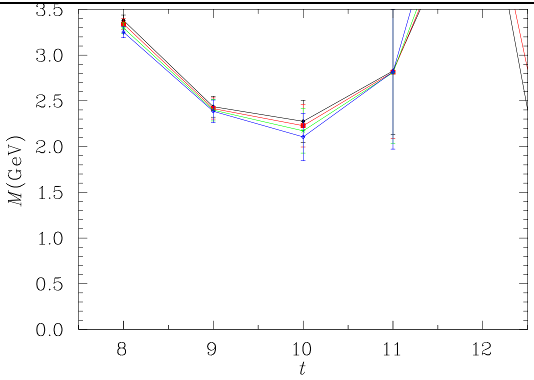	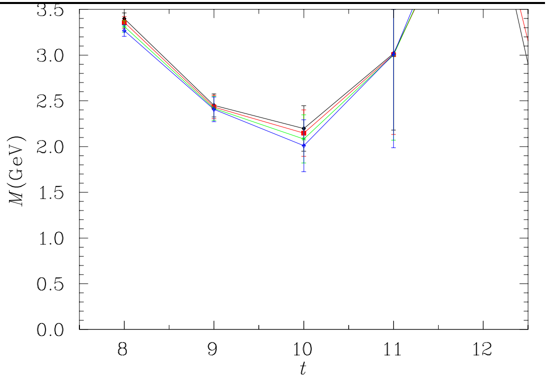
8	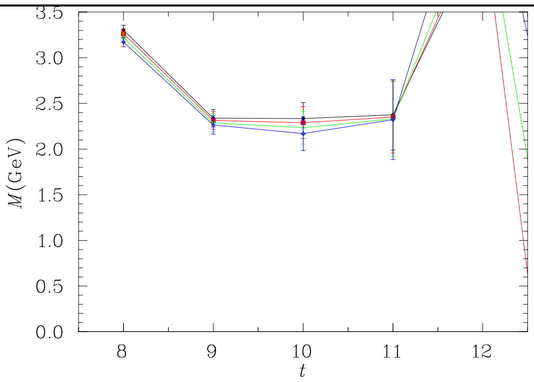	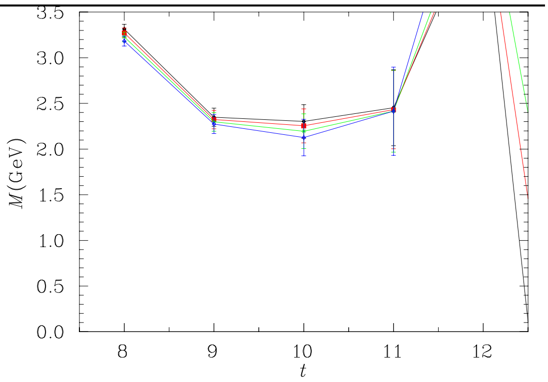
10	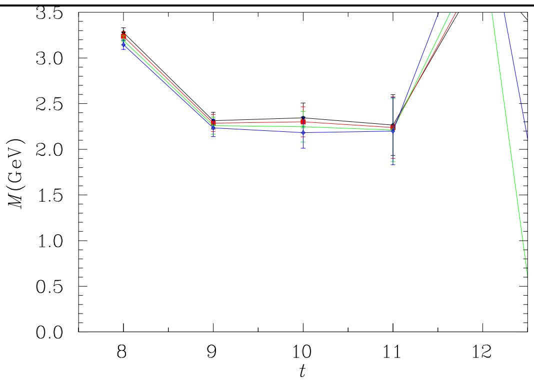	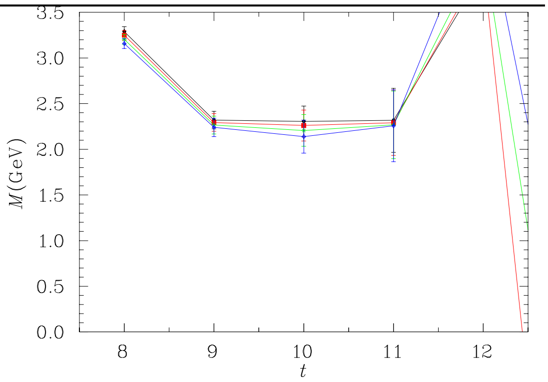

Table C.1: Exotic meson Effective masses from the $20^3 \times 40$ lattice for χ_2 with $n_{\text{src}} = 35$. Results for the heaviest four quark masses are depicted.

n_G	$Q_{\text{paths}} = 1$	$Q_{\text{paths}} = 3$
20	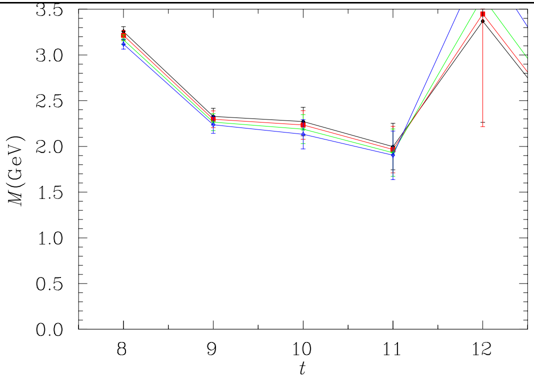	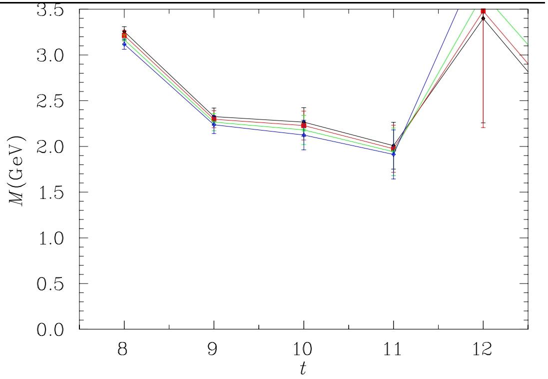
30	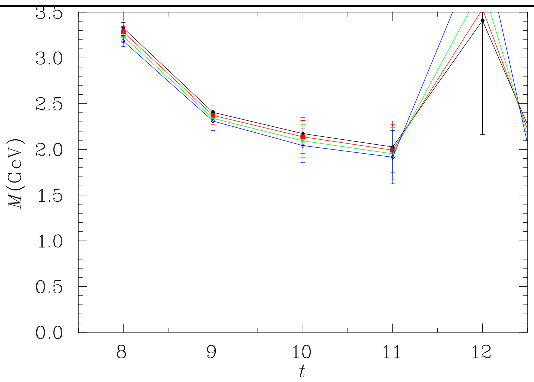	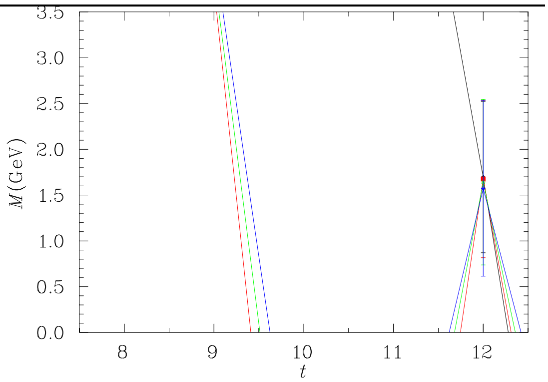

Table C.2: Exotic meson Effective masses from the $20^3 \times 40$ lattice for χ_2 with $n_{\text{src}} = 35$. Results for the heaviest four quark masses are depicted.

n_G	$Q_{\text{paths}} = 1$	$Q_{\text{paths}} = 3$
4	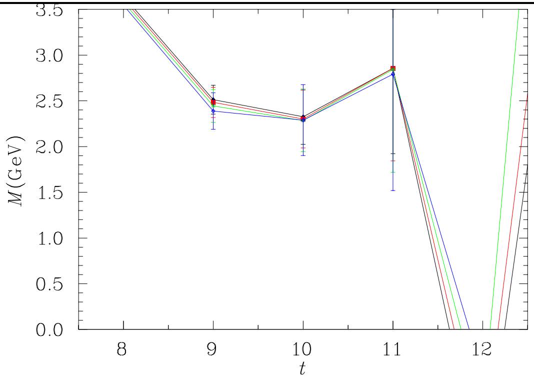	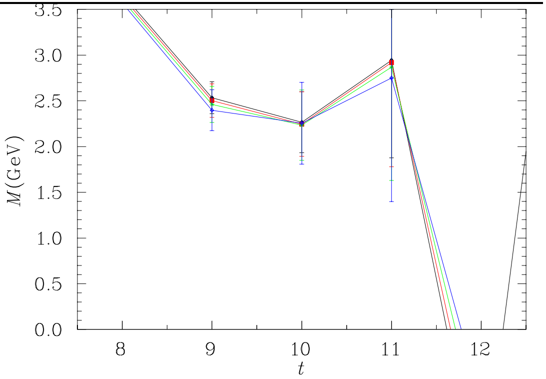
8	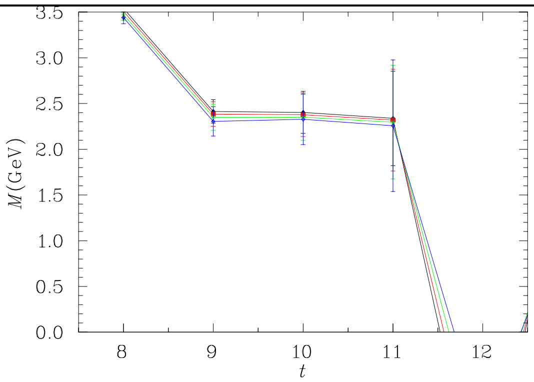	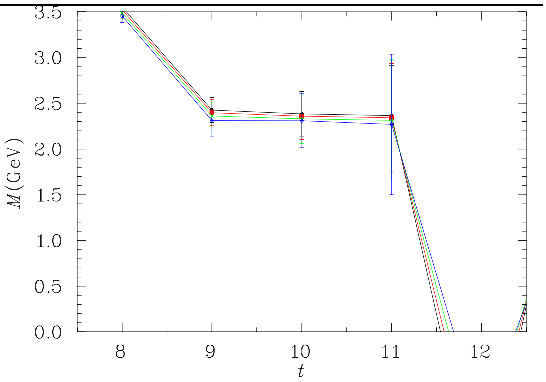
10	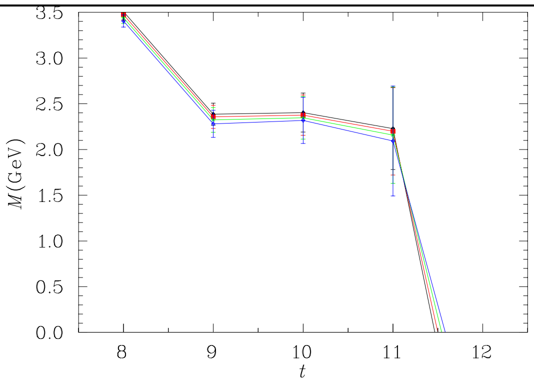	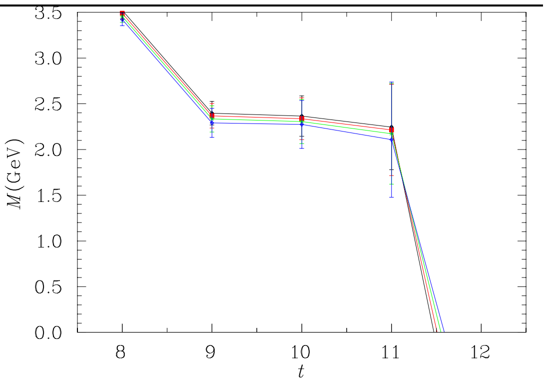

Table C.3: Exotic meson Effective masses from the $20^3 \times 40$ lattice for χ_3 with $n_{\text{src}} = 35$. Results for the heaviest four quark masses are depicted.

n_G	$Q_{\text{paths}} = 1$	$Q_{\text{paths}} = 3$
20	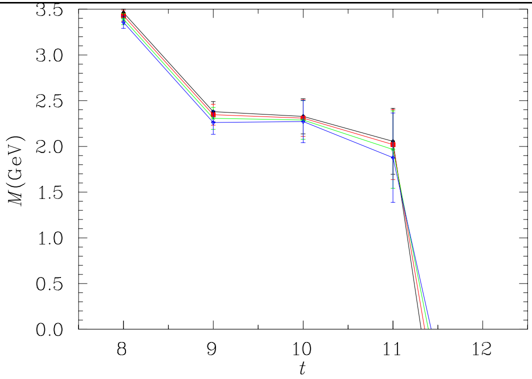	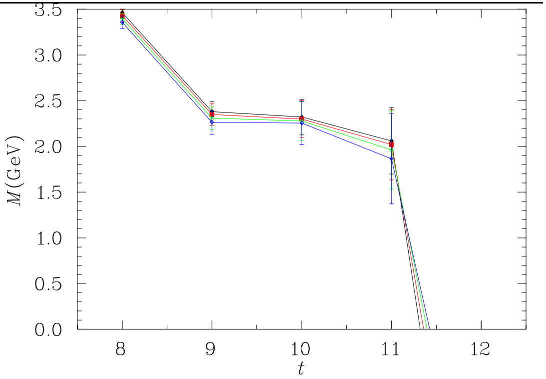
30	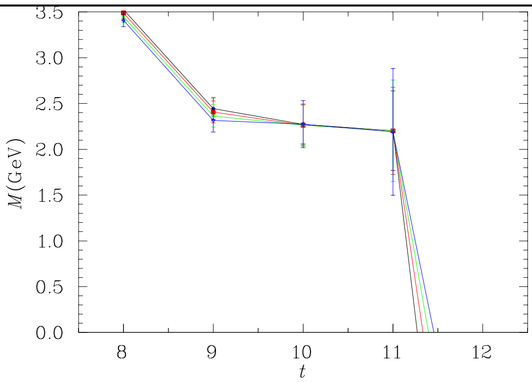	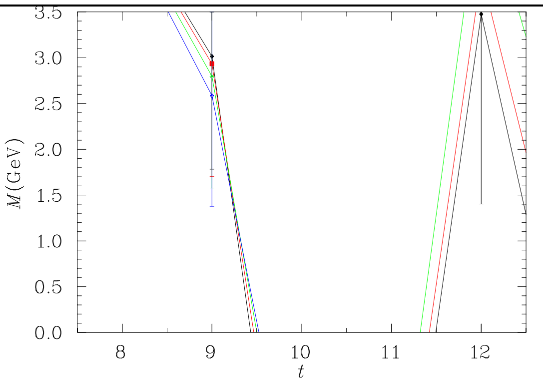

Table C.4: Exotic meson Effective masses from the $20^3 \times 40$ lattice for χ_3 with $n_{\text{src}} = 35$. Results for the heaviest four quark masses are depicted.

D

Quark-level calculations

D.1 Two-point function

Consider the following two-point function for some x with $x_0 > 0$.

$$\chi(x;[U])\tilde{\chi}^{\dagger}(0;[U]) \tag{D.1}$$

where $\chi = \bar{q}_2^a H^{ab} q_1^b$ and $\tilde{\chi}_{\nu}^{\dagger} = \bar{q}_1^{b'} \gamma_4 \tilde{H}^{\dagger^{b'a'}} \gamma_4 q_2^{a'}$. Here the H and $\tilde{H}$ are a product of gamma matrices and gauge functionals, the tilde indicates that these may be different at source and sink. We shall restrict ourselves here to the case $q_1 \neq q_2$, as this is the only case that can be handled efficiently using lattice techniques. To minimise the necessity of indices, let us choose $q_1, q_2 = u, d$.

Inserting these operators, we rewrite the two-point function as

$$\bar{d}^a(x) H^{ab} u^b(x) \bar{u}^{b'}(0) \gamma_4 \tilde{H}^{\dagger^{b'a'}} \gamma_4 d^{a'}(0) \tag{D.2}$$

With the spinor indices written out explicitly this is

$$\bar{d}_{\alpha}^{a}(x)\, H_{\alpha\beta}^{ab}\, u_{\beta}^{b}(x)\, \bar{u}_{\beta'}^{b'}(0)\, (\gamma_4 \tilde{H}^{\dagger^{b'a'}} \gamma_4)_{\beta'\alpha'}\, d_{\alpha'}^{a'}(0) \tag{D.3}$$

One proceeds by contracting out quark pairs to construct propagators:

$$\begin{aligned} q_{\alpha}^{a}(x)\bar{q}_{\beta}^{b}(0) &= S_{\alpha\beta}^{ab}(x,0) \\ \bar{q}_{\alpha}^{a}(x) q_{\beta}^{b}(0) &= -S_{\beta\alpha}^{ba}(0,x)\,. \end{aligned} \tag{D.4}$$

We denote $S(x,0)$ the fermion propagator from 0 to x.

Eq. (D.3) corresponds to

$$-(S_d)_{\alpha'\alpha}^{a'a}(0,x)\, H_{\alpha\beta}^{ab}\, (S_u)_{\beta\beta'}^{bb'}(x,0)\, (\gamma_4 \tilde{H}^{\dagger^{b'a'}} \gamma_4)_{\beta'\alpha'}\,. \tag{D.5}$$

For Wilson-like fermions, the following property holds:

$$(\gamma_5)_{\alpha\alpha'}\, S_{\alpha'\beta'}^{ab}(0,x;[U])\, (\gamma_5)_{\beta'\beta} = S_{\beta\alpha}^{ba\,\star}(x,0;[U]) \tag{D.6}$$

enabling us to write the above in terms of forward-going quark propagators as

$$-(\gamma_5)_{\alpha\gamma}(S_d)_{\gamma\delta}^{aa'\star}(x,0,[U])\, (\gamma_5)_{\delta\alpha'}\, H_{\alpha\beta}^{ab}\, (S_u)_{\beta\beta'}^{bb'}(x,0,[U])\, (\gamma_4 \tilde{H}^{\dagger^{b'a'}} \gamma_4)_{\beta'\alpha'}\,. \tag{D.7}$$

Finally, we make use of the symmetry of γ_5 under transposition to rewrite this as

$$\begin{aligned} &-(\gamma_5)_{\gamma\alpha}(S_d)_{\gamma\delta}^{aa'\star}(x,0,[U])\, (\gamma_5)_{\alpha'\delta}\, H_{\alpha\beta}^{ab}\, (S_u)_{\beta\beta'}^{bb'}(x,0,[U])\, (\gamma_4 \tilde{H}^{\dagger^{b'a'}} \gamma_4)_{\beta'\alpha'} && \text{(D.8)} \\ &= -\mathrm{tr}_{\mathrm{sp}}\{\gamma_5\, H^{ab}\, (S_u)^{bb'}(x,0,[U]) \gamma_4 \tilde{H}^{\dagger^{b'a'}} \gamma_4 \gamma_5 (S_d)^{aa'\dagger}(x,0,[U])\} && \text{(D.9)} \end{aligned}$$

In the case of the π-meson, where $H = \gamma_5$, this is simply $\mathrm{tr}_{\mathrm{sp}}\{(S_u)^{aa'}(S_d)^{aa'\dagger}\}$.

D.2 Electromagnetic current insertion

Consider the following three-point function:

$$G^{\mu}(x_2, x_1, 0) = \chi(x_2) j^{\mu}(x_1) \chi^{\dagger}(0) \tag{D.10}$$

Let us take the case where $\chi = \bar{q}_2^a \Gamma q_1^a$. Then $\chi^{\dagger} = \bar{q}_1^a \gamma_4 \Gamma^{\dagger} \gamma_4 q_2^a$. The electromagnetic current can be written as $j^{\mu} = \sum_f Q_f \bar{q}_f \gamma^{\alpha} q_f$, where Q_f is the electric charge of the particular flavour involved. As above, let us take q_1, q_2 as u, d to economise on indices.

Inner products, and thus bra-ket expressions are linear, so we can take this sum out to write $G^{\mu}(x_2, x_1, 0)$ as

$$\begin{aligned} & q_u \bar{d}_{\alpha}^a(x_2) \Gamma_{\alpha\beta} u_{\beta}^a(x_2)\, \bar{u}_{\gamma}^b(x_1) \gamma_{\gamma\delta}^{\mu} u_{\delta}^b(x_1)\, \bar{u}_{\rho}^c(0) \big(\gamma_4 \Gamma^{\dagger} \gamma_4\big)_{\rho\sigma} d_{\sigma}^c(0) \\ + \;\; & q_d \bar{d}_{\alpha}^a(x_2) \Gamma_{\alpha\beta} u_{\beta}^a(x_2)\, \bar{d}_{\gamma}^b(x_1) \gamma_{\gamma\delta}^{\mu} d_{\delta}^b(x_1)\, \bar{u}_{\rho}^c(0) \big(\gamma_4 \Gamma^{\dagger} \gamma_4\big)_{\rho\sigma} d_{\sigma}^c(0)\,. \end{aligned}$$

Contracting the fermion operators to form quark propagators yields

$$\begin{aligned} & q_u S^{\star ca}_{\;\;\sigma\alpha}(0, x_2) \Gamma_{\alpha\beta} (S_3)_{\beta\rho}^{ac}(x_2, x_1, 0; \mu) \big(\gamma_4 \Gamma^{\dagger} \gamma_4\big)_{\rho\sigma} \\ + \;\; & q_d \Gamma_{\alpha\beta} (\tilde{S}_3)_{\beta\rho}^{\star ac}(x_2, x_1, 0; \mu) u_{\beta}^a(x_2)\, \bar{u}_{\rho}^c(0) \big(\gamma_4 \Gamma^{\dagger} \gamma_4\big)_{\rho\sigma}\,, \end{aligned} \tag{D.11}$$

where we introduce the “ forwards 3-point propagator”:

$$\begin{aligned} (S_3)_{\alpha\beta}^{ab}(x_2, x_1, 0; \mu) \;&= q_{\alpha}^a(x_2)\, \bar{q}_{\sigma}^c(x_1) \gamma_{\sigma\rho}^{\mu} q_{\rho}^c(x_1)\, \bar{q}_{\beta}^b(0) \\ &= S_{\alpha\sigma}^{ac}(x_2, x_1) \gamma_{\sigma\rho}^{\mu} S_{\rho\beta}^{cb}(x_1, 0) - S_{\alpha\beta}^{ab}(x_2, 0) \gamma_{\sigma\rho}^{\mu} S^{\star cc}_{\;\;\rho\sigma}(x_1, x_1) \end{aligned} \tag{D.12}$$

and the “backwards 3-point propagator”:

$$\begin{aligned} (\tilde{S}_3)^{\star ab}_{\;\;\alpha\beta}(x_2, x_1, 0; \mu) \;&= \bar{q}_{\alpha}^a(x_2)\, \bar{q}_{\sigma}^c(x_1) \gamma_{\sigma\rho}^{\mu} q_{\rho}^c(x_1)\, q_{\beta}^b(0) \\ &= \;\; S^{\star ca}_{\;\;\rho\alpha}(x_1, x_2) \gamma_{\sigma\rho}^{\mu} S^{\star bc}_{\;\;\beta\sigma}(0, x_1) + S^{\star cc}_{\;\;\rho\sigma}(x_1, x_1) \gamma_{\sigma\rho}^{\mu} S^{\star ba}_{\;\;\beta\alpha}(0, x_2) \end{aligned} \tag{D.13}$$

The second terms in the forwards and backwards 3-point propagators represent disconnected loop contributions, and in the spirit of the quenched approximation we simply drop them. The final feature of our calculation is that we use an improved conserved vector current derived from the fermion action, rather than the local formulation above.

E

REDUCE script for calculating ratios of three to two-point functions

```
%  To run type:  in "Spin1FormFactors.red";
%  To quit:      bye;
%
ON DIV;
%
%  A few definitions
%
INDEX AL,B,RHO,LAM,SIG;
VECTOR PRho,PpRho,MU,NU,PFinal,PInitial,TAU;
VECTOR pplus,pzero,pminus;
NOSPUR L;                              % Use LTR for traces.
MASS PRho=mRho, PpRho=mRho;
MSHELL PRho,PpRho;
VECTOR Dir0,DirI,DirJ,DirK;
%
ORDER G1,G2,G3;
%
FOR ALL L,AL,B LET SIGMA(L,AL,B) = (I/2)*(G(L,AL,B)-G(L,B,AL));
%
FOR ALL AL,B,P,M LET SPINSUM(AL,B,P,M) =
                        - ( (AL.B) - (P.AL)*(P.B)/(M^2) );
%
%  Note q = p'-p matches PRD 46 2141 (1992)
%
FOR ALL RHO,MU,SIG,P,PP,M LET HINT(RHO,MU,SIG,P,PP,M) = -(
     G1 * (RHO.SIG) * (P.MU+PP.MU)
    +G2 * ( (PP.RHO-P.RHO) * (MU.SIG) - (PP.SIG-P.SIG) * (MU.RHO)  )
    -G3 * ( (PP.RHO-P.RHO) * (PP.SIG-P.SIG) * (P.MU+PP.MU) )/(2*M^2) );
%
% Define vector p_0
LET pzero.Dir0 = mRho;
LET pzero.DirI = px_i;
LET pzero.DirJ = py_i;
LET pzero.DirK = pz_i;
LET pzero.pzero = mRho*mRho;
LET abs(mRho) = mRho;
normRho := 1/(4*eRho*mRho);

% Define vector p_+
LET pplus.Dir0 = eRho;
LET pplus.DirI = px + px_i;
LET pplus.DirJ = py_i;
LET pplus.DirK = pz_i;
LET pplus.pplus = mRho * mRho;

% Define vector p_-
LET pminus.Dir0 = eRho;
LET pminus.DirI = px_i -px;
LET pminus.DirJ = py_i;
LET pminus.DirK = pz_i;
LET pminus.pminus = mRho * mRho;

LET pplus.pzero = mRho * eRho;
LET pminus.pzero = mRho * eRho;

LET PRho.PpRho  = mRho * eRho;
LET Dir0.Dir0 = 1;
LET Dir0.DirI = 0;
LET Dir0.DirJ = 0;
LET Dir0.DirK = 0;
LET DirI.DirJ = 0;
LET DirI.DirK = 0;
LET DirJ.DirK = 0;
LET DirI.DirI =-1;
LET DirJ.DirJ =-1;
LET DirK.DirK =-1;

LET px_i = 0;
LET py_i = 0;
LET pz_i = 0;

LET eRho       = SQRT(px^2 + mRho^2);
%
%
ResEle := SPINSUM(MU,RHO,PFinal,mRho) * HINT(RHO,TAU,SIG,PInitial,PFinal,mRho) *
                          SPINSUM(SIG,NU,PInitial,mRho)*normRho;
Forwards := SUB(PInitial=pzero,PFinal=pplus,ResEle);
```

```
Backwards := SUB(PInitial=pplus,PFinal=pzero,ResEle);
Denom := SPINSUM(MU,MU,pplus,mRho) * SPINSUM(NU,NU,pzero,mRho)*normRho;
%
% Separation of components.
%
ResEle001 := SUB(MU=Dir0,NU=DirI,TAU=Dir0,Forwards)* SUB(MU=DirI,NU=Dir0,TAU=Dir0,Backwards) / SUB(MU=Dir0,NU=DirI,Denom);
ResEle101 := SUB(MU=DirI,NU=DirI,TAU=Dir0,Forwards)* SUB(MU=DirI,NU=DirI,TAU=Dir0,Backwards) / SUB(MU=DirI,NU=DirI,Denom);
ResEle101Forwards := SUB(MU=DirI,NU=DirI,TAU=Dir0,Forwards);
ResEle202 := SUB(MU=DirJ,NU=DirJ,TAU=Dir0,Forwards)* SUB(MU=DirJ,NU=DirJ,TAU=Dir0,Backwards) / SUB(MU=DirJ,NU=DirJ,Denom);
ResEle203 := SUB(MU=DirJ,NU=DirK,TAU=Dir0,Forwards)* SUB(MU=DirK,NU=DirJ,TAU=Dir0,Backwards) / SUB(MU=DirJ,NU=DirK,Denom);
ResEle303 := SUB(MU=DirK,NU=DirK,TAU=Dir0,Forwards)* SUB(MU=DirK,NU=DirK,TAU=Dir0,Backwards) / SUB(MU=DirK,NU=DirK,Denom);
ResEle302 := SUB(MU=DirK,NU=DirJ,TAU=Dir0,Forwards)* SUB(MU=DirJ,NU=DirK,TAU=Dir0,Backwards) / SUB(MU=DirK,NU=DirJ,Denom);

ResEle133 := SUB(MU=DirI,NU=DirK,TAU=DirK,Forwards)* SUB(MU=DirK,NU=DirI,TAU=DirK,Backwards) / SUB(MU=DirI,NU=DirK,Denom);
ResEle132 := SUB(MU=DirI,NU=DirJ,TAU=DirK,Forwards)* SUB(MU=DirJ,NU=DirI,TAU=DirK,Backwards) / SUB(MU=DirI,NU=DirJ,Denom);
ResEle331 := SUB(MU=DirK,NU=DirI,TAU=DirK,Forwards)* SUB(MU=DirI,NU=DirK,TAU=DirK,Backwards) / SUB(MU=DirK,NU=DirI,Denom);

%
ON FACTOR;
%
OUT "Spin1Product.res";
ResEle001;
ResEle101;
ResEle101Forwards;
ResEle202;
ResEle203;
ResEle303;
ResEle302;
ResEle133;
ResEle132;
ResEle331;
ResEle101 + ResEle101 - ResEle202 - ResEle303;
SHUT "Spin1Product.res";
OUT T;
%
END;
%
%  BYE;
```

F

Data pertaining to the calculation of meson form-factors

Table F.1: Rho meson mass data

i_κ	t_{start}	t_{end}	Ma	σ	$\chi^2/\mathrm{d.o.f}$
1	17	30	0.7312	0.0030	1.230
2	17	30	0.7067	0.0036	1.209
3	17	30	0.6797	0.0046	1.131
4	13	21	0.6537	0.0049	0.936
5	13	21	0.6309	0.0056	0.737
6	13	21	0.6160	0.0064	0.610
7	11	20	0.6039	0.0071	0.122
8	11	20	0.5982	0.0080	0.634

Table F.2: Pion mass data

i_κ	$t_{\rm start}$	$t_{\rm end}$	Ma	σ	$\chi^2/{\rm d.o.f}$
1	16	24	0.5411	0.0010	1.272
2	16	24	0.5013	0.0011	1.124
3	16	24	0.4539	0.0011	0.906
4	16	24	0.4014	0.0012	0.749
5	16	24	0.3471	0.0015	0.802
6	16	24	0.3020	0.0019	0.938
7	16	24	0.2412	0.0042	0.659
8	16	24	0.1968	0.0052	1.044

Table F.3: Strange quark contribution to K-meson form-factor.

i_κ	$t_{\rm start}$	$t_{\rm end}$	G_C	σ	$\chi^2/{\rm d.o.f}$
1	20	30	0.8178	0.0041	0.405
2	20	30	0.8196	0.0045	0.363
3	20	30	0.8215	0.0051	0.329
4	18	30	0.8233	0.0055	0.621
5	18	30	0.8249	0.0061	0.510
6	18	30	0.8256	0.0068	0.576
7	18	24	0.8260	0.0077	0.971
8	16	24	0.8279	0.0078	0.742

Table F.4: Strange quark contribution to K^*-meson charge form-factor.

i_κ	$t_{\rm start}$	$t_{\rm end}$	G_C	σ	$\chi^2/{\rm d.o.f}$
1	20	30	0.7713	0.0070	0.845
2	20	29	0.7706	0.0077	0.853
3	20	28	0.7689	0.0087	0.918
4	20	28	0.7657	0.0103	1.014
5	20	27	0.7602	0.0124	0.972
6	18	27	0.7564	0.0134	1.183
7	18	25	0.7491	0.0148	0.751
8	17	25	0.7454	0.0154	0.626

Table F.5: Up quark contribution to K-meson form-factor.

i_κ	$t_{\rm start}$	$t_{\rm end}$	G_C	σ	$\chi^2/{\rm d.o.f}$
1	20	30	0.8346	0.0042	0.619
2	20	30	0.8302	0.0045	0.346
3	20	30	0.8215	0.0051	0.329
4	18	30	0.8126	0.0055	0.415
5	18	30	0.8041	0.0062	0.398
6	18	30	0.7976	0.0068	0.361
7	18	24	0.7920	0.0077	0.750
8	16	24	0.7910	0.0081	0.935

Table F.6: Up quark contribution to K^*-meson charge form-factor.

i_κ	$t_{\rm start}$	$t_{\rm end}$	G_C	σ	$\chi^2/{\rm d.o.f}$
1	20	30	0.7939	0.0067	0.897
2	20	29	0.7828	0.0075	0.886
3	20	28	0.7689	0.0087	0.918
4	20	28	0.7538	0.0106	1.016
5	20	27	0.7384	0.0133	1.021
6	18	27	0.7271	0.0147	1.206
7	18	24	0.7160	0.0172	0.806
8	17	24	0.7074	0.0192	0.695

Table F.7: Up quark contribution to π-meson charge form-factor.

i_κ	$t_{\rm start}$	$t_{\rm end}$	G_C	σ	$\chi^2/{\rm d.o.f}$
1	20	30	0.8327	0.0035	0.649
2	20	30	0.8284	0.0041	0.387
3	20	30	0.8215	0.0051	0.329
4	18	30	0.8149	0.0061	0.464
5	18	30	0.8100	0.0083	0.616
6	18	30	0.8091	0.0120	0.825
7	18	21	0.8123	0.0219	0.013
8	16	21	0.8332	0.0301	0.646

Table F.8: Up quark contribution to ρ-meson Charge form-factor.

i_κ	t_{start}	t_{end}	G_C	σ	$\chi^2/\text{d.o.f}$
1	20	30	0.7954	0.0054	1.021
2	20	29	0.7841	0.0066	0.940
3	20	28	0.7689	0.0087	0.918
4	20	25	0.7501	0.0122	1.102
5	20	24	0.7267	0.0179	1.116
6	18	23	0.7079	0.0218	1.491
7	18	21	0.6830	0.0316	0.406
8	17	20	0.6602	0.0398	0.914

Table F.9: Strange quark contribution to K^* magnetic form-factor.

i_κ	t_{start}	t_{end}	G_M	σ	$\chi^2/\text{d.o.f}$
1	18	24	1.4064	0.0213	0.864
2	18	24	1.4125	0.0228	0.777
3	18	24	1.4182	0.0252	0.664
4	16	20	1.4276	0.0265	0.580
5	16	20	1.4352	0.0282	0.517
6	16	20	1.4378	0.0299	1.161
7	15	20	1.4403	0.0314	1.216
8	15	20	1.4409	0.0332	0.196

Table F.10: Up quark contribution to K^* magnetic form-factor.

i_κ	t_{start}	t_{end}	G_M	σ	$\chi^2/\text{d.o.f}$
1	18	24	1.3733	0.0187	0.776
2	18	24	1.3953	0.0213	0.712
3	18	24	1.4182	0.0252	0.664
4	16	20	1.4453	0.0277	0.639
5	16	20	1.4687	0.0314	0.636
6	16	20	1.4850	0.0356	0.920
7	15	19	1.5006	0.0405	0.454
8	15	19	1.5127	0.0460	0.359

Table F.11: Up quark contribution to ρ magnetic form-factor.

i_κ	t_{start}	t_{end}	G_M	σ	χ^2/d.o.f
1	18	24	1.3599	0.0160	1.113
2	18	24	1.3889	0.0194	0.845
3	18	24	1.4182	0.0252	0.664
4	16	20	1.4547	0.0293	0.716
5	16	20	1.4838	0.0365	0.874
6	16	20	1.4961	0.0467	1.114
7	15	19	1.5002	0.0601	1.007
8	15	17	1.4828	0.0812	0.329

Table F.12: Strange quark contribution to K^* quadrupole form-factor.

i_κ	t_{start}	t_{end}	G_Q	σ	χ^2/d.o.f
1	16	20	-0.2936	0.0280	0.268
2	16	20	-0.2937	0.0299	0.293
3	16	20	-0.2932	0.0327	0.339
4	16	21	-0.2921	0.0371	0.478
5	15	20	-0.2912	0.0411	0.524
6	15	19	-0.2875	0.0456	0.138
7	15	19	-0.2815	0.0527	0.323
8	15	19	-0.2798	0.0603	0.439

Table F.13: Up quark contribution to K^* quadrupole form-factor.

i_κ	t_{start}	t_{end}	G_Q	σ	χ^2/d.o.f
1	16	20	-0.2857	0.0264	0.455
2	16	20	-0.2886	0.0288	0.376
3	16	20	-0.2932	0.0327	0.339
4	16	21	-0.3014	0.0389	1.227
5	15	20	-0.3073	0.0447	1.174
6	15	22	-0.3170	0.0520	1.255
7	15	19	-0.3339	0.0646	1.032
8	15	19	-0.3417	0.0791	1.024

Table F.14: Up quark contribution to ρ quadrupole form-factor.

i_κ	$t_{\rm start}$	$t_{\rm end}$	G_Q	σ	$\chi^2/{\rm d.o.f}$
1	16	20	-0.2852	0.0224	0.537
2	16	20	-0.2887	0.0263	0.367
3	16	20	-0.2932	0.0327	0.339
4	16	21	-0.2992	0.0438	0.788
5	15	20	-0.3026	0.0560	0.623
6	15	19	-0.2962	0.0744	0.451
7	15	19	-0.3091	0.1116	0.525
8	15	18	-0.3039	0.1652	0.626

Table F.15: Q^2 values for pion (lattice units)

i_κ	Q^2	σ
1	0.091542	0.000023
2	0.090542	0.000029
3	0.089069	0.000038
4	0.086962	0.000054
5	0.084038	0.000094
6	0.080797	0.000159
7	0.074714	0.000505
8	0.068450	0.000838

Table F.16: Q^2 values for K (lattice units)

i_κ	Q^2	σ
1	0.090486	0.000030
2	0.089868	0.000033
3	0.089069	0.000038
4	0.088124	0.000045
5	0.087097	0.000055
6	0.086234	0.000065
7	0.085220	0.000108
8	0.084666	0.000092

Table F.17: Q^2 values for ρ (lattice units)

i_κ	Q^2	σ
1	0.094518	0.000032
2	0.094250	0.000041
3	0.093923	0.000058
4	0.093574	0.000070
5	0.093236	0.000086
6	0.092998	0.000106
7	0.092793	0.000123
8	0.092694	0.000143

Table F.18: Q^2 values for K^* (lattice units)

i_κ	Q^2	σ
1	0.094238	0.000042
2	0.094091	0.000049
3	0.093923	0.000058
4	0.093753	0.000064
5	0.093600	0.000070
6	0.093497	0.000075
7	0.093409	0.000080
8	0.093364	0.000084

Papers by the author

1. **“Light-quark FLIC fermion simulations of the 1-+ exotic meson”**
   J. N. Hedditch, B. G. Lasscock, D. B. Leinweber, A. G. Williams, W. Kamleh and J. M. Zanotti
   PoS **LAT2005**, 040 (2006) [arXiv:hep-lat/0510103]
   Talk given at 23rd International Symposium on Lattice Field Field: Lattice 2005, Trinity College, Dublin, Ireland, 25-30 Jul 2005

2. **“1-+ exotic meson at light quark masses”**
   J. N. Hedditch, W. Kamleh, B. G. Lasscock, D. B. Leinweber, A. G. Williams and J. M. Zanotti
   Phys. Rev. D **72**, 114507 (2005) [arXiv:hep-lat/0509106]

3. **“Search for the pentaquark resonance signature in lattice QCD”**
   B. G. Lasscock *et al.*
   Phys. Rev. D **72**, 014502 (2005) [arXiv:hep-lat/0503008]

4. **“FLIC mesons: Hybrids and exotics”**
   J. N. Hedditch, B. G. Lasscock, D. B. Leinweber, A. G. Williams and J. M. Zanotti
   Nucl. Phys. Proc. Suppl. **141**, 43 (2005)
   Prepared for Workshop on QCD Down Under, Barossa Valley and Adelaide, Australia, 10-19 Mar 2004

5. **“Spin-3/2 pentaquark resonance signature”**
   B. G. Lasscock *et al.*
   PoS **LAT2005**, 067 (2006)
   Prepared for 23rd International Symposium on Lattice Field Field: Lattice 2005, Trinity College, Dublin, Ireland, 25-30 Jul 2005

6. **“Lattice QCD Studies Of Pentaquarks And Exotics”**
   B. G. Lasscock *et al.*
   Nucl. Phys. Proc. Suppl. **153**, 348 (2006)
   Talk given at Workshop on Computational Hadron Physics (Hadron Physics 13), Nicosia, Cyprus, 14-17 Sep 2005

7. **“Hybrid mesons on the lattice with FLIC fermions”**
   J. N. Hedditch, B. G. Lasscock, D. B. Leinweber, A. G. Williams and J. M. Zanotti
   DESY-03-208
   Prepared for Workshop on Gluonic Excitations, Newport News, Virginia, 14-16 May 2003

8. **“Hybrid meson spectrum from the FLIC action”**
   J. N. Hedditch, D. B. Leinweber, A. G. Williams and J. M. Zanotti

Nucl. Phys. Proc. Suppl. **128**, 221 (2004) [arXiv:hep-lat/0402016]
Talk given at 2nd Cairns Topical Workshop on Lattice Hadron Physics 2003 (LHP 2003), Cairns, Australia, 22-30 Jul 2003

9. **“Hybrid and exotic mesons from FLIC fermions”**
   J. N. Hedditch, D. B. Leinweber, A. G. Williams and J. M. Zanotti
   Nucl. Phys. Proc. Suppl. **129**, 248 (2004) [arXiv:hep-lat/0309119]
   Presented at 21st International Symposium on Lattice Field Theory (LATTICE 2003), Tsukuba, Ibaraki, Japan, 15-19 Jul 2003

10. **“Nucleon resonances from FLIC fermions”**
    D. B. Leinweber, J. N. Hedditch, W. Melnitchouk, A. G. Williams and J. M. Zanotti
    Prog. Theor. Phys. Suppl. **151**, 138 (2003)
    Prepared for Tokyo - Adelaide Joint Workshop on Quarks, Astrophysics and Space Physics, Tokyo, Japan, 6-10 Jan 2003

11. **“Excited baryons from the FLIC fermion action”**
    W. Melnitchouk, J. N. Hedditch, D. B. Leinweber, A. G. Williams, J. M. Zanotti and J. B. Zhang
    Nucl. Phys. Proc. Suppl. **119**, 293 (2003) [arXiv:hep-lat/0210042]
    Submitted to 20th International Symposium on Lattice Field Theory (LATTICE 2002), Boston, Massachusetts, 24-29 Jun 2002

12. **“FLIC fermions and hadron phenomenology”**
    D. B. Leinweber *et al.*
    arXiv:nucl-th/0211014
    Invited plenary session talk at Conference on Quarks and Nuclear Physics (QNP 2002), Julich, Germany, 9-14 Jun 2002

13. **“Excited baryons in lattice QCD”**
    W. Melnitchouk *et al.*
    Phys. Rev. D **67**, 114506 (2003) [arXiv:hep-lat/0202022]

14. **“Low-lying eigenmodes of the Wilson-Dirac operator and correlations with topological objects”**
    D. J. Kusterer, J. Hedditch, W. Kamleh, D. B. Leinweber and A. G. Williams
    Nucl. Phys. B **628**, 253 (2002) [arXiv:hep-lat/0111029]